Magnetization Reversal Processes of Nanostructure Arrays

von der Fakultät für Naturwissenschaften der Technischen Universität Chemnitz
genehmigte Dissertation zur Erlangung des akademischen Grades

doctor rerum naturalium

(Dr. rer. nat.)

vorgelegt von: Dipl. Phys. Philipp Krone
geboren am 13.03.1987 in Ratingen
eingereicht am 29.03.2011

Gutachter:
Prof. Dr. Manfred Albrecht
Prof. Dr. Thomas Schrefl

Tag der Verteidigung: 29.07.2011

Bibliographic Description

Topic:
Magnetization Reversal Processes of Nanostructure Arrays

Dissertation
Technische Universität Chemnitz
von Diplom-Physiker Philipp Krone

Abstract:

In the thesis at hand, different concepts of magnetic recording were investigated both from an experimental and theoretical point of view. On the one hand, micromagnetic simulations of bit patterned media were performed examining the influence of magnetic and geometrical parameters on the magnetization reversal mechanism of the bit array. In this regard, the recording concept called "exchange coupled composite" (ECC) media was applied in combination with bit patterned media (BPM). It was demonstrated that
ECC/BPM is superior in terms of narrowing the SFD which is vital for the implementation of BPM as a recording scheme in magnetic data storage deviced. Moreover, the stability of the magnetic state was calculated for single nanomagnets using the nudged elastic band algorithm. It was found out that the magnetic and geometrical properties have a severe influence on both, the energy barrier for magnetization reversal and the magnetization reversal process of the single nanomagnets. On the other hand, experimental studies of granular CoCrPt:SiO_2 films deposited on self-assembled arrays of SiO_2 nanoparticles with a size from 10 nm to 330 nm have been carried out, showing a distinct size-dependence of the coercive field and remanent magnetization with changing nanoparticle size. Moreover, these films have been irradiated with Co^+ ions with different fluences, resulting in a change of the magnetic properties of the films due to both a change of the intergranular exchange coupling of the film and a degredation of the magnetic layers at higher irradiation fluences.

Keywords: magnetic recording, magnetization reversal, nanomagnetics, bit patterned media, micromagnetic simulations, granular CoCrPt:oxide

Contents

Chapter 1

Introduction

In1953, IBM noticed the necessity of something IBM called "Random Access File" with high capacity and rapid random access at a relatively low cost. After researching several other technologies including wire matrices, rod arrays, drums, drum arrays, etc. [1], the IBM San Jose finally invented the disk drive [2]. This disk drive created a new era in computer storage history, as it was less expensive and slower than typical main memory, but faster and more expensive than tape drives.

The commercial usage of hard disk drives began in the year 1956 with the first shipment of an IBM 305 RAMAC system including IBM Model 350 disk storage [3] (see figure 1.1).

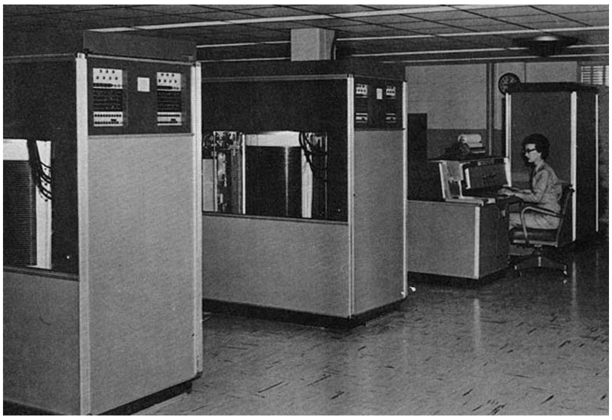

Figure 1.1: IBM 305 at U.S. Army Red River Arsenal Foreground: Two 350 disk drives. Background: 380 console and 305 processing unit.

Compared to modern hard disk drives, early disk drives were large and sensitive and thus suited to use in the protected environment of a data center rather than in an industrial environment, office or home. Disk media was nominally 8-inch or 14-inch platters, which required large equipment racks.

Hard disk drives were not commonly used with microcomputers until after 1980, when Shugart Technology introduced the ST-506, the first 5.25-inch hard drives, with a formatted capacity of 5 megabytes. The capacity of hard drives has grown exponentially over time. With early personal computers, a drive with a 20 megabyte capacity was considered huge. During the mid-1990s the typical hard disk drive for a PC had a capacity of about 1 GB. As of July 2010, desktop hard disk drives typically have a capacity of 500 to 1000 gigabytes, while the largest-capacity drives were 3 terabytes. Figure 1.2 shows a possible roadmap of the areal density from the year 2000 to 2016, compiled from different roadmaps [4, 5]. As illustrated in figure 1.2, approximately in the year 2011/12, a transition from standard perpendicular recording to shingled writing is about to take place as the common recording concepts are at its limit and thus new concepts need to be developed. Thereby, in shingled magnetic recording, adjacent tracks will be partially overwritten by writing information on the disc to achieve a closed pitch. However, the information needs to be written in a specific order on the hard disc drive to not loose information from other tracks [6].

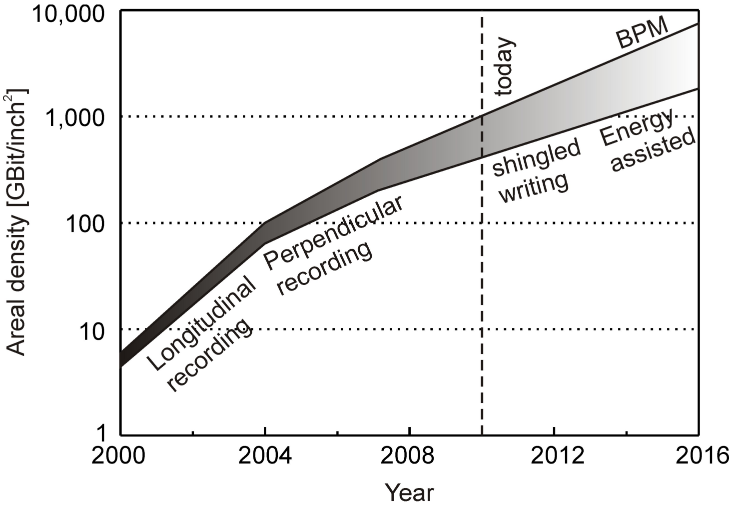

Figure 1.2: Possible development of the areal density from 2000 up to 2016.

In the second chapter of this thesis, state-of-the-art recording concepts and the possible recording concepts of the future shall be introduced and possible disadvantages and advantages will be outlined. After that, the theoretical background of this thesis, namely general magnetism and the theory of micromagnetism, will be discussed (chapter 3). Chapter 4 is about the basics of the experimental techniques used to deposit, tailor, and analyze the thin films. In chapter 5, results obtained in the frame of this work will be presented and its importance will be reviewed. Finally, the thesis will close with a summary of the work (chapter 6) and an outlook (chapter 7).

Chapter 2

Magnetic data storage

Information are processed as a binary value, being either “0” or “1”. To efficiently save those information, different concepts were developed over the last decades. In general, they can be divided into volatile and non-volatile memory:

- **volatile memory**: Volatile memory is computer memory that requires power to maintain the stored information. The most popular volatile memory is random access memory (RAM), used as short-time storage in computers.
- **non-volatile memory**: Non-volatile memory is memory that saves the information even when not powered. The most popular non-volatile memories are flash memory (USB sticks) and magnetic computer memory (hard disk drives - HDDs).

Due to several limitations of flash memory, as for example the limited number of read/write cycles, the magnetic computer memory is the most used memory type for long-term data storage.

In magnetic data storage, information are saved as the direction of magnetization in ferromagnets. There are several possibilities on how to realise the saving of the information with ferromagnets in practice. In the following chapter, an introduction to current recording concepts and recording media and to new concepts shall be given. Please note that no introduction to magnetic read/write heads and complete magnetic layer stacks inclusive soft underlayer will be given. For more information, see the following review articles: [7–10].

2.1 Current Recording Media - Perpendicular Granular Media

In currently produced HDDs, *perpendicular granular media*, consisting of CrCtPt:SiO_2, is used to save information. Figure 2.1 shows an example of such a granular media [11].

One bit of information is saved using about 60-80 grains with a magnetic moment pointing in the same direction, either up or down. This number of grains is needed to provide a sufficient large signal-to-noise ratio. As already partly discussed in section 3.5, the long-term stability for a storage time > 10 years is:

$$K_{\mathrm{U}}V \geq 60k_{\mathrm{B}}T \tag{2.1}$$

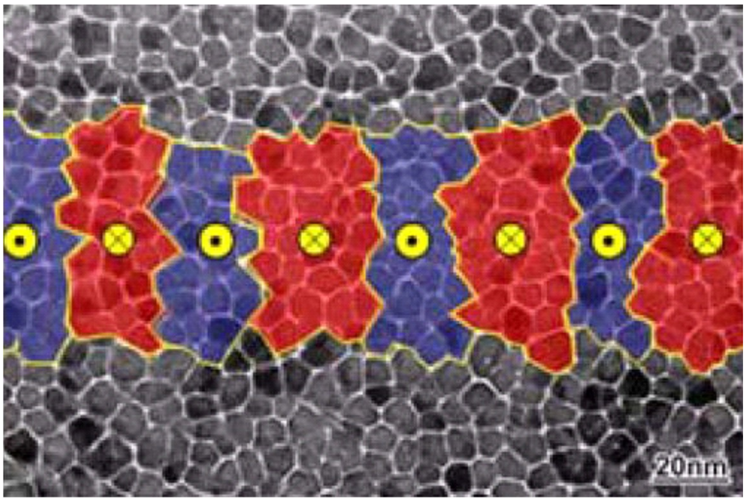

Figure 2.1: Conventional perpendicular granular recording media. The different bits are shown as red and blue areas [11].

with K_U being the magnetic anisotropy constant, V the volume of one grain, and T the temperature; k_B is the BOLTZMANN-constant. In case of a small thermal stability, the individual magnetic moments will be flipped due to the so-called superparamagnetism. In small enough particles, magnetization can randomly flip direction under the influence of temperature. The typical time between two flips is called the Néel relaxation time τ_N:

$$\tau_\mathrm{N} = \tau_0 \exp\left(\frac{K_\mathrm{U} V}{k_\mathrm{b} T}\right) \tag{2.2}$$

Due to an always increasing need of disk space, an increase of the areal density (number of bits per unit area) is necessary. Possible approaches are:

- Decrease of the number of grains per bit. This leads to a reduction of the signal-to-noise ratio (SNR), as the domain walls follow the grain boundaries. Moreover, it results in an increase of the switching field distribution due to intrinsic distributions of the smaller grains, e.g. size, magnetic anisotropy.
- Decrease of the volume of the grain. This leads to a reduction of the long-term stability and finally to an erasure of the saved information. To compensate for the decrease in grain volume, one has to increase the magnetic anisotropy value. However, due to a limitation of the magnetic write head, that writes the information on the recording media, the maximum achievable write field is about 1 T [12], which preserving a reasonable field gradient. As the coercive field of a grain, which needs to be overcome with the write field, is approximately linearly dependent on the magnetic anisotropy constant, a further increasement of K_U is not possible.

These number of issues is called the *trilemma in data storage*. Due to all these limitations, it is expected the the maximal areal density that can be achieved with PGM is about $1-2\,\text{Tbit/inch}^2$ [10, 13]. Therefore, new recording concepts are needed to extend the possible areal density.

2.2 New Recording Concepts

In the last few years, new magnetic recording concepts were developed to overcome the areal density limitation of current perpendicular granular media, including percolated media [14, 15], bit patterned media (BPM) [8, 16], exchange coupled composite (ECC) [17–19] media and energy-assisted magnetic recording (e.g. heat-assisted magnetic recording or microwave-assisted magnetic recording) [12].

2.2.1 Percolated Media

A novel concept of media proposed by ZHU and TANG [14] and SUESS [20] to overcome the issue of thermal stability is so-called *percolated media*. As described above, in conventional granular recording media, the grain size determines the width of the bit boundaries and therefore, the grain size needs to be reduced to increase the areal density. In order to tackle the problem of thermal stability, K_U of the media material is increased, which leads to issues of writability. On the other hand, if the reversal mechanism is based on domain pinning, the density and the size of the pinning sites would determine the size of the bit. If the pinning sites have a high density and a size smaller than the domain size, narrow transitions and high recording density could be achieved. In this case, the energy barrier for thermally excited reversal does not depend on the grain volume, but depends on the pinning energy associated with the pinning sites. Please note that this is only valid if the pinning energy is larger than the product of K_U and V, as otherwise, the entire pinned domain could reverse its magnetisation.

Although a detailed theoretical description of percolated media is provided in literature[11, 14, 21], there are only a few experimental realizations of a percolated perpendicular medium (see figure 2.2). In one example, evenly distributed nonmagnetic defects in a magnetic matrix were achieved by co-deposition of magnetic material (CoPt and FePt alloys) with nonmagnetic oxides (MgO, SiO) [15]. Another example concerns the deposition of Co/Pt multilayers onto anodized alumina substrates resulting in the formation of PPM with evenly distributed pinning centers [22]. In this case, the holes serve as pinning sites for the domain wall propagation due to the variation of the magnetic properties and magnetic film thickness around the perimeters of the holes. Furthermore, CoPt alloy films with perpendicular magnetic anisotropy were grown on SiO_2 nanoparticle arrays with particle sizes as small as 10 nm. [23, 24] The peculiar magnetization reversal behavior was attributed to the specific structure of the cap array where the pinning of domain walls was suggested to occur at the intersections between particles acting as defects. Recently, other approaches were presented, based on the pinning of magnetic domain walls in Co/Pt multilayer films on nonmagnetic defects given by either plasma etched

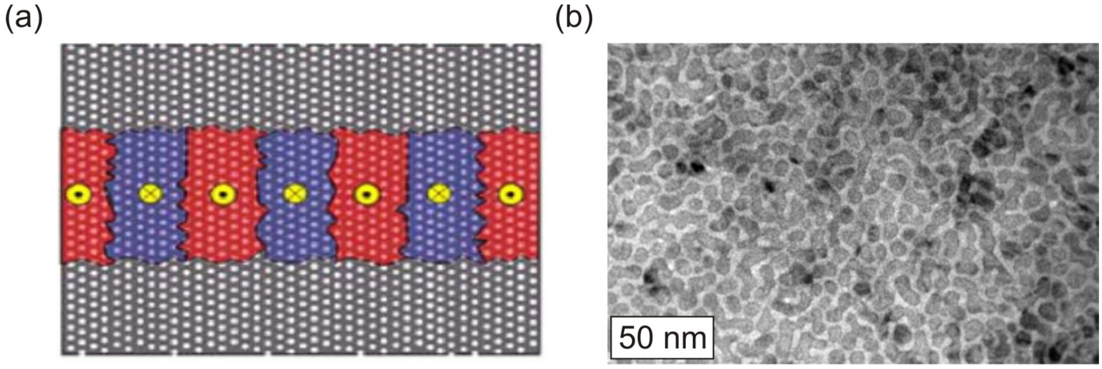

Figure 2.2: (a) Micromagnetic simulations [14], and (b) first experimental realisations of percolated perpendicular media [15].

polystyrene particles [25] or substrates with densely distributed perforations [26].

Punz et al.[27] found out that the pinning energy depends on the ratio between pinning site diameter and domain wall width. However, whether there is an optimal ratio which leads to a maximal pinning energy depends on the magnetic and geometrical parameters. For example for a fixed hard magnetic material, the pinning energy increases monotonically with increasing pinning site diameter and no optimal ratio can be found. For high areal densities, very dense and small pinning sites have to be used; thus, to have large pinning sites compared to the domain wall width, the magnetic material has to have a high magnetic anisotropy with a very thin domain wall. To achieve for example an areal density of 1 TBit/inch^2, the size of the pinning sites needs to be about 5 nm, leading to a necessary magnetic anisotropy constant of about 4.0×10^7 ergs/cm^3 for an exchange-coupled film with an exchange constant of 1×10^{-6} ergs/cm.

2.2.2 Bit patterned Media

Another novel approach introduced in 1996 towards areal densities above 1 Tbit/inch^2 is the so-called *bit patterned media* (BPM) concept [8, 9, 28]. A patterned recording medium consists of a regular array of magnetic elements (bits), each of which has uni-axial perpendicular magnetic anisotropy. Theoretical predictions show a possible areal density of up to 50 Tbit/inch^2 [29]. Figure 2.3 shows an example of such a bit patterned media with a period of about 500 nm.

Each element stores one bit of information, depending on its state of magnetization. Contrary to current granular media, the grains within each patterned bit are completly exchange-coupled. The major **advantages** of such a bit patterned medium are [8]:

- The transition noise is eliminated as the bit boundaries are defined by the physical boundaries of the bit.
- The thermal stability is substantially increased as the volume is not defined by one single grain but by the entire bit.

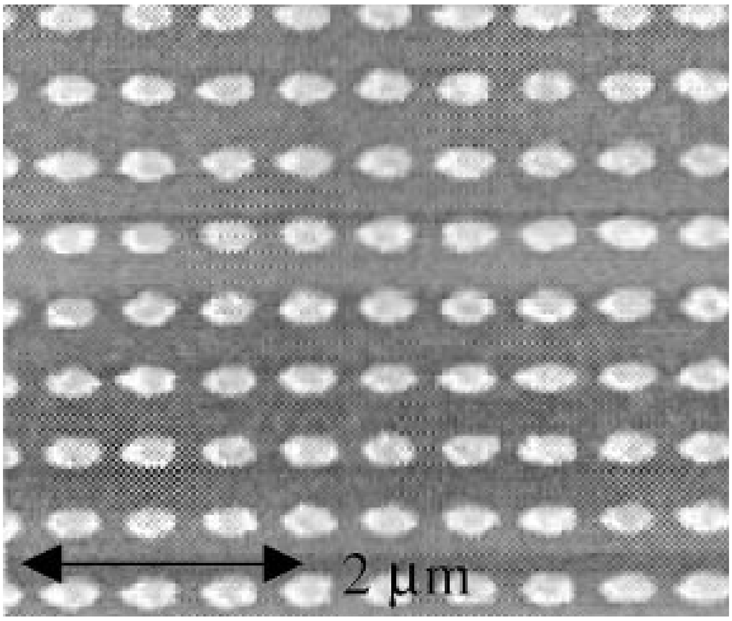

Figure 2.3: Scanning electron microscopy image of bit patterned media with a perdio of about 500 nm [8]
.

However, there are also **disadvantages** of the BPM recording concept:

- The fabrication of large-area arrays of elements with dimensions in the region of about 10 nm and a period of under 25 nm to achieve an areal density above 1 Tbit/inch^2 requires advanced lithography or self-assembly techniques.
- The control of the distribution of the magnetic properties, as for example given by the size and position of the magnetic units, as well as the variation of the intrinsic magnetic properties, as for example the magnetic anisotropy value is important. Thus, for instance, THOMSON et al. [30] demonstrated that the distribution of the magnetic anisotropy within an individual nanostructure is vital to understand the magnetization reversal process in nanopatterned magnetic arrays.
- The addressing of the array in the HDD requires high precision and high accuracy in the detection of magnetic fields on a very small scale. Especially in the writing process of individual bits, the applied magnetic field must be synchronized with the physical location of the specific element [31, 32].
- Possibilities to influence the switching field distribution of bit patterned media is not well understood up to now. In the frame of the thesis at hand, this issue shall be adressed intensively.

As already mentioned, advanced techniques have to be used to fabricate such BPM. In the following, a short summary of the most promising fabrication methods shall be given.

During **lithography**, the desired pattern is generated by exposure of a resist layer and then transferred into the magnetic material by a sequence of development, etching and deposition steps. The generation of the pattern itself can be accomplished by e.g. electron-beam lithography [33–35], X-ray of optical lithography [36], or imprint lithography [37]. Afterwards, the patterns can be transferred into the magnetic material by additive or subtractive processes:

- In an additive process, magnetic material is deposited after patterning.

- In a substractive process, the magnetic material is deposited first and then etched to form the desired pattern using a lithographically generated mask.

The most common lithography technique is the electron-beam lithography, where an electron-beam is used to write a pattern into a resist layer, which is subsequently developed to leave a template. However, this technique cannot be used for mass production as it is a serial method needing a long time to pattern for example a whole disc. In X-ray lithography, a thin membrane mask is place close to a resist-coated substrate and illuminated with soft X-rays of $1 - 10\,\mathrm{nm}$ wavelengths, leading to feature sizes below 20 nm. However, either long exposure times with laboratory X-ray or high intensity synchrotron radiation are necessary. Finally, in nanoimprimt lithography, a rigid mold is used to stamp patterns into a soft polymeric layer, analogous to the stamping of a compact disk. Featues as small as 10 nm dots on a 40 nm period have been made using evaporation and liftoff [37].

Another technique for creating BPM is the self-assembly of nanoparticles. Thereby, either magnetic nanoparticles, or non-magnetic nanoparticles with magnetic film deposited on it are used as pattern. Such nanoparticles can have a sub-10 nm size and a corresponding period of about 10 nm, leading to an areal density of about 5 Tbit/inch^2 [38]. However, the largest issue is to obtain a uniform particle distribution over a large area, as for example a whole disk. Only a small size distribution of the particles leads to defects in the array which makes the entire array hardly usable for data storage.

However, recently a combination of lithography and self-assembly of nonmagnetic particles, so-called *guided self-assembly*, was applied to achieve BPM with an areal density of up to 1 Tbit/inch^2 [39]. They combined electron-beam lithography and self-assembly of block copolymers to achieve long-range order of the bits and thus narrow the switching field distribution of the BPM. Figure 2.4 shows a comparison between (a) guided block copolymers assembly, (b,c) unguided block copolymer assembly, and (d) and electron-beam lithography [39].

Whereas in the discussed case of an areal density of 0.5 Tbit/inch^2, the switching field distribution is about 10% for the pattern created via electron-beam lithography only and between 10% and 20% for the unguided self-assembly, the SFD is only about 3% for the pattern created using guided block copolymer assembly. Thus, this route is one of the most promising technique for the creation of bit patterned media [39].

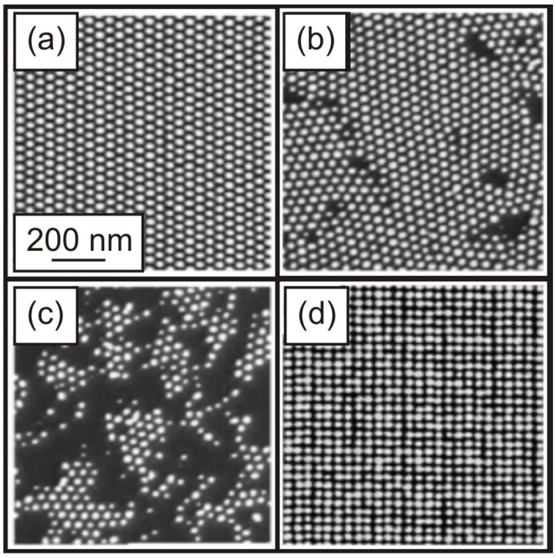

Figure 2.4: Comparison between (a) guided block copolymers assembly, (b, c) unguided block copolymer assembly, and (d) and electron-beam lithography at an areal density of 0.5 Tbit/inch^2 [39].

2.2.3 Exchange coupled composite (ECC) media

Exchange coupled composite (ECC) media consists of magnetic grains with a hard/soft bilayer structure. The high magnetic anisotropy layer provides thermal stability. The low magnetic anisotropy layer acts as a lever to help switch the hard layer during writing. Recent theoretical reviews on ECC media for magnetic data storage are presented by Victora and Shen [40] and Suess et al. [18].

In exchange spring media the switching field of a hard magnetic layer is reduced by a soft magnetic layer that is exchange coupled to the hard layer. In the first step, a reverse domain is nucleated in the soft layer at a field H_N (see figure 2.5). The formation and expansion of the nucleation is reversible up to the third state from left in figure 2.5. In the second step the formed domain wall propagates to the soft/hard interface, where it becomes pinned. With

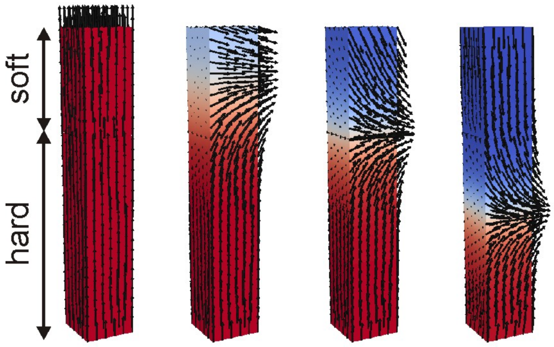

Figure 2.5: Reversal of a single bit consiting of 2 fully exchange coupled layers (exchange coupled composite media).

increasing external field strength the domain wall becomes compressed as shown in 2.5. The bilayer completely reverses when the external field is large enough to overcome the pinning field H_P. Therefore, the switching field of the entire grain is given by $H_\mathrm{S} = \max(H_\mathrm{N},\, H_\mathrm{P})$ [18]. Analytical expressions for H_P and H_N as well as approaches to manipulate these fields are discussed by Suess et al. [18]. Furthermore, Garcia-Sanchez et al. [41] studied the reversal process of magnetic bilayers using a multiscale approach, where the interface between the hard and soft layer is discretised atomistically. They found that strong coupling between the soft and the hard layer is required to obtain a maximum reduction of the switching field.

As a drawback of graded media, the relatively large thickness of about 20 nm is under debate [18]. As a consequence, alternative media design known as "synthetic antiferromagnet exchange coupled composite media" was proposed by Hernandez et al. [42]. A synthetic antiferromagnetic exchange coupled composite media could effectively reduce $M_\mathrm{s,hard}$ of the hard/soft composite structure, which is advantageous for reduction of the switching field of the entire composite. In this case, each grain consists of three layers: The top two layers are magnetically hard layers and they are antiferromagnetically exchange coupled to each other. The soft layer is ferromagnetically coupled to the centre hard layer, which functions the same as previously described. Simulations by Hernandez et al. [42] show that synthetic antiferromagnet exchange coupled composite media exhibit a high figure of merit that could only be achieved by graded anisotropy composite media, while avoiding use of low exchange stiffness material or very thick media.

Most of the presented studies on the ECC approach are performed on CoCrPt-based [43, 44] or Co/Pt(Pd)-based [45, 46] media, revealing superior properties compared to the single layer media. In line with theoretical predictions, advantage in switching field, switching field distribution, thermal stability and angular dependence of the switching field was demonstrated. In the following, experimental demonstration of the ECC media concept is presented. One of the earliest studies on FePt-based ECC approach was presented by [47]. Magnetically hard FePt films as well as the FePt/NiFe bilayers were grown by magnetron sputtering onto glass substrates with a 1.5 nm-thick Pt seed layer. The substrate temperature for the $\mathrm{Fe_{55}Pt_{45}}$ alloy deposition was maintained at 420°C. The FePt layer thickness was kept constant at 20 nm. High anisotropy $\mathrm{L1_0}$ FePt films with a coercive field of about 1 T were fabricated. Subsequently, a soft NiFe layer of various thicknesses ranging from $10 - 80$ nm was sputtered onto the FePt films at 150°C to avoid intermixing between the soft and hard layers. Magnetisation loops for selected FePt/NiFe(t nm) bilayer structures are shown in figure 2.6.

The coercivity of the composite films gradually decreases with increasing thickness t from about 0.18 T for $t = 10$ nm to about 0.01 T for $t = 80$ nm. For thicker NiFe layers, reverse domains nucleate in the film in low fields and then asymptotically approach saturation with increasing field. This behaviour is associated with a twisting of the magnetic moment of the soft layer as shown in figure 2.7.

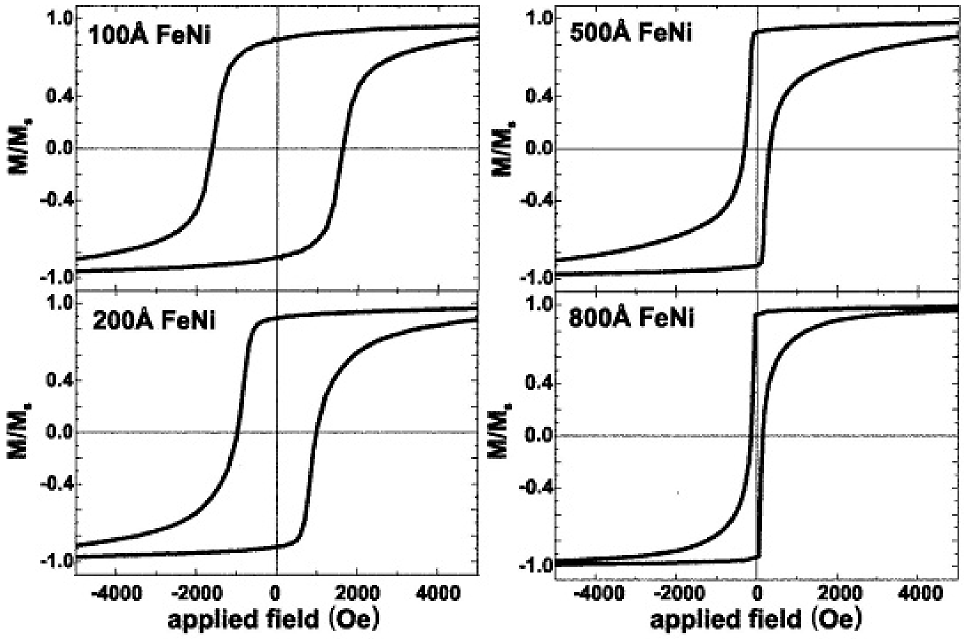

Figure 2.6: Magnetisation loops for selected FePt/NiFe(t nm) bilayer structures [47]. Please note that the figure was slightly modified from the original concerning the design.

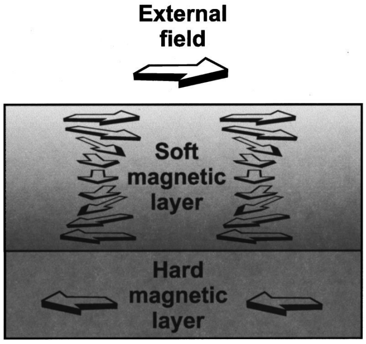

Figure 2.7: Twisting of the magnetic moment of the soft layer in soft/hard bilayer structures [47].

2.2.4 Thermally Assisted Magnetic Recording (TAMR)

Thermally assisted magnetic recording (TAMR - also called heat assisted magnetic recording - HAMR) can solve fundamental problems concerning the thermal energy barrier and writability issues. The idea behing thermally assisted magnetic recording is to locally reduce the necessary writefield for switching a magnetic bit using a focused laser beam. Due to the very small bit size, near-field optics have to be used to overcome the optical resolution limitation, which is half the wavelength of the used light. The idea is to use the dependency of the saturation magnetization and the magnetic anisotropy value from the temperature, $M_{\mathrm{S}}(T), K_{\mathrm{U}}(T)$. Figure 2.8 illustrates the relationship between coercivity H_{C} and temperature T, caused by the mentioned temperature dependency of M_{S} and K_{U} [12]. The thermally assisted magnetic recording can basically be

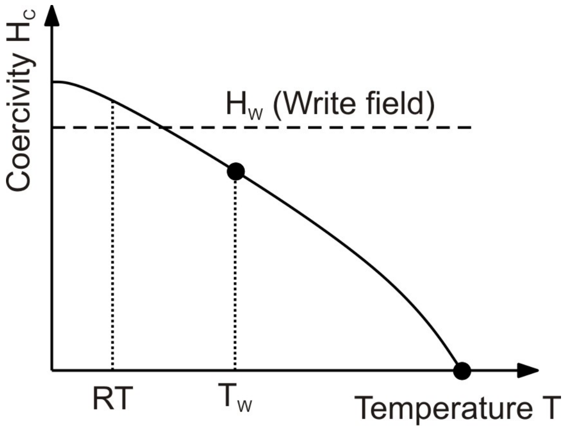

Figure 2.8: Relationship between coercivity H_C and temperature T. Moreover, the write field H_W, and the write temperature T_W are shown [12].

divided into two methods: (1) optical dominant magnetic recording, and (2) magnetic dominant magnetic recording. In the magnetic dominant magnetic recording, the write temperature T_W is the temperature at which the coercivity becomes slightly smaller than the maximum write field. In optical dominant magnetic recording, the write temperature is just below the CURIE temperature. The write field is relatively small because the coercivity decreases just below T_C.

Recently, a plasmonic nano-antenna that is fully integrated into a magnetic recording head and its use for thermally assisted magnetic recording on both continuous and fully-ordered patterned media using nanosecond pulses was demonstrated by B. STIPE et al. [48]. They have shown ideally written bits without disturbing neighbouring tracks in the case of patterned media at 1 Tb/inch^2 with 24 nm track pitch (see figure 2.9).

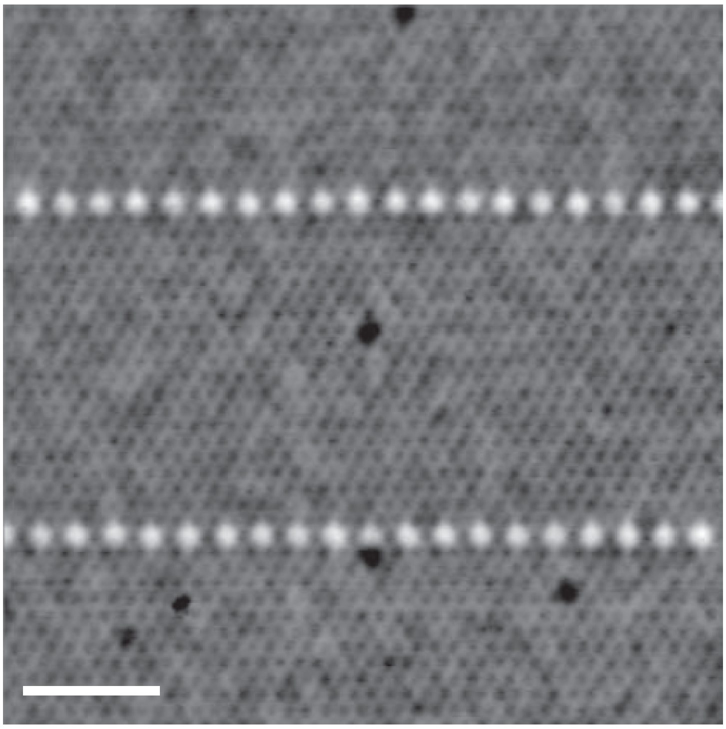

Figure 2.9: HR-MFM image of single-tone TAR tracks at 24 nm [48].

Chapter 3

Theoretical background

In the 1940s, W. F. BROWN published his first papers on the theory of micromagnetism of ferromagnetic materials and its application to the law of approach to ferromagnetic saturation [49]. This continuum theory closed the gap between the microscopic quantum theory of spin structures and MAXWELL's theory of electromagnetism. The big success of the theory of micromagnetism was due to several facts [50]:

- the analysis of domain structures in small particles and thin films
- the analysis of nucleation problems and magnetization processes
- the calculation of the spin structures of domain walls and spin singularities
- the interpretation of the characteristic parameters of the hystereis loops

The computer capabilities available nowadays make it possible to use numerical methods to solve otherwise unsolvable problems.

3.1 Gibbs Free Energy

The total energy of a micromagnetic system is given by the GIBBS free energy, E_{tot}, which depends on the magnetization polarisation, the external magnetic field and some (temperature dependent) material parameters. The GIBBS free energy includes both macroscopic contributions, such as the ZEEMAN energy, and the magnetostatic energy, as well as microscopic contributions, such as the magnetocristalline energy density, and the exchange energy density. These energies can be written as volume integral over energy densities, as follows:

$$\begin{aligned} E_{\mathrm{tot}} &= \int_{\Omega} (\epsilon_{\mathrm{exc}} + \epsilon_{\mathrm{ani}} + \epsilon_{\mathrm{ext}} + \epsilon_{\mathrm{magn}}) dV \qquad (3.1) \\ &= \int_{\Omega} \Big(A \left((\nabla \vec{m}_{\mathrm{x}})^2 + (\nabla \vec{m}_{\mathrm{y}})^2 + (\nabla \vec{m}_{\mathrm{z}})^2 \right) + K_{\mathrm{U}} (1 - (\vec{a} \cdot \vec{m})^2) \\ &\qquad - \vec{J} \cdot \vec{H}_{\mathrm{ext}} - \frac{1}{2} \vec{J} \cdot \vec{H}_{\mathrm{magn}} \Big) dV \qquad (3.2) \end{aligned}$$

with

$$\vec{J} = \mu_0 \vec{M}(\vec{r}, t) = \mu_0 M_\mathrm{S}(\vec{r}) \cdot \vec{m}(\vec{r}, t) \ , \qquad |\vec{m}| = 1 \tag{3.3}$$

Thereby, $\vec{J}$ is the magnetic polarisation, $\vec{M}$ the magnetization, A the exchange constant, K_U the first uniaxial magneto-crystalline anisotropy constant, $\vec{a}$ the unit vector parallel to the easy axis, $\vec{H}_\mathrm{ext}$ the external magnetic field, and $\vec{H}_\mathrm{magn}$ the magnetostatic (demagnetization) field. Thus, in equilibrium, the magnetization is parallel to an effective magnetic field $\vec{H}_\mathrm{eff}$:

$$\vec{H}_\mathrm{eff} = -\frac{1}{M_\mathrm{S}} \frac{\partial \epsilon_\mathrm{tot}}{\partial \vec{m}} = \frac{2A}{M_\mathrm{S}} \Delta \vec{m} + \frac{2K_\mathrm{U}}{M_\mathrm{S}} \vec{a}(\vec{m} \cdot \vec{a}) + \vec{H}_\mathrm{ext} + \vec{H}_\mathrm{magn} \tag{3.4}$$

Please note that magnetostrictive terms are not explicitely taken into account. It is assumed that the external field is independent of the magnetization distribution and the exchange and anisotropy energy are due to short range interactions, depending only on the local magnetization distribution. Thus, these energies can be computed quite efficiently. However, the magnetostatic field is a long-range interaction, which is the most expensive part in terms of memory and computation time requirements. Its calculation is usually based on a magnetic vector or scalar potential [51]. Moreover, it is an open boundary problem, for which various methods have been developed [52]. In the following section, a short introduction to the different energy terms and their calculation shall be given.

3.1.1 Exchange Energy

Please note that this derivation is based on the diploma thesis of W. SCHOLZ [53].

The HEISENBERG Hamiltonian $\mathbb{H}_\mathrm{exc}$ of the exchange interaction is usually written as [54]:

$$\mathbb{H}_\mathrm{exc} = -\frac{1}{2} \sum_{i,j=1}^{N} J_\mathrm{ij} \hat{S}_\mathrm{i} \cdot \hat{S}_\mathrm{j} \tag{3.5}$$

where J_ij is the exchange integral, $\hat{S}_\mathrm{i,j}$ are the spin operators, and N is the number of spins.

By using the fact that it is a short-range interaction, and by replacing the quantum mechanical operators with classical vectors, it can be modified to:

$$E_\mathrm{exc} = -\frac{1}{2} J S^2 \sum_{i,j|i \neq j} \cos(\Phi_\mathrm{i,j}) \tag{3.6}$$

By further assuming that the angles between two neighboring spins are small, cos can be expanded into its TAYLOR series expansion. Moreover, we take the sum for each pair of nearest neighbours only once and redefine the zero level of energy by removing the constant term. Thus, it follows:

$$E_\mathrm{exc} = J S^2 \sum_{i} \sum_{NN} \Phi_\mathrm{i,j}^2 \tag{3.7}$$

If we further use the continuous variable $\vec{m} = \frac{\vec{M}}{M_\mathrm{S}}$ for the magnetization, we get for small angles:

$$|\Phi_{\mathrm{i,j}}| \approx |\vec{m}_i - \vec{m}_j| \approx |(\vec{r}_\mathrm{i} \cdot \nabla)\vec{m}| \tag{3.8}$$

where $\vec{r}_\mathrm{i}$ is the position vector from lattice point i to j. Thus, the exchange energy can be written as:

$$E_\mathrm{exc} = JS^2 \sum_i \sum_{r_\mathrm{i}} ((\vec{r}_\mathrm{i} \cdot \nabla)\vec{m})^2 \tag{3.9}$$

Finally, we get:

$$\epsilon_\mathrm{exc} = A \left((\nabla \vec{m}_\mathrm{x})^2 + (\nabla \vec{m}_\mathrm{y})^2 + (\nabla \vec{m}_\mathrm{z})^2 \right) \tag{3.10}$$

with

$$A = \frac{JS^2 c}{d} \tag{3.11}$$

where d is the distance between nearest neighbors, and c depends on the crystalline structure ($c = 1, 2, 4$ for simple cubic, body centred cubic and face centred cubic crystal structure, respectively).

3.1.2 Magneto-cristalline Anisotropy Energy

Magneto-crystalline anisotropy is caused by the spin-orbit interaction of the electrons. The electron orbits are connected to the crystallographic structure, and by their interaction with the spins they make the latter prefer to align along well-defined crystallographic axes. Therefore, there are directions, in which a magnetic material is easier to magnetize than in others. The most common treatment of the magneto-crystalline anisotropy is a power series expansion taking into account the crystal symmetry and using coefficients from experiment.

In crystals the anisotropy energy is a function of only one parameter, which is the angle between the magnetization and the c-axis. In this case it is symmetric with respect to the base plane, and so odd powers of $\sin(\Phi)$ can be neglected in a power series expansion for the anisotropy energy density ϵ_ani. The first two terms of the energy density are thus:

$$\epsilon_\mathrm{ani} = K_\mathrm{U} \sin^2(\Phi) + K_2 \sin^4(\Phi) \tag{3.12}$$

It is also known from experiment that terms of higher order, and in most cases even K_2 are negligible. If $K_U > 0$, the c-axis is an easy axis, which means it is a direction of minimal energy. For $K_\mathrm{U} < 0$, it is a hard axis with an easy plane perpendicular to it.

Figure 3.1 shows the energy landscape plot of the magneto-crystalline anisotropy energy for a uniaxial system with easy-axis along the z-axis.

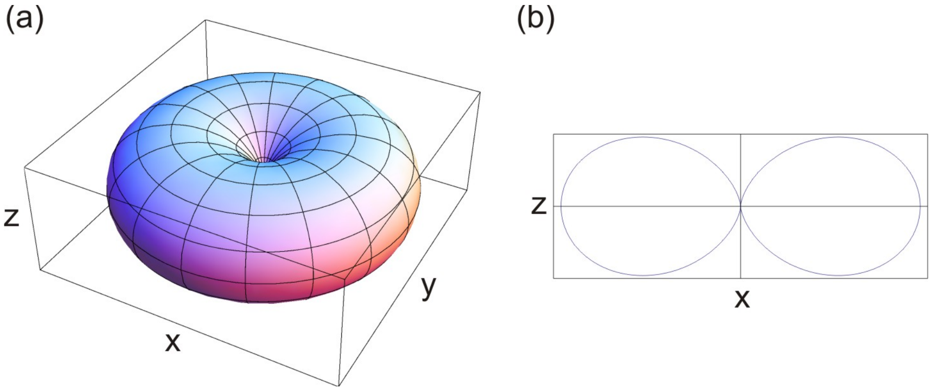

Figure 3.1: Energy landscape of the magneto-crystalline anisotropy energy for a uniaxial system with easy-axis along the z-axis. (a) 3D Plot (b) Cut through the x-z-plane.

3.1.3 Zeeman Energy

The Zeeman energy density of a magnetic body with magnetization $\vec{M}(\vec{r})$ in an external magnetic field $\vec{H}_{\text{ext}}(\vec{r})$ is given by:

$$\epsilon_{\text{ext}} = -\mu_0 \vec{M} \cdot \vec{H}_{\text{ext}} = -\vec{J} \cdot \vec{H}_{\text{ext}} \tag{3.13}$$

3.1.4 Magnetostatic Energy

The magnetostatic energy density is the energy most difficult to calculate due to its long-range nature. Its actual calculation includes solving an open boundary problem with one of its boundary condition at infinity. To overcome this issue, various methods, i.e. a combined hybrid finite element/boundary element method [55–57], have been proposed. Further information can be found in [58]. For the following, it shall be enough to mention that the magnetostatic energy density can be calculated as follows:

$$\epsilon_{\text{magn}} = -\frac{1}{2}\mu_0 \vec{H}_{\text{magn}} \cdot \vec{M} \tag{3.14}$$

Therefore, $\vec{H}_{\text{magn}}$ can be calculated using

$$\vec{H}_{\text{magn}} = -\nabla U \tag{3.15}$$

with U being the magnetic scalar potential [59]. Using the Maxwell equations, one gets for the magnetic scalar potential:

$$\Delta U_{\text{in}} = \nabla \cdot \vec{M} \tag{3.16}$$

$$\Delta U_{\text{out}} = 0 \tag{3.17}$$

with U_{in} and U_{out} being the magnetic scalar potential inside and outside of the magnetic body, respectively.

These equations have to be solved with the following boundary conditions:

$$\begin{aligned} U_{\text{in}} &= U_{\text{out}} && (3.18) \\ \frac{\partial U_{\text{in}}}{\partial \vec{n}} - \frac{\partial U_{\text{out}}}{\partial \vec{n}} &= \vec{M} \cdot \vec{n} && (3.19) \end{aligned}$$

on the surface of the magnetic body to obtain U and from U finally $\vec{H}_{\text{magn}}$. The boundary conditions make sure that the scalar magnetic potential and its first derivative is continuous at the surface of the magnetic body. Thereby, $\vec{n}$ is the unit vector normal to the surface of the magnetic body, pointing away from it.

3.1.5 Summary

The following statements can be summarized:

- The *exchange energy* gets minimized if magnetic moments close to each other are parallel. However, the exchange energy does neither depend on the global direction of the magnetization nor on the magnetic field.
- The *magneto-crystalline anisotropy energy* gets minimized if the magnetization is parallel (or anti-parallel) to the easy axis of a uniaxial system.
- The ZEEMAN *energy* gets minimized if the magnetization is parallel to the external magnetic field.
- The *magnetostatic energy* must be treated more sophisticated. However, in general it tries to align spins anti-parallel to each other (dipole-dipole interaction).
- In equilibrium, the magnetization is parallel to an effective magnetic field $\vec{H}_{\text{eff}}$:

$$\vec{H}_{\text{eff}} = -\frac{1}{M_{\text{S}}} \frac{\partial \epsilon_{\text{tot}}}{\partial \vec{m}} = \frac{2A}{M_{\text{S}}} \Delta m + \frac{2K_{\text{U}}}{M_{\text{S}}} \vec{a}(\vec{m} \cdot \vec{a}) + \vec{H}_{\text{ext}} + \vec{H}_{\text{magn}} \tag{3.20}$$

3.2 Finite Element Method

The finite element method (FEM) is a numerical technique for finding approximate solutions of partial differential equations as well as of integral equations. In the following, only a brief introduction to FEM will be given. The mathematical and physical background is for example given in [58, 60]. Whereas for simple geometries (e.g. an ellipsoid), an analytical solution of the micromagnetic equations is possible, there is no general solution for more complex geometries. One possible way is to divide the space in which the solution of a specific equation is needed in smaller parts, so-called cells. In the scope of this work, FEM was applied with tetrahedrons as cells. By choosing small enough cells, it is possible to assume that the solution of the equation under study is linear in each cell. By additionally taking into account that the solution must be continuous at the boundaries of the cells, it is possible to solve a given equation numerically. Figure 3.2 shows such a finite element mesh for a rectangular prism. In the frame of this work, the finite element meshing was performed using GiD, a universal, adaptive and user-friendly graphical interface for geometrical modelling, data input and visualisation of results for all types of numerical simulation programs [61]. One important parameter of a finite element model is the so-called mesh size, which represents the maximal one-dimensional size of a cell. The larger this value is, the less cells the model has and the faster the simulations are. On the other hand, the simulation results become more and more inaccurate the larger the mesh size is. Thus, a compromise between simulation time and accuracy needs to be found. As a general rule, the mesh size needs to be smaller than the smallest length scale that might occur in the solution of the equation. In micromagnetics, exchange length is a typical length scale. Dependent on the magnetic material parameters, the exchange length can be written as

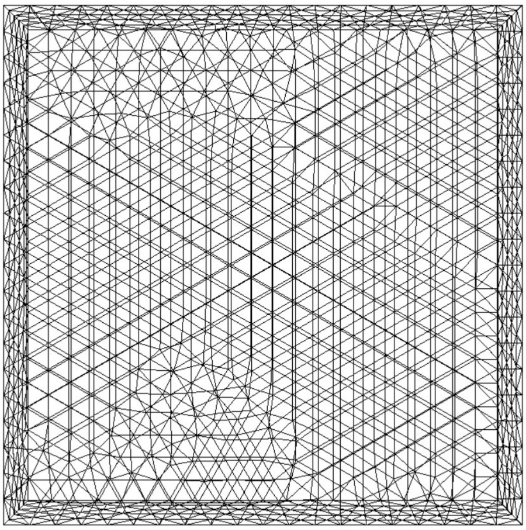

Figure 3.2: Example of a finite element model of a rectangular prism with a size of $(40 \times 40 \times 10)\ \mathrm{nm}^3$ and a mesh size of $2\,\mathrm{nm}$. Please note that the different mesh size at the edge of the image is solely due to perspective.

- $$l_{\mathrm{bex}} = \sqrt{\frac{A}{K_{\mathrm{U}}}}, \qquad \delta_{\mathrm{BW}} = \pi l_{\mathrm{bex}} \tag{3.21}$$

  with δ_{BW} being the width of a Bloch type domain wall.

- $$l_{\mathrm{nex}} = \sqrt{2\frac{A}{\mu_0 M_{\mathrm{S}}^2}}, \qquad \delta_{\mathrm{NW}} = \pi l_{\mathrm{nex}} \tag{3.22}$$

with δ_{NW} being the width of a Néel type domain wall and $K = \frac{M_{\mathrm{S}}^2}{2}$.

Table 3.1 gives an overview of characteristic magnetic properties and Bloch and Néel domain wall width of different magnetic materials. The exchange constant was always assumed to be $A = 1 \times 10^{-6}$ ergs/cm. Please note that a discussion about different domain wall types can be found in 3.4.2.

Material	K_{U} [10^7ergs/cm]	M_{S} [kG]	δ_{BW} [nm]	δ_{NW} [nm]
Co/Pt-multilayer [62]	up to 1.0	up to 10	10	15.7
$\mathrm{Co_3Pt}$ [63]	2.0	14	6.9	11
$L1_0$ CoPt [63]	4.9	10	4.4	15.7
$L1_0$ FePt [63]	6.6	14	3.8	10.7
$\mathrm{SmCo_5}$ [64]	15	13	2.5	10.9
CoCrPt [65]	0.35	6.5	17	23

Table 3.1: Different magnetic materials and their characteristic magnetic properties and Bloch and Néel domain wall lengths. Please note that whereas for CoCrPt the intergranular exchange constant is in the region of about $A_{\mathrm{inter}} = 1 \times 10^{-9}$ ergs/cm, the exchange constant within one grain is still about $A_{\mathrm{inner}} = 1 \times 10^{-6}$ ergs/cm.

3.3 Solution of the Micromagnetic Equations

After introducing both, the Gibbs free energy and the finite element method, it is now possible to outline the basic idea of the solution of the micromagnetic equations. In general, there are two cases: the static and the dynamic one. In the static case, one is interested in the equilibrium magnetization distributions in a magnetic body. In the dynamic case, one is also interested in the way the magnetization changes over time. Within the scope of this work, the micromagnetic solvers *magpar* for the static case and *femme* for the dynamic case were used [58, 66]. In the following section, a brief introduction to both cases shall be given.

3.3.1 Static Case: Energy Minimization

In the static case, a minimization of the Gibbs free energy function is used to calculate the equilibrium magnetization states of a given system. Therefore, the energy and the energy gradient of a system are calculated. To consider the constraint that the absolute value of the magnetization in each cell

$$\vec{M}_{\mathrm{i}}(\vec{x}) = M_{\mathrm{S}} \begin{pmatrix} m_{\mathrm{x,i}} \\ m_{\mathrm{y,i}} \\ m_{\mathrm{z,i}} \end{pmatrix} \tag{3.23}$$

must be constant, the energy gradient is calculated in spherical coordinates $\theta_\mathrm{i} \in [0;\pi), \varphi_\mathrm{i} \in [0;2\pi)$:

$$\begin{pmatrix} \theta_\mathrm{i} \\ \varphi_\mathrm{i} \end{pmatrix} = \begin{pmatrix} \arccos(m_\mathrm{z,i}) \\ \arctan(m_\mathrm{y,i}/m_\mathrm{x,i}) \end{pmatrix} \tag{3.24}$$

This has also the advantage that the number of variables reduces from three to two, significantly decreasing the computational time.

The minimizing itself is then performed using the limited memory variable metric (LMVM) algorithm of the TAO package [67], as implemented in *magpar*.

3.3.2 Dynamic Case: The Landau-Lifshitz-Gilbert (LLG) equation

The minimization of the GIBBS free energy function can find an equilibrium magnetization distribution. However, the energy landscape of micromagnetic systems is usually complicated and contains many local extrema. Therefore, the choice of the initial magnetization distribution has a strong influence on the result. A more physical approach to the problem and a more realistic approach to bring the system to its equilibrium in a local minimum is provided by a dynamic description of the path through the energy landscape. The motion of a magnetic moment in a magnetic field is mainly governed by its LARMOR precession around the local magnetic field, determining the necessary time step for solving the LLG numerically. The damping of the motion causes the relaxation to equilibrium. There are many processes which contribute to the damping in a magnetic solid like magnon-magnon and magnon-phonon interactions, interactions between localized and itinerant electrons [68, 69].

The LANDAU-LIFSHITZ-GILBERT equation (LLG) [70, 71] named for L. LANDAU, E. LIFSHITZ, and T. L. GILBERT, is a name used for a differential equation describing the precessional motion of magnetization $\vec{M}$ in a solid. It is a modification by GILBERT of the original equation of LANDAU and LIFSHITZ. One possible formulation of the LLG is as follows:

$$\frac{\partial \vec{m}}{\partial t} = -\gamma \vec{m} \times \vec{H}_\mathrm{eff} + \alpha \vec{m} \times \frac{\partial \vec{m}}{\partial t} \tag{3.25}$$

with $\vec{m} = \vec{M}/M_\mathrm{S}$ being the normalized magnetization, $\vec{H}_\mathrm{eff}$ the effective magnetic field, γ the gyromagnetic ratio, and α the LANDAU-LIFSHITZ-GILBERT damping. Thereby, the first term on the right hand side is the precession around the local effective field, $d\vec{M}_\mathrm{P}$, and the second term on the right hand side the relaxation to equilibrium, $d\vec{M}_\mathrm{R}$ (figure 3.3). An example is the relaxation process of a single macrospin towards its equilibrium magnetization from an initially tilted magnetization direction. Figure 3.4 shows such a relaxation process of a macrospin from the initial position $(0.57, 0.57, 0.57)$ towards the easy axis of magnetization, $(0, 0, 1)$. Moreover, the LARMOR-frequency ω_L, defined as

$$\omega_\mathrm{L} = -\gamma \cdot \mu_0 H, \tag{3.26}$$

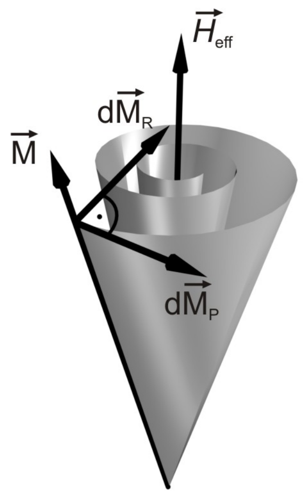

Figure 3.3: Illustration of the different terms of the Landau-Lifshitz-Gilbert equation: precession $d\vec{M}_{\mathrm{P}}$ and relaxation $d\vec{M}_{\mathrm{R}}$

is shown. In this case, the magnetic field H is the effective magnetic field H_{eff}.

3.4 Magnetization Reversal

In this section, the magnetization reversal of a single-phase magnet shall be discussed, beginning with the description of a hysteresis loop and of different types of domain walls. In this context, different properties of a magnet, as for example the coercive field and saturation magnetization, will be introduced.

3.4.1 Magnetization loops

A hysteresis loop describes the relation between magnetization, M, and applied magnetic field, H. Figure 3.5 shows a hysteresis loop of a uniaxial magnet. Additionally, the coercive field, H_{C}, the saturation magnetization, M_{S}, the remanent magnetization, M_{R}, and the switching field distribution, SFD, is shown. Please note that the switching field distribution was defined as the difference between the field at which the magnetization is dropped to 90% and the field at which the magnetization is at −90%. Moreover, the nucleation field, H_{N}, (not shown) is defined as the field at which reverse magnetic domains begin to nucleate.

Contrary to the hysteresis loop that describes the magnetization of a magnetic body in an applied field, the so-called *remanent curve* describes the magnetization of a magnetic body at remanence. Therefore, the magnet gets at first saturated in a large positive magnetic field. Afterwards, a reversed magnetic field H_{R} is applied to the magnet. Finally, the magnetic field is turned off and the magnetization relaxes to its remanent magnetization M_{R}. The remanent

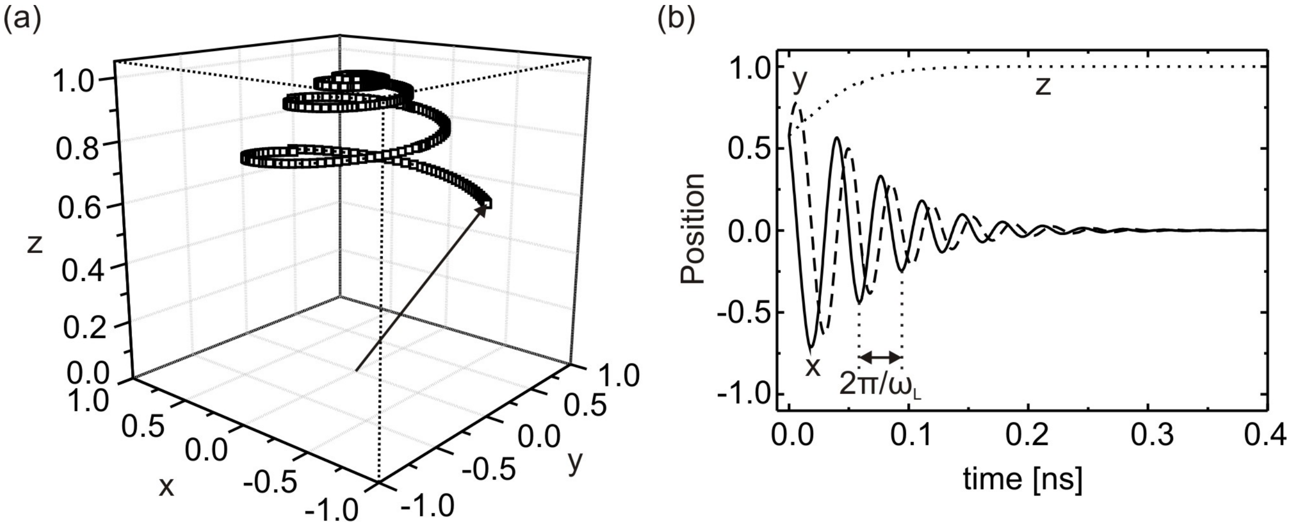

Figure 3.4: Relaxation process of a macrospin from the initial position $(0.57, 0.57, 0.57)$ towards the easy axis of magnetization, $(0, 0, 1)$. (a) shows the trajectory, whereas (b) shows the independent components.

curve is then $M_{\mathrm{R}}(H_{\mathrm{R}})$. The field at which $M_{\mathrm{R}} = 0$ in the remanent loop is typically defining the switching field of the magnet.

3.4.2 Magnetic domain walls

The region in which the magnetization of a magnetic body changes from one direction to the opposite direction is called domain wall. There are several types of domain walls [72], whereas the two most common types are the BLOCH and the NÉEL domain wall. The energies needed to built those domain walls are as follows:

$$\text{BLOCH domain wall: } \epsilon_{\mathrm{BW}} = 4\sqrt{AK_{\mathrm{U}}} \tag{3.27}$$

$$\text{NÉEL domain wall: } \epsilon_{\mathrm{NW}} = 4\sqrt{\frac{\mu_0 A M_{\mathrm{S}}^2}{2}} \tag{3.28}$$

The corresponding domain wall widths are:

$$\delta_{\mathrm{BW}} = \pi\sqrt{A/K_{\mathrm{U}}} \tag{3.29}$$

$$\delta_{\mathrm{NW}} = \pi\sqrt{\frac{2A}{M_{\mathrm{S}}^2 \mu_0}} \tag{3.30}$$

Figure 3.6 shows the structure of the BLOCH and NÉEL domain wall. In a BLOCH domain wall, the magnetization changes by rotation with the rotational plane being perpendicular to the direction of the magnetization changes. In a NÉEL domain wall, the rotational plane is parallel to the direction of the magnetization changes.

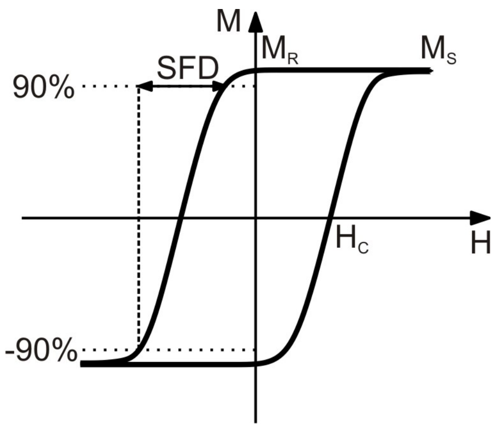

Figure 3.5: Hysteresis loop of an uniaxial magnetic body. Additionally, the coercive field, H_{C}, the saturation magnetization, M_{S}, the remanent magnetization, M_{R}, and the switching field distribution SFD is shown. Please note that the switching field distribution is usually defined as the difference between the field at which the magnetization is dropped to 90% and the field at which the magnetization is at -90%.

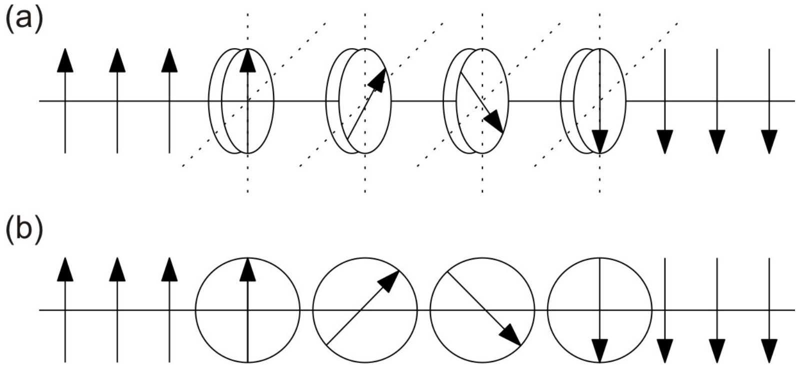

Figure 3.6: Structure of a (a) BLOCH and (b) NÉEL domain wall.

The creation of the different types of domain walls depends on the thickness of the film and on the magnetic properties: for a film thickness $t < t_{\text{crit}}$, a NÉEL domain wall is built, for a film thickness $t > t_{\text{crit}}$, a BLOCH domain wall is built.

3.4.3 Magnetization reversal modes

The way the magnetization of a magnetic body changes from positive to negative saturation depends on various magnetic and structural properties. For a perfect ellipsoid with uniaxial magnetic anisotropy, the reversal mode depends on the lateral dimension of the ellipsoid. Figure 3.7 shows the nucleation field for a sphere as a function of the diameter for different reversal modes. For a diameter smaller than D_{th}, the nucleation field gets reduced due to the instability of the magnetic moment against thermal exitation, the so-called *superparamagnetism.* For $D_{\text{th}} < D < D_{\text{crit}}^{\text{inh}}$, the reversal happens through coherent rotation of magnetization, meaning that at all time during the magnetization reversal process, all magnetic moments are parallel to

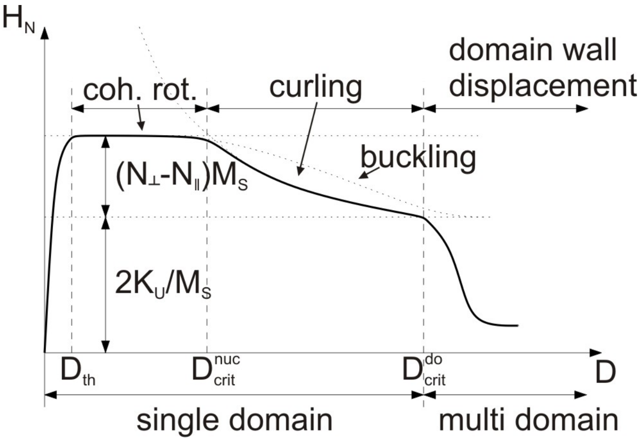

Figure 3.7: Review of the nucleation fields of different magnetization reversal modes [50].

each other. This reversal mode means a win of exchange energy, in expense of magnetostatic, Zeeman, and anisotropy energy, as at a certain point during the reversal, all magnetic moments are perpendicular to the easy-axis and to the external magnetic field, maximizing the mentioned energies. With increasing lateral size, for $D^{\mathrm{inh}}_{\mathrm{crit}} < D < D^{\mathrm{do}}_{\mathrm{crit}}$, the reversal mode changes to inhomogeneous rotation, e.g. curling or buckling. Those reversal modes are more complex in terms of spatial spin configuration. However, the change from coherent rotation of magnetization to e.g. curling goes ahead with a loose in exchange energy but with a gain in the other energy contributions [50].

3.4.3.1 Coherent magnetization rotation - The Stoner-Wohlfarth model

In the case of a very small particles (or a macrospin) with uniaxial anisotropy, an analytical formulism, the so-called Stoner-Wohlfarth model (SW model) exists for describing magnetization reversal of the particles. Figure 3.8 shows (a) the theoretical reversal of a macrospin and (b) a micromagnetic simulation of a cube with side length of 10 nm and magnetic properties close to the one of Co/Pt-multilayers: $K_{\mathrm{U}} = 3 \times 10^6\,\mathrm{ergs/cm^3}$ and $M_{\mathrm{S}} = 6\,\mathrm{kG}$. The Landau-Lifshitz-Gilbert damping constant was set to 0.2.

The hysteresis loop of such a particle with the external magnetic field applied under an angle of 0° relative to the easy-axis has a squareness of 1 and a nucleation field H_{N} of [50]:

$$H_{\mathrm{N}} = \alpha_{\mathrm{SW}} \left(\frac{2K_{\mathrm{U}}}{\mu_0 M_{\mathrm{S}}} - (N_{\perp} - N_{\|}) M_{\mathrm{S}} \right) \tag{3.31}$$

with $N_{\perp}$ and $N_{\|}$ being the perpendicular and parallel demagnetization factors, respectively. The prefactor α_{SW} is 1 for a SW particle and an applied magnetic field under an angle of 0°. It is important to emphasize that equation 3.31 is only valid in the case of coherent magnetization rotation.

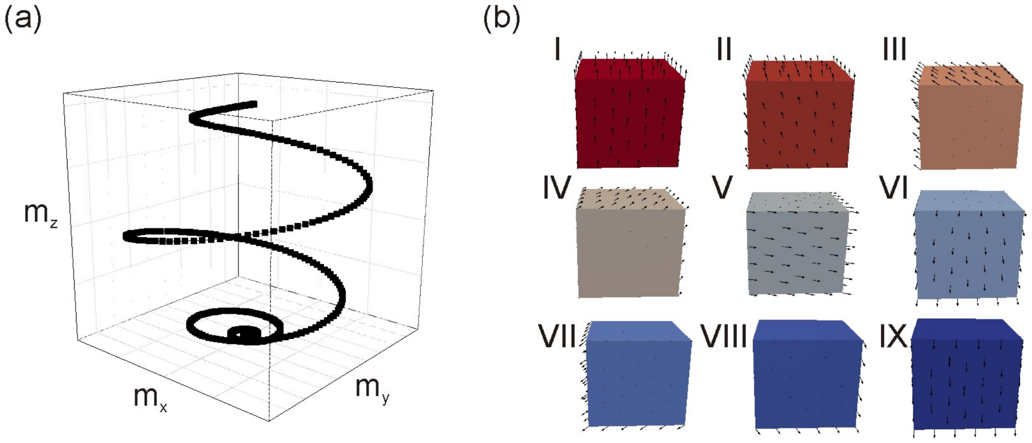

Figure 3.8: (a) Trajectory of the theoretical magnetization rotation of a macrospin in an applied magnetic field (b) Micromagnetic simulation of the magnetization reversal of a cube with side length of 10 nm and $K_\mathrm{U} = 3 \times 10^6$ ergs/cm^3 and $M_\mathrm{S} = 6\,\mathrm{kG}$ [73].

If the external magnetic field is not applied under an angle of 0° relative to the easy-axis but under an angle Φ_0, the prefactor α_SW from equation 3.31 changes to [50]:

$$\alpha_\mathrm{SW} = \frac{1}{(\cos(\Phi_0)^{2/3} + \sin(\Phi_0)^{2/3})^{3/2}} \tag{3.32}$$

Figure 3.9 shows the angular dependence of the nucleation field of a SW particle, calculated according to 3.32. Additionally, the angular dependence of the coercive field is shown aswell. The coercive and nucleation field are normalized to the respective field at $\Phi_0 = 0°$.

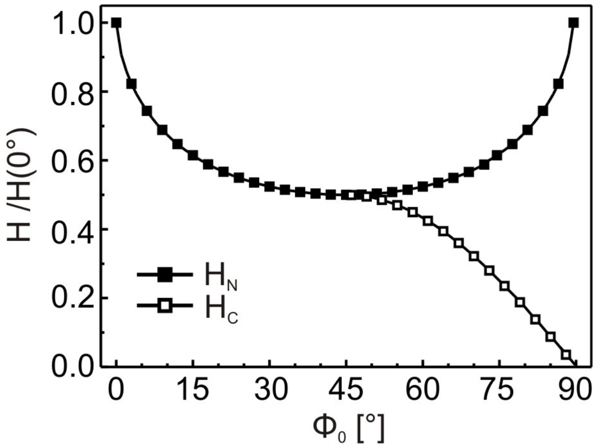

Figure 3.9: Angular dependence of the nucleation and coercive field of a SW particle. Please note that the coercive and nucleation field are normalized to the respective field at $\Phi_0 = 0°$.

Up to $\Phi_0 = 45°$, both the coercive and nucleation field decrease down to $0.5H(0°)$ at $\Phi_0 = 45°$. With further increasing field angle, the nucleation field increases up to its initial value at $\Phi_0 = 90°$, whereas the coercive field further decreases down to 0 at $\Phi_0 = 90°$. The analytical formula describing the behaviour of the coercive field for $\Phi_0 > 45°$ is as follows [72]:

$$\alpha_{\mathrm{SW,coerc}} = \sin(\Phi_0) \cdot \cos(\Phi_0) \tag{3.33}$$

Please note that not only single-domain particles that reverse their magnetization via coherent rotation show such an angular dependence of the nucleation field. Indeed, it is already sufficient for a magnetic body that there is no *stable* multi-domain configuration during the magnetization reversal process to show a Stoner-Wohlfarth angular dependence of the nucleation field [74]. Figure 3.10 shows magnetic states of a film with a size of $(200 \times 200 \times 9)\,\mathrm{nm}^3$ that reverses its magnetization via domain wall nucleation and propagation. The same magnetic properties as in the simulation above were used: $K_\mathrm{U} = 3 \times 10^6\,\mathrm{ergs/cm}^3$, $M_\mathrm{S} = 6\,\mathrm{kG}$, and $\alpha = 0.2$.

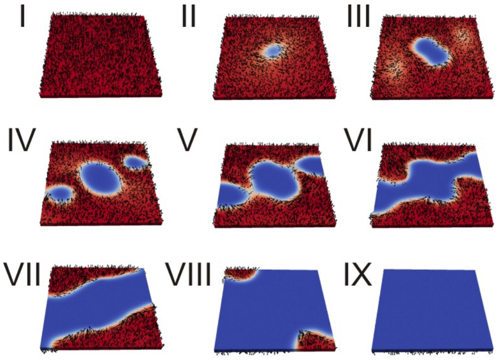

Figure 3.10: Micromagnetic simulation of the magnetization reversal of a film with the size of $(200 \times 200 \times 9)\,\mathrm{nm}^3$ and $K_\mathrm{U} = 3 \times 10^6\,\mathrm{ergs/cm}^3$ and $M_\mathrm{S} = 6\,\mathrm{kG}$.

In this case, a domain is created in the middle of the film and successively propagates throughout the entire film. This systems shows the same Stoner-Wohlfarth like angular dependence of the nucleation field as discussed above.

3.4.3.2 Inhomogeneous magnetization rotation

With increasing size of the particle, the magnetization reversal mode changes from coherent rotation of magnetization to inhomogeneous magnetization reversal. Such an inhomogeneous magnetization reversal can be buckling, curling, or the creation of an vortex-antivortex-pair and its respective annihilation. Those more complex magnetization reversal modes shall not be discussed in more detail in this work, however, further information can be found in [50].

3.4.3.3 Domain wall nucleation and propagation - The Kondorsky model

The domain wall propagation, as derived by Kondorsky describes the case where a domain is pushed through the film by an external field. The angular dependence of the nucleation field in this case was derived by KONDORSKY [75]:

$$H_{\mathrm{N}}(\Phi_0) = \frac{H_{\mathrm{N}}(\Phi_0 = 0°)}{\cos(\Phi_0)} \tag{3.34}$$

This so-called KONDORSKY behaviour is illustrated in Fig. 3.11, together with the SW model for comparison.

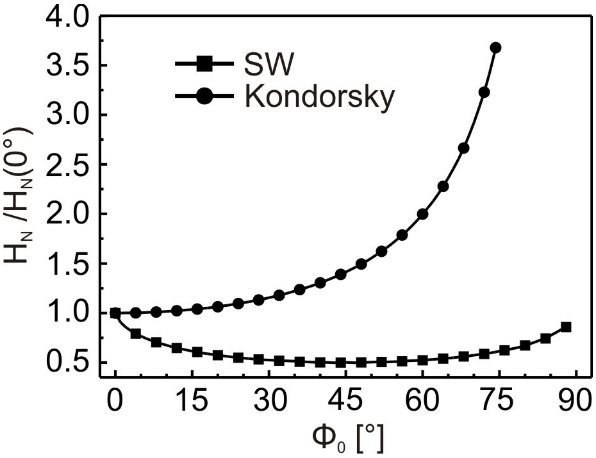

Figure 3.11: Angular dependence of the nucleation field for the KONDORSKY model of domain wall nucleation and propagation. Additionally, the curve for the SW model was added for comparison. Please note that the nucleation fields are normalized to the nucleation fields at $\Phi_0 = 0°$.

3.5 Magnetic energy barrier

One important property of a magnetic body is the energy necessary to change the magnetization from state $\vec{m}_1$ to $\vec{m}_2$. This property is given by the *(magnetic) energy barrier* ΔE. The energy barrier determines the thermal stability and thus the lifetime τ of a magnetic state, following the ARRHENIUS law [50]:

$$\tau = \tau_0 \exp\left(\frac{K_{\mathrm{eff}} V}{k_{\mathrm{B}} T}\right) \tag{3.35}$$

with τ_0 being the attempt frequency ($\approx 1 \times 10^{-11}\,\mathrm{s}$), K_{eff} the effective magnetic anisotropy constant, V the volume of the particle, and T the temperature; k_{B} is the BOLTZMANN constant. For example in magnetic recording, the lifetime of an individual bit shall be $>$ 10 years, leading to an energy barrier of $\Delta E > 60\mathrm{k_B}T$ [76].

In the case of a system with uniaxial magnetic anisotropy and coherent rotation of magnetization, the energy barrier at zero external field can be calculated as follows:

$$\Delta E = K_{\mathrm{eff}} V \tag{3.36}$$

The effective magnetic anisotropy constant can be written as:

$$K_{\mathrm{eff}} = (K_{\mathrm{U}} + {}^{1}\!/\!{}_{2}\mu_0 M_{\mathrm{S}}^2 (N_\perp - N_{||})) \tag{3.37}$$

with K_{U} being the magnetic anisotropy constant, M_{S} the saturation magnetization, and $N_\perp$ and $N_{||}$ the perpendicular and parallel demagnetization factor, respectively. Finally, the demagnetization factors can be written as:

$$(N_\perp - N_{||}) = {}^{1}\!/\!{}_{2}(1 - 3N_{\mathrm{eff}}) \tag{3.38}$$

with N_{eff} being the effective demagnetization factor in the case of a magnet with a symmetry in the plane perpendicular to the magnetic field vector. This finally leads to the expression for the energy barrier of a particle with uniaxial magnetic anisotropy that reverses its magnetization via coherent rotation:

$$\Delta E = (K_{\mathrm{U}} + {}^{1}\!/\!{}_{4}\mu_0 M_{\mathrm{S}}^2 (1 - 3N_{\mathrm{eff}}))V \tag{3.39}$$

The effective demagnetization factor is a value between 0 and 1 depending on the geometry of the particle and the direction of the applied magnetic field. For example a sphere has an effective demagnetization factor of $^{1}\!/\!_{3}$ and a flat film with magnetic field applied parallel to the surface normal of 1.

3.5.1 The Nudged Elastic Band Method

In order to calculate the energy barrier of micromagnetic system, sophisticated methods have to be applied. The most obvious method, i.e. to simulate a magnet at a given temperature until the magnetization is switched is not possible due to computational limitations (the switching can take up to several years, whereas the simulation time is usually in the region of 200 ns). The energy barrier is defined as the minimal energy needed to change the magnetization from an initial magnetic state M_{i} to a final magnetic state M_{f}. Henkelman and Jonsson proposed the nudged elastic band method (NEB) to calculate these minimal energy paths [77]. Figure 3.12 shows an example of a minimal energy path.

The description of the nudged elastic band method is adopted from Scholz [58]. The path is represented by a sequence of "images" (magnetization distributions), which connects the two given stable equilibrium states $\vec{M}_{\mathrm{i}}$ and $\vec{M}_{\mathrm{f}}$. The first sequence is given by the initial magnetization distribution $\vec{M}_{\mathrm{i}}$ and the final magnetization distribution $\vec{M}_{\mathrm{f}}$ and a number of images $\vec{M}_{\mathrm{k}}$ in between, which can for example be obtained by linear interpolation. Then, an optimization algorithm is applied, which moves the "elastic band of images" through the energy landscape towards the optimal path, which is defined by:

$$(\nabla E(\vec{M}_{\mathrm{k}}) \cdot \vec{t})\vec{t} = \nabla E(\vec{M}_{\mathrm{k}}) \tag{3.40}$$

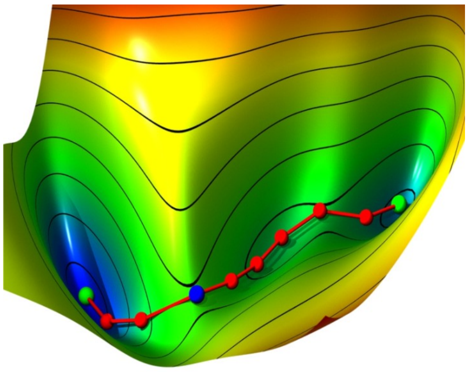

Figure 3.12: Example of a minimum energy path from one energy minimum to another (green spheres), going over a saddle point (blue sphere) [78]

with $\nabla E(\vec{M}_{\mathrm{k}})$ being the gradient of the total energy at image $\vec{M}_{\mathrm{k}}$ and $\vec{t}$ is the unit tangent vector along the path. In order to avoid kinks in the path the tangent is calculated using forward, backward, or second order central differences. Equation 3.40 requires the component of the gradient parallel to the tangent to be equal to the gradient. In other words, the optimal path is characterized by the fact that the gradient of the total energy is parallel to the tangent for any image $\vec{M}_{\mathrm{k}}$.

Starting from the initial path an iterative optimization scheme is applied, which moves the images $\vec{M}_{\mathrm{k}}$ in a direction $\vec{D}(\vec{M}_{\mathrm{k}})$, which is given by:

$$\vec{D}(\vec{M}_{\mathrm{k}}) = -\left(\nabla E(\vec{M}_{\mathrm{k}}) - (\nabla E(\vec{M}_{\mathrm{k}}) \cdot \vec{t})\vec{t}\right) \tag{3.41}$$

The interpretation of this expression is as follows: The images are moved along the negative gradient of the total energy perpendicular to the tangent. The negative gradient determines the direction towards lower energy while the distance between the images is preserved by taking only the component perpendicular to the tangent. Thus, an ordinary differential equation can be formulated:

$$\frac{\partial \vec{M}_{\mathrm{k}}}{\partial t} = \vec{D}(\vec{M}_{\mathrm{k}}) \tag{3.42}$$

where t denotes some artificial time parameter, which is integrated using any ordinary differential equation solver.

Chapter 4

Experimental techniques

In the scope of this work, the thin films were prepared using sputter deposition and molecular beam epitaxy (MBE) techniques. The investigation was performed using superconduction quantum interference device (SQUID), magneto optical KERR effect, and magnetic force microscopy. In the following, those techniques shall be briefly explained.

4.1 Magnetron sputter deposition

The magnetron sputter deposition is an important technique for producing thin films. The CoCrPt:SiO_2 films used in this work were sputter deposited at Oerlikon Balzers AG (Balzers, Lichtenstein) in collaboration with F. Springer and H. Rohrmann. In the following, basic principles of magnetic sputtering will be presented. Figure 4.1 shows the commercially available sputter machine *RACETRACK* from *OC Oerlikon Balzers AG*, which is intended to produce about 1000 hard discs per hour. As sputter gas, argon with a purity of 99.999% was used at a

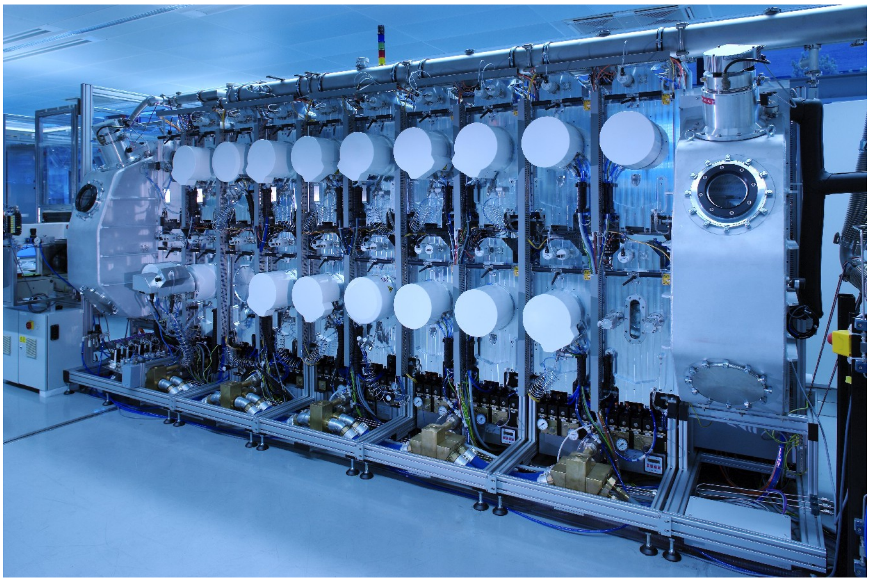

Figure 4.1: Photo of the *RACETRACK* sputter system at the OC Oerlikon Balzers AG [79].

pressure of about 20 mTor. In the *RACETRACK* machine, several magnetrons were used. Figure 4.2 shows a three dimensional illustration of a magnetron. A magnetron consists of a target which holds the element or alloy that shall get sputtered. Under the target, there is a magnet system with a cylindrical magnet in the middle and a ring magnet around it. By applying a voltage between target and anode, the ions in the argon gas begin to move towards the target. Once hitting the target, both secondary electrons and target material are extracted out of the target. The secondary electrons then move under the influence of the magnetic field from the magnet system and the electrical field from the target in a cycloid above the target (Fig. 4.2, *plasmatorus*) and ionise new argon atoms that again move towards the target. This way, more and more target material is extracted, building the film.

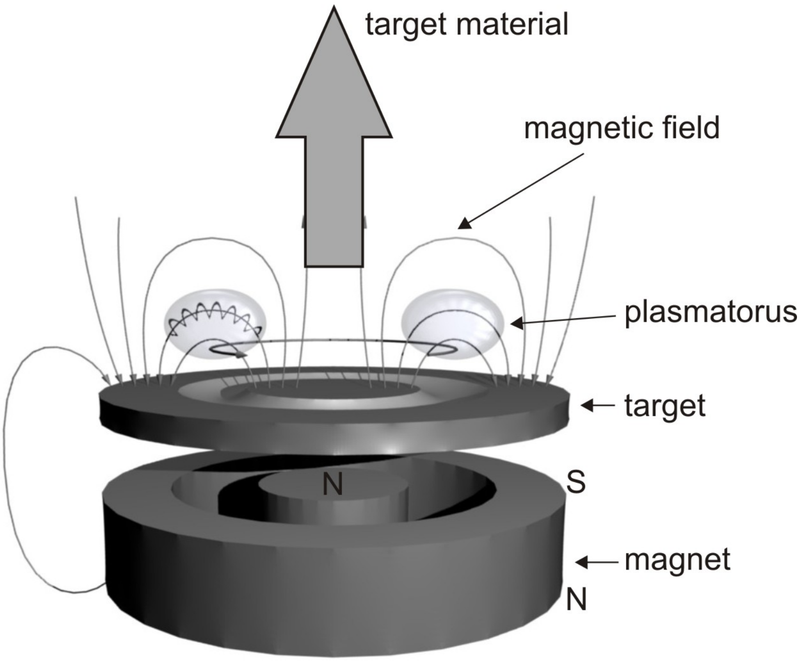

Figure 4.2: Illustration of a magnetron.

4.2 Molecular beam epitaxy

The Co/Pt multilayer films used in the frame of this work were prepared by molecular beam deposition. Molecular beam deposition (MBD) is a method for depositing thin films under ultra high vacuum conditions. The most important aspect of MBE is the slow deposition rate (typically 0.1 Å), which allows the films to grow epitaxially on suitable substrates. The slow deposition rates require ultra high vacuum to achieve the same impurity levels as other deposition techniques, as for example magnetron sputter deposition.

Figure 4.3 shows the used MBE chamber *SGC600* from *DCA*. The MBE machine consists of 4 chambers: (1) the load lock (with turbomolecular pump and prepump), (2) the transferring chamber (with ion getter pump), (3) the deposition chamber (with cryo and sublimation pump), and (4) the LEED/AES chamber (with ion getter pump). Please note that LEED/AES was not used in the frame of this work. The base pressure in the deposition chamber was as low as 4×10^{-11} mbar, the pressure during deposition was about 4×10^{-9} mbar. The *Co* and *Pt* (purity larger than 99.99%) was deposited using an electron beam evaporator.

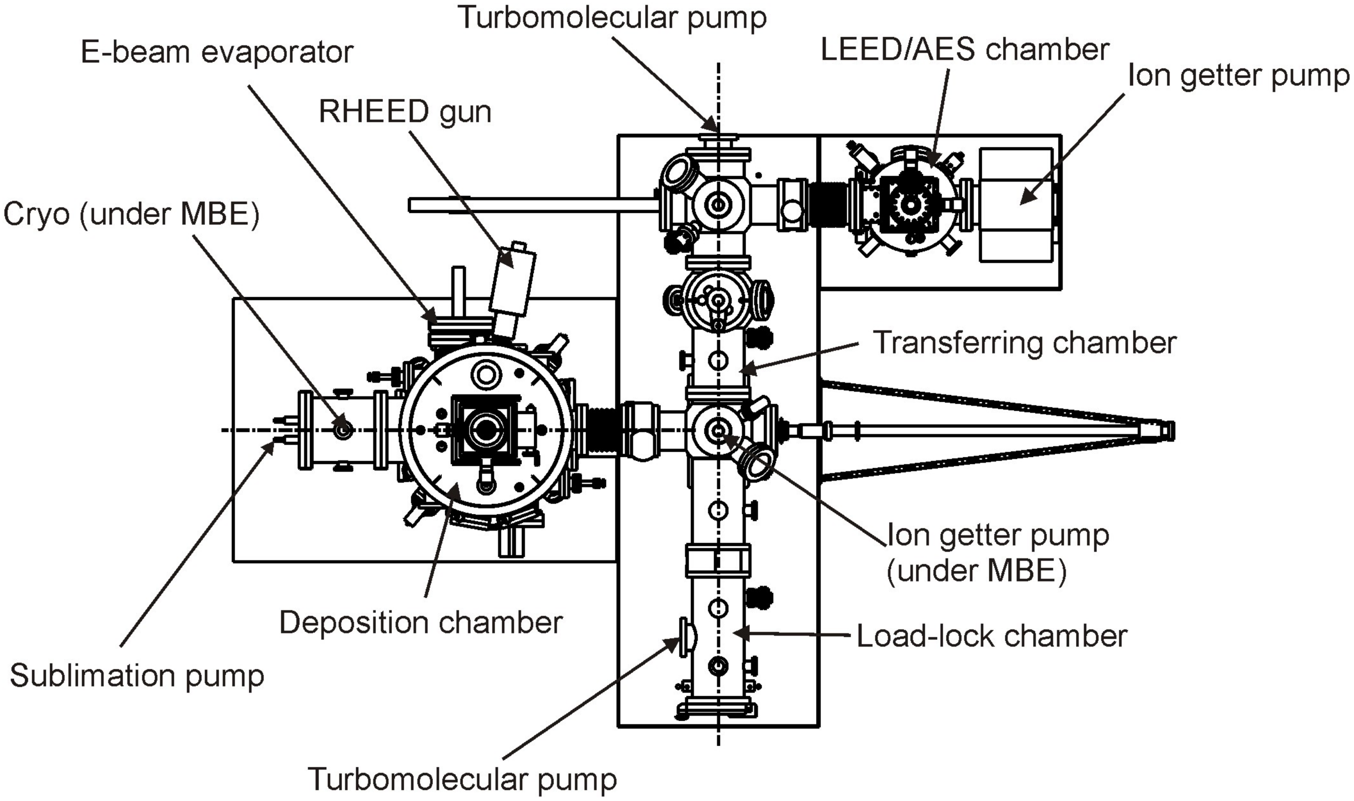

Figure 4.3: Functional principle of the used MBE chamber.

4.3 Self-assembly of particle monolayers

The self-assembly of particle monolayers was performed by C. Brombacher during his diploma work [79]. The basics of this procedure was developed by F. Burmeister [80]. A 5−10 μl drop of a colloidal solution of nanoparticles was put on a substrate. Afterwards, the solution evaporated in a drying box under an angle of approximately 9°, leading to an beginning of the evaporation at one side of the droplet, significantly increasing the order of the nanoparticles. In the frame of this work, SiO_2 particles with sizes from 10 up to 330 nm were used. The particles were bought as a water-particle suspension from *Bangs Laboratories* (sizes of 160 and 330 nm) and *Polysciences* (sizes of $10, 50$, and 100 nm).

4.4 SQUID magnetometry

The SQUID magnetometer (superconduction quantum interference device) is the most sensible tool for measuring changes in a magnetic field with an accuracy down to 1Oe [81]. The functionality is based on two physical principles:

- quantization of the magnetic flux in a superconducting ring.
- JOSEPHSON-effect, which describes the tunneling process of COOPER pairs through a normal conductor in between two superconductors.

In general, there are two types of SQUIDs:

- AC-SQUID:
    a) operated under alternating voltage.
    b) works with only one JOSEPHSON contact, however, the alternating voltage has to be coupled in using a coil.
- DC-SQUID:
    a) operated under direct current voltage
    b) works with two JOSEPHSON contacts, the voltage can be applied directly

In the following, a short description of the DC-SQUID shall be given. Figure 4.4 shows a functional principle of a DC-SQUID. Because of the quantization, the magnetic flux in the superconductor can only be a multiple of the fluxon $\Phi_0 = \frac{h}{2e} = 2.07 \times 10^{-15}\,\mathrm{Vs}$:

$$\Phi = n \cdot \Phi_0 \tag{4.1}$$

A sufficient large change in the external magnetic field induces a circular current in the superconductor, leading to an increase or decrease of the magnetic flux by one fluxon. To detect those changes, there are two JOSEPHSON contacts in the superconductor. If there is a current in the ring, which is larger than the critical current I_C of both JOSEPHSON contacts, a voltage can be measured at the ring elements, which correlates to the maximal possible current I_max. Thereby, I_max oscillates with a period that is determined by the ratio out of magnetic flux and fluxon [81]:

$$I_\mathrm{max} = 2I_\mathrm{C} \cdot \left| \cos\left(\pi \frac{\Phi}{\Phi_0}\right) \right| \tag{4.2}$$

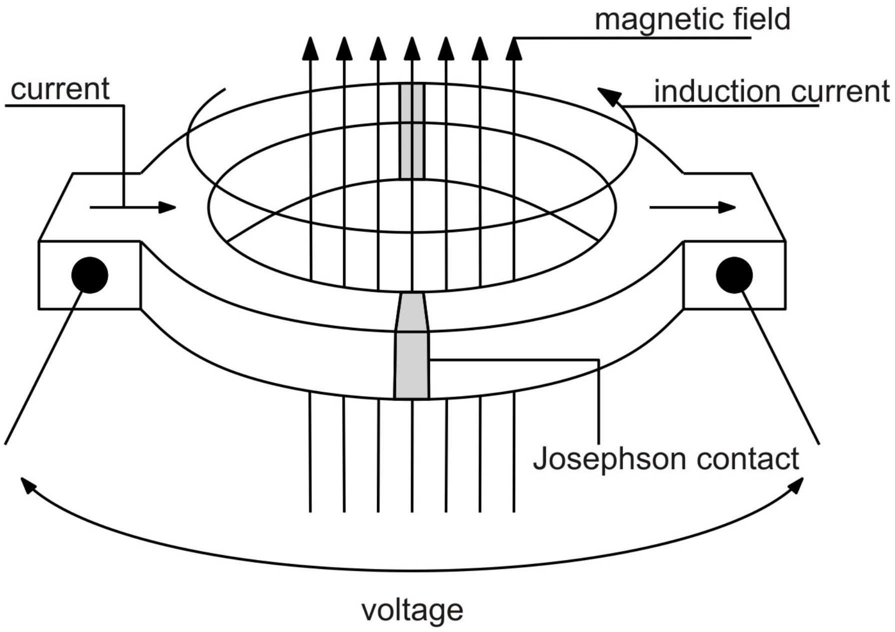

Figure 4.4: Functional principle of a SQUID sensor.

This way, a change of the magnetic flux can be detected by measuring a change of the period of the voltage.

To increase the sensitivity of a SQUID, the lock-in technique was used. Thereby, the sample oscillate with a frequency of 15 Hz, combining the advantages of a SQUID and a VSM (vibrating sample magnetometer) in the sense of sensitivity and measurement speed.

In the frame of this work, a SQUID-VSM magnetometer from *Quantum Design* of the type *SQUID VSM* was used as can be seen in figure 4.5. This specific SQUID model can reach fields up to 7 T and operates in a temperature range from 1.8 to 1000 K.

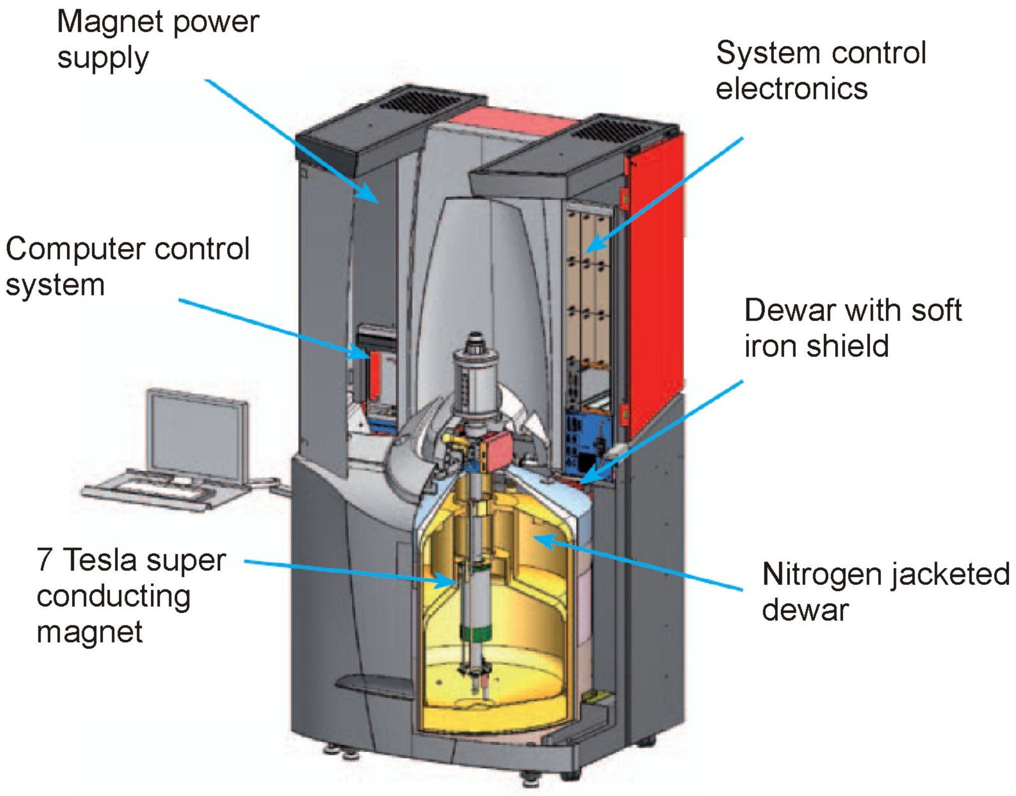

Figure 4.5: Cutaway view of the SQUID VSM setup. Note that the pump console is not shown [82].

4.5 Magneto-optical Kerr effect (MOKE)

To investigate small patterns of magnetic materials, SQUID measurements are not suitable as they only give the magnetic moment of the entire film. Therefore, focused MOKE measurements were performed, allowing the measurement of magnetization looops of the small Co/Pt pattern used in this work.

The magneto-optical Kerr effect is used to probe the magnetic properties of a sample. It is based on the fact that the reflection from the magnetic sample rotates the polarization direction of linear polarized light proportional to the magnetic moment [83]. Additionally, a phase shift between incoming and outgoing light occurs, resulting in an elliptical polarized reflected light. Due to the limited penetration depth of the light in metal films, MOKE is surface sensitive. Please note that with MOKE, only relative changes of the magnetic moment can be measured, but no absolute values. As shown in Fig. 4.6, there are several types of MOKE, depending on the direction of the magnetic field relative to the direction of the light. If the direction of the magnetic field is perpendicular to the sample surface, the MOKE is called polar. In the case of a parallel magnetic field relative to the sample surface, it is called longitudinal MOKE. If the

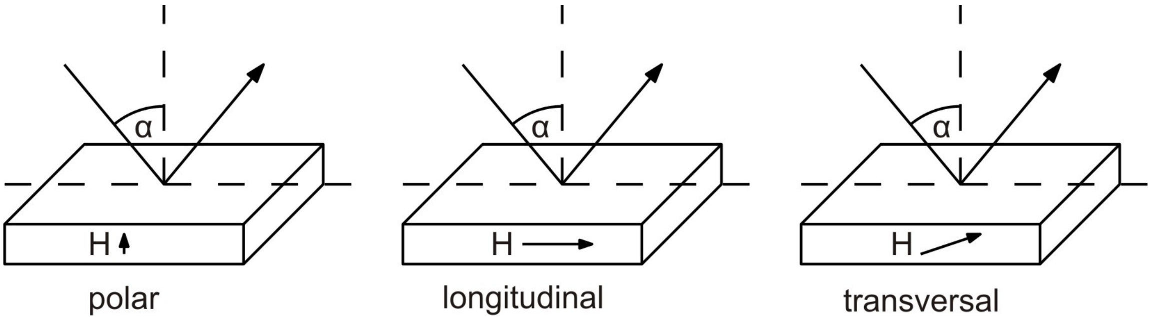

Figure 4.6: Different types of MOKE: polar, longitudinal and transversal.

magnetic field is parallel to the surface but perpendicular to the direction of the incident light, one talks about the transversal MOKE.

In the frame of this work, the polar MOKE setup built by T. Ulbrich was used [84]. A functional principle is presented in Fig. 4.7. A modulated laser beam (wavelength of 670nm) passes through a Wollaston polarizer and gets split by a beam splitter. A Wollaston polarizer consists of two triangular calcite prisms with orthogonal crystal axes that are cemented together. At the internal interface, an unpolarized beam splits into two linearly polarized rays which leave the prism at a divergence angle of 15°-45°. One ray is used as reference beam for the difference detector. The second part gets focused by a lense and reflected by a mirror before it hits sample (spot size about 100 μm). After reflection from the sample, it goes back to the mirror and is

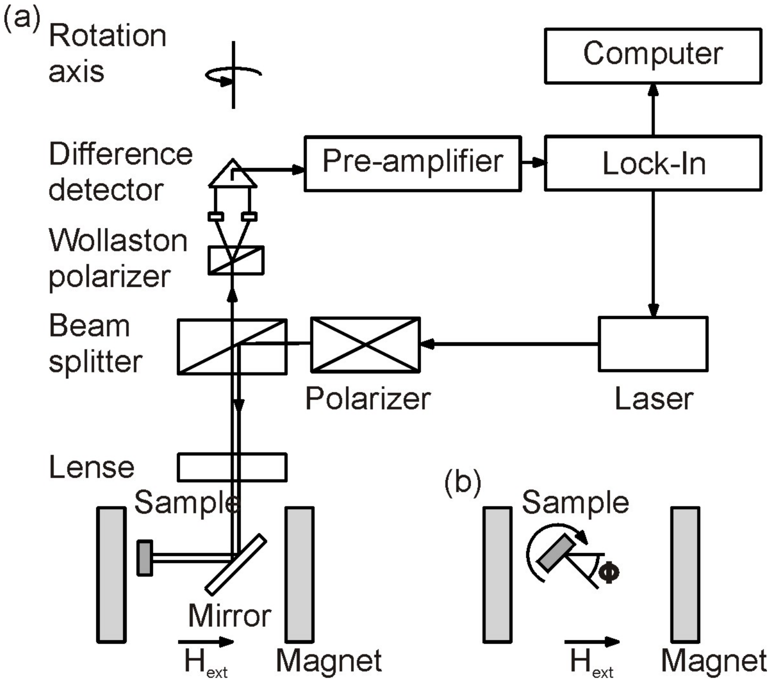

Figure 4.7: Functional principle of the used MOKE setup.

finally used as second beam for the difference detector. The difference between the two beams is the used to extract a normalized magnetization of the sample. Further explanation can be found in [85].

4.6 Magnetic force microscopy (MFM)

In the early 1980s, G. Binnig and H. Rohrer developed the so-called atomic force microscopy (AFM) at the IBM Rüschlikon laboratory in Zurich. Figure 4.8 shows a functional principle of an AFM/MFM. A cantilever is oscillating close to its resonance frequency due to the external excitation from a piezo (piezo not shown here). At the very end of the cantilever, there is a small tip (tip radius about 15 – 50 nm) that scans the sample surface. Due to the Van-der-Waals force between tip and sample, the amplitude and phase of the oscillation of the cantilever changes. These changes can be detected by the photodiode through the laser beam that gets reflected on the backside of the cantilever. If sample and tip have a magnetic moment, there are long-range magnetic forces next to the Van-der-Waals forces, also changing the phase and amplitude of the oscillation. To investigate the local magnetic properties of the sample, at first, the sample is scanned close to the surface, where the strong short-range Van-der-Waals forces have a major influence on the oscillation. After so scanning the surface, the tip is moved away from the sample to about $20 - 100\,\mathrm{nm}$ and the tip is moved along the just recorded height profile. This way, the Van-der-Waals forces are hold constant and now the magnetic force has a major influence. This measurement method is called *lift mode*.

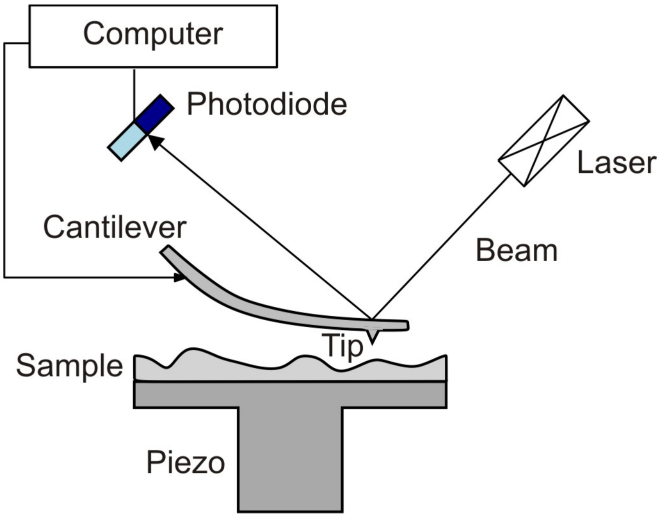

Figure 4.8: Functional principle of an AFM.

4.7 Ion irradiation

Ion irradiation is widely use to modify properties of thin films after their deposition. Ion implantation systems typically consists of three major units:

- an ion source, where ions of the desired element are produced
- an accelerator, where the ions are electrostatically accelerated to a high energy
- a target chamber, where the ions hit the target

Each ion is typically a single atom, and thus the actual amount of material implanted in the target is the integral over time of the ion current. The currents used by the implantation systems are typically small (microamperes), and thus the amount of ions which can be implanted in a reasonable amount of time is small. Therefore, ion implantation finds application in cases where the amount of chemical change required is small [86].

The ion irradiation (in this case Co^+) of the CoCrPt:SiO_2 films was performed in cooperation with the Institute of Ion-Beam Physics and Materials Research, Helmholtz-Zemtrum Dresden-Rossendorf with the low-energy ion implanted *DANFYSIK 1050* at room temperature. The process of the ion irradiation was simulated using the TRIM code of the SRIM package [87]. An irradiation energy of 40 keV was chosen to ensure the maximum of the damage distribution to be situated well within the magnetic layer of the films under investigation. For more details, please see section 5.4. The system used for the ion irradation can be seen in figure 4.9.

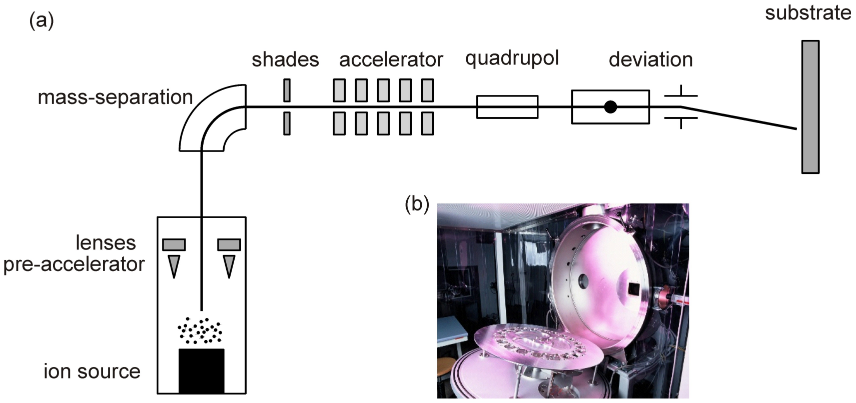

Figure 4.9: (a) Schematics of the used irradiation system, and (b) photo of the target of the irradiation system where the samples were mounted on [88].

Figure 4.9(a) shows a principle scetch of the ion implanter used for the experiments. More details on the working principle of such an ion implanter can be found in basic literature [86, 89]. Moreover, figure 4.9(b) shows a photo of the actual sample holder where the samples were put on for irradiation.

Chapter 5

Results

5.1 Magnetization reversal processes of single nanomagnets and their energy barrier[1]

Micromagnetic simulations were performed to investigate the influence of the geometry and magnetic anisotropy constant on the energy barrier and magnetization reversal mechanism of individual bits important for the bit patterned media concept in magnetic data storage.

Here, a systematic study of the dependence of the energy barrier for magnetization reversal on the geometry of individual bits is presented. Therefore, the shape, either a prism with square base plane or a cylinder, the size, either the edge length or the diameter, respectively, and the thickness of one bit is varied. Additionally, the uniaxial magnetic anisotropy value, K_{U}, is systematically changed. The energy barrier was calculated using the nudged elastic band method (see section 3.5.1 and [77, 91]), implemented in the micromagnetic solver femme (see section 3.3.2 and [92]). Moreover, the field-driven reversal mechanism of the bit, either quasi-coherent or incoherent rotation of magnetization was studied. This is of high importance for the recording process of the bits as the reversal mechanism influences the required write field and thermal stability.

5.1.1 The model

The model consists of one bit with the shape of either a prism with a square base plane with edge length s and thickness t (from now on referred to as "prism") or with a circular base plane with diameter s and thickness t (from now on referred to as "cylinder"). Figure 5.1 shows the models under study with all relevant geometrical properties.

The base plane of the models shall be the xy-plane. The bit possesses a uniaxial anisotropy with the easy axis of magnetization along the z-axis. The magnetic anisotropy value, K_{U}, was varied between $0.5 \times 10^7\,\mathrm{ergs/cm^3}$ and $1 \times 10^8\,\mathrm{ergs/cm^3}$, the thickness, t, between 3 nm and 15 nm, and the size, s, between 5 nm and 20 nm. The saturation magnetization, $\mathrm{M_S}$, was fixed at 14 kG and the exchange constant, A, at $1 \times 10^{-6}\,\mathrm{ergs/cm}$, corresponding to the values of

---

[1] Results have been published in [90]

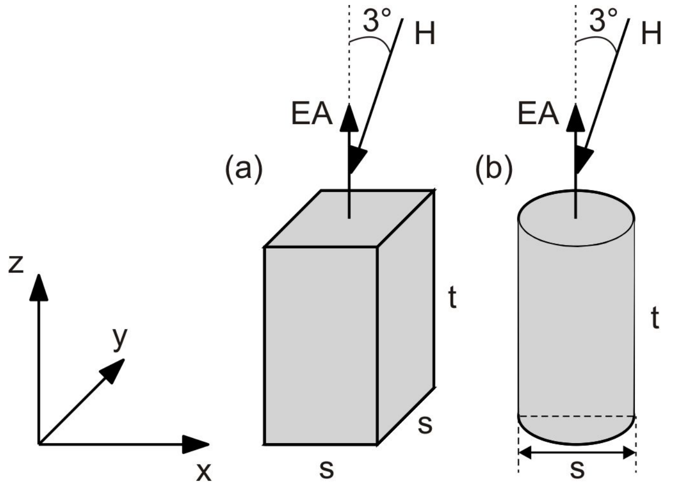

Figure 5.1: Models under study: (a) prism, and (b) cylinder. The orientation of the easy axis, EA, and the external magnetic field is shown.

chemically ordered L1$_0$ FePt alloy [63, 93]. For each set of the parameters s, t, and K_U, the magnetization reversal mode was simulated. The cell size of the finite element mesh for the simulations was set to 1 nm for $K_\mathrm{U} < 6 \times 10^7\,\mathrm{ergs/cm^3}$ and 0.5 nm for $K_\mathrm{U} > 6 \times 10^7\,\mathrm{ergs/cm^3}$. The external magnetic field was applied under an angle of 3° relative to the easy axis to avoid numerical instabilities related to the vanishing torque from the applied magnet field acting on the magnetization. Additionally, the energy barrier ΔE between the two states with $M_\mathrm{z} = +1$ and $M_\mathrm{z} = -1$ (M_z being the to M_S normalized z-component of the magnetization) was calculated at $T = 0\,\mathrm{K}$ using the nudged elastic band method (see section 3.5).

5.1.2 Results and Discussion

5.1.2.1 Energy barrier calculations

In the following discussion, a reversal process in which the magnetic moments of all cells are aligned with a deviation smaller than 2° is defined as “quasi-coherent” rotation. Respectively, the magnetization rotation is “incoherent” if this is not the case. Figure 5.2 shows the energy barrier as function of the magnetic anisotropy, K_U, for both models ($s = 5\,\mathrm{nm}$ and $t = 10\,\mathrm{nm}$).

With increasing magnetic anisotropy value, the energy barrier increases, as the first summand of equation 3.37 increases (Fig. 5.2). In the grey marked area, the reversal of the bit happens through quasi-coherent rotation of the magnetization, as due to the low anisotropy, the energy loss because of all moments being perpendicular to the easy axis during the quasi-coherent rotation is smaller compared to the gain in exchange energy. The data can be fitted using equation 3.39 with the volume as free parameter. In the following, the parameter η is defined as $\eta = \frac{V_\mathrm{act}}{V_\mathrm{bit}}$, which is the ratio between fitted activation volume, V_act, and real volume of the bit, V_bit. Please note that the activation volume is not defined as the first derivative of the energy

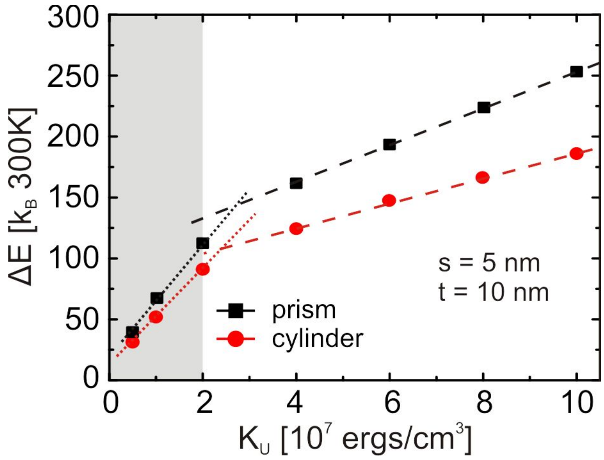

Figure 5.2: Energy barrier ΔE as a function of the magnetic anisotropy constant, K_{U}, for $s = 5\,\mathrm{nm}$ and $t = 10\,\mathrm{nm}$. "prism" stands for the model with a square base plane, "cylinder" for the one with a circular base plane. In the grey marked area, the field-driven magnetization reversal process happens through quasi-coherent rotation (see discussion in the text). Dashed and dotted lines are fit to the data points using equation 3.39.

barrier with respect to the magnetic field but as the volume satisfying equation 3.39 . The fitting of the data points in the grey marked region (Fig. 5.2, dotted line) results in $\eta = 1$. However, the increase of K_{U} results in a transition from quasi-coherent to incoherent reversal behavior and equation 3.39 cannot be used as it is. The increase of ΔE is still found to be linear with K_{U}, however, the slope of the fitted line (Fig. 5.2, dashed line), and thus the ratio η, is reduced to about 0.25, meaning that the activation volume for magnetization reversal is 25% of the real volume of the bit for the specific case of $s = 5\,\mathrm{nm}$ and $t = 10\,\mathrm{nm}$. Additionally, the intersection of both fits gives an approximation for the highest value of the magnetic anisotropy, K_{U}^{max}, for which the reversal is still considered to be quasi-coherent. In the discussed case of the model with $s = 5\,\mathrm{nm}$ and $t = 10\,\mathrm{nm}$, K_{U}^{max} is 2.2×10^7 ergs/cm^3 for a cylinder and 2.4×10^7 ergs/cm^3 for a prism.

Moreover, the energy barrier of the model with a square base plane is higher than the one of the model with a circular base plane. The difference between the ΔE values for the two models is attributed to a different volume for the same s and t values ($\frac{V_{\mathrm{cylinder}}}{V_{\mathrm{prism}}} = \frac{\pi}{4} < 1$), and a different demagnetization factor, influencing the effective anisotropy value. Moreover, the slope in the inhomogeneous region is smaller for the cylinder than for the prism, leading to an increased thermal stability of the magnetic moment in the bit with a square base plane. The following discussion will be limited to the model with square base plane, as no qualitative difference in reversal behavior was found. Figure 5.3 shows a pseudocolor image of $\eta = \frac{V_{\mathrm{act}}}{V_{\mathrm{bit}}}$ and K_{U}^{max} as a function of the size and thickness of the bit.

Both, K_{U}^{max} and η have a similar dependency from the size and thickness. For small sizes and thicknesses ($s < 6\,\mathrm{nm}$, $t < 6\,\mathrm{nm}$), the parameters reach their maximum values of 6×10^7 ergs/cm^3

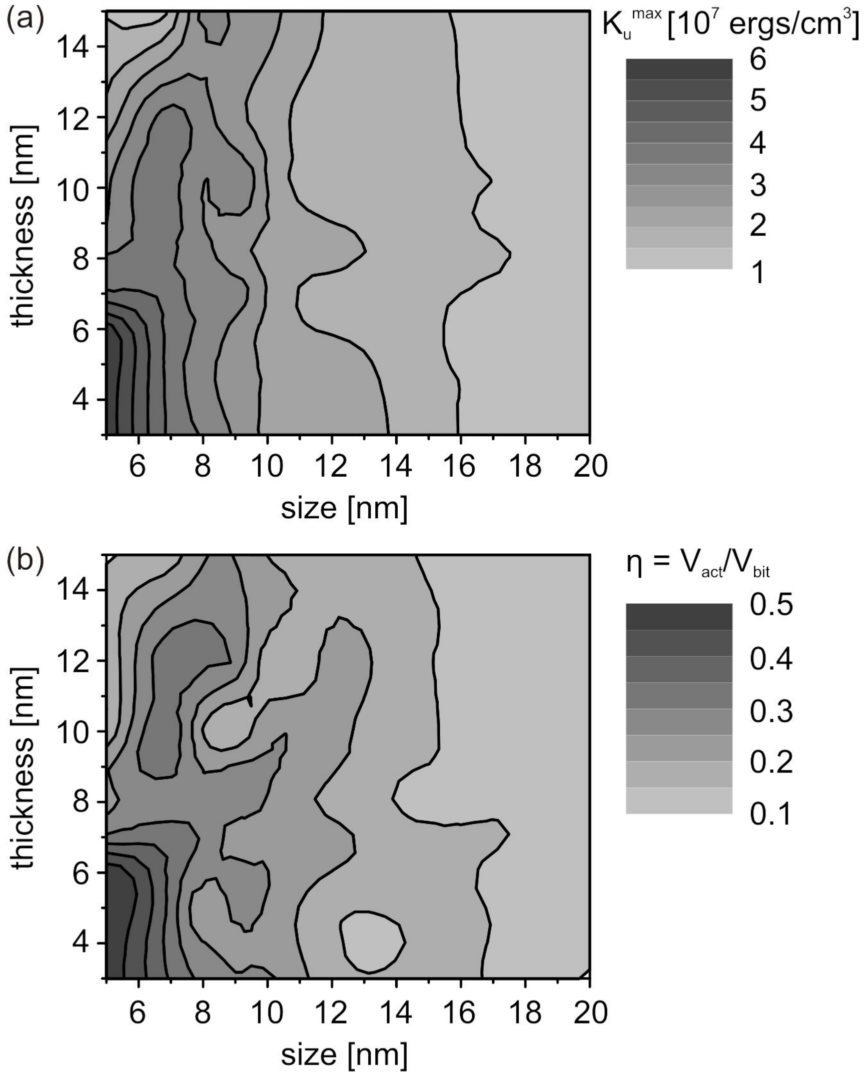

Figure 5.3: (a) Highest value of the magnetic anisotropy, K_{U}^{max}, for which the field-driven reversal happens through quasi-coherent rotation and (b) ratio $\eta = \frac{V_{\mathrm{act}}}{V_{\mathrm{bit}}}$ as a function of the size and the thickness of the bit for the prism. Please note that the images were interpolated from discrete simulation points.

and 0.5, respectively. Please note that occasionally, this magnetic anisotropy value is about the value of L1$_0$ chemically ordered FePt alloy. For increasing dimensions of the bit, K_{U}^{max} and η gradually decrease down to about 1×10^7 ergs/cm^3 and 0.1, respectively, for sizes larger than about 17 nm and all investigated thicknesses. It is important to mention that the ratio between activation volume and bit volume does not exceeded 50% in the case of inhomogeneous magnetization reversal.

Figure 5.4 shows the energy barrier dependency on the size and the thickness of the bit for a fixed $K_{\mathrm{U}} = 2 \times 10^7$ ergs/cm^3. In both cases, the energy barrier increases with increasing geometrical parameter, as the volume increases. Additionally, the increase of the dimensions of

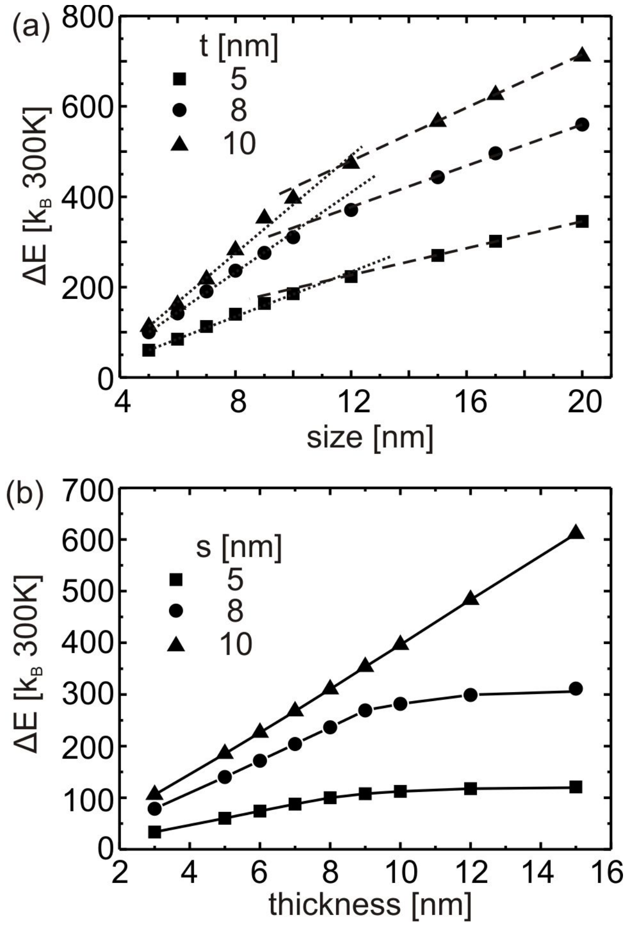

Figure 5.4: Energy barrier ΔE as a function of the (a) size and (b) thickness of the model with square base plane for $K_{\mathrm{U}} = 2 \times 10^7\,\mathrm{ergs/cm^3}$.

the bit changes the demagnetization factor, influencing the effective anisotropy value. In this respect, it was observed that in the case of a fixed t of 10 nm (Fig. 5.4(a)), the quasi-coherent magnetization reversal process if preferable for $s < 10\,\mathrm{nm}$, while it is incoherent for larger sizes. The dependences in both regions show a linear increase of the energy barrier with increasing size with smaller slope in the inhomogeneous region. Furthermore, a saturation effect in the dependence of the energy barrier from the thickness was observed for bit sizes of 5 nm and 8 nm (Fig. 5.4(b)). This saturation effect can be explained in terms of a change of the reversal mechanism from a quasi-coherent rotation process to an incoherent one by accumulation of a multi-domain vortex state [94]. However, please note that the multi-domain vortex states are no equilibrium states of the system. Indeed, the Bloch wall width is approximately 9 nm for the given parameters. For a bit size of 10 nm (and larger), a saturation effect was not observed in the range of the investigated bit thickness. Also the fact that such a saturation effect is not observed for $\Delta E(s)$ (Fig. 5.4(a)) is related to the relatively small range of investigated bit sizes. With further increasing the size of the bit, a saturation effect is expected to occur due to a change of the magnetization reversal mechanism to domain wall nucleation and propagation.

5.1.2.2 Reversal mechanisms

From both an application and fundamental point of view, the transition from a quasi-coherent reversal regime to a regime of incoherent magnetization reversal with increasing bit size and thickness is of interest. For an ellipsoid, the transition happens at a certain critical diameter dcrit proportional to the exchange length, where both, the nucleation field for quasi-coherent rotation and the one for incoherent rotation (i.e. curling) are equal [95]. Figure 5.5 shows pseudo color images depicting the reversal mode of the models under study. The upper row shows the results for the model with square base plane (prism), the lower row for the model with a circular base plane (cylinder). The white color represents the regime of incoherent magnetization reversal, where as the grey color corresponds to the geometrical parameters where the model reveals quasi-coherent rotation of magnetization.

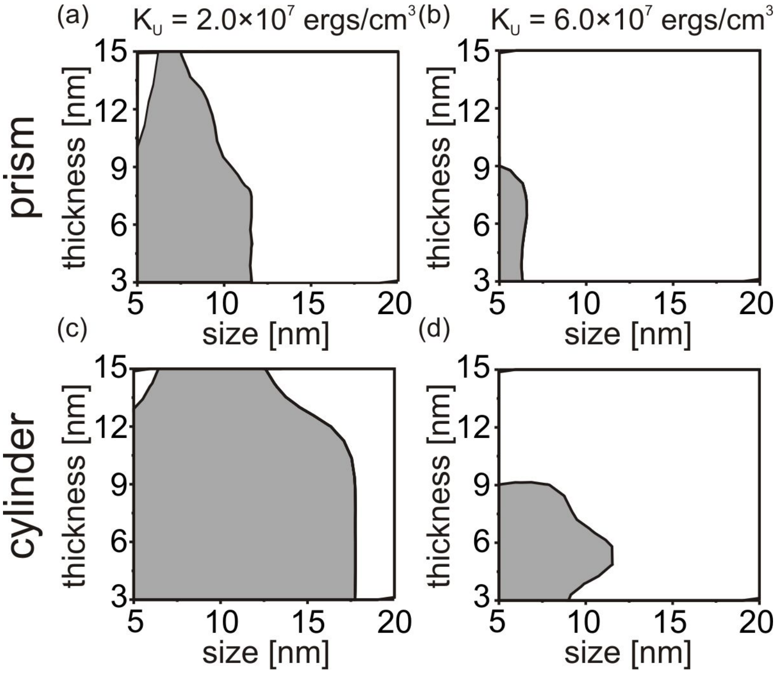

Figure 5.5: Pseudo color image of the reversal mechanism of a single bit with square (upper row) or circular (lower row) base plane as a function of the size and the thickness of the bit. Additionally, the magnetic anisotropy value, K_U, was varied. The grey areas represent quasi-coherent magnetization reversal and the white areas incoherent magnetization reversal.

By comparing Fig. 5.5(a) and (c), it turns out that the cylinder reveals quasi-coherent magnetization reversal for bigger sizes than the prism. This is related to the different demagnetization factor and volume of the bit with the same geometrical properties s and t. The analysis suggests that for small lateral sizes and high thicknesses, the reversal becomes incoherent (incoherent region in the upper left corner in Fig. 5.5(a) and (c)). With increasing magnetic anisotropy constant, the reversal process becomes preferably incoherent (compare subfigures (a) and (b) in Fig. 5.5). To illustrate the temporal evolution of the reversal process of the bit,a series of magnetic states for the prism model with $t = s = 10\,\mathrm{nm}$ corresponding to incoherent magnetization reversal (Fig. 5.6(a)-(p)) for $K_\mathrm{U} = 6 \times 10^7\,\mathrm{ergs/cm^3}$ and quasi-coherent magnetization rotation (Fig. 5.6(q)-(u)) for $K_\mathrm{U} = 2 \times 10^7\,\mathrm{ergs/cm^3}$ is presented.

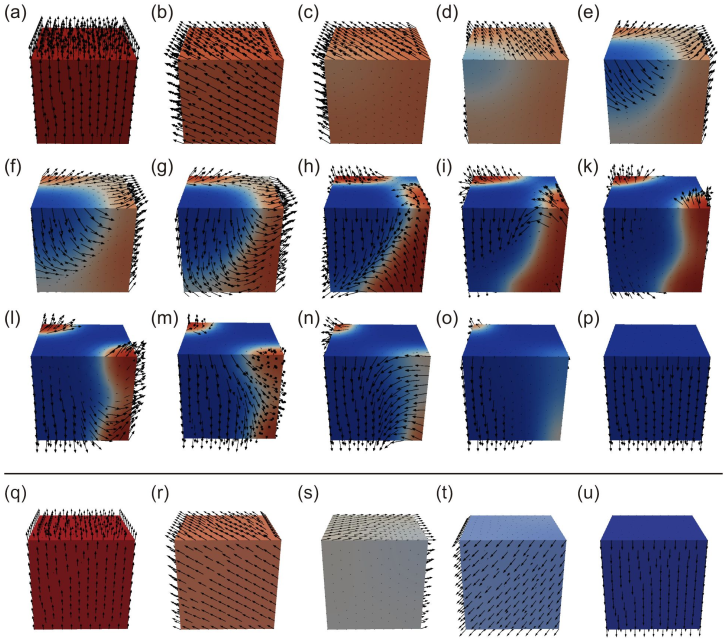

Figure 5.6: Temporal evolution of the magnetization reversal of an individual bit with square base plane with a thickness $t = 10\,\mathrm{nm}$, and a size $s = 10\,\mathrm{nm}$. (a)-(p) incoherent reversal process ($K_\mathrm{U} = 6 \times 10^7\,\mathrm{ergs/cm^3}$). (q)-(u) quasi-coherent reversal process ($K_\mathrm{U} = 2 \times 10^7\,\mathrm{ergs/cm^3}$).

Figure 5.6(a)-(p) shows that the reversal of the hard bit with $K_\mathrm{U} = 6 \times 10^7\,\mathrm{ergs/cm^3}$ happens by domain wall nucleation at a corner (Fig. 5.6(d)) and consecutive domain wall propagation through the entire bit. This incoherent reversal process is preferable for high K_U values as the total energy gets minimized by avoiding the collective tilt of the magnetization to high angles compared to the easy axis. However, please note that the domain walls built during the reversal process are not stable. For a softer bit (Fig. 5.6(q)-(u)), the reversal happens through quasi-coherent rotation, all spins are collinear within 2° for the complete reversal process.

In addition, it is important to emphasize the small area of incoherent rotation for a thickness of 15 nm and a size of 5 nm (very left upper corner of Fig. 5.5(b)). Figure 5.7 summarizes the temporal evolution of the magnetic states of a prism with $t = 15\,\mathrm{nm}$, $s = 5\,\mathrm{nm}$, and $K_\mathrm{U} = 2 \times 10^7\,\mathrm{ergs/cm^3}$. For those elongated bits, the magnetization reversal process happens through curling with a stabilization of a $\frac{\pi}{2}$ magnetic domain state [94].

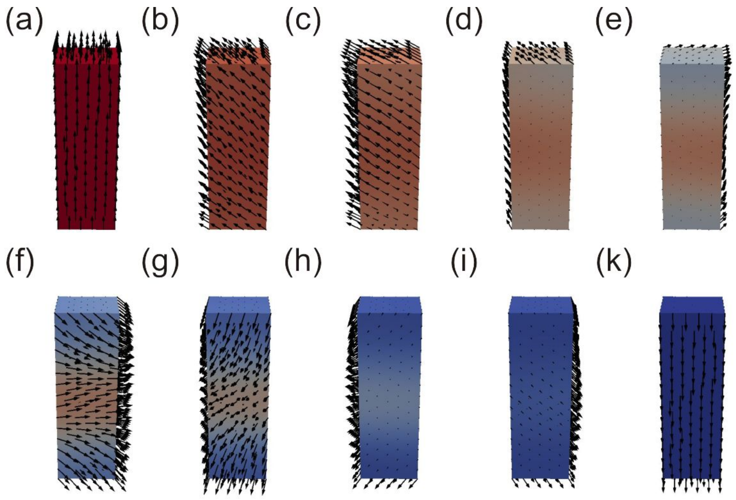

Figure 5.7: Reversal of an individual bit with a thickness of 15 nm, a size of 5 nm, and a magnetic anisotropy constant of 2×10^7 ergs/cm^3.

5.2 Micromagnetic Simulations on the Magnetization Reversal of single-phase Bit Patterned Media[2]

The bit array under study consists of 8×8 bits with each bit having a volume of $10 \times 10 \times 5\,\text{nm}^3$ (see Figure 5.8(a)).

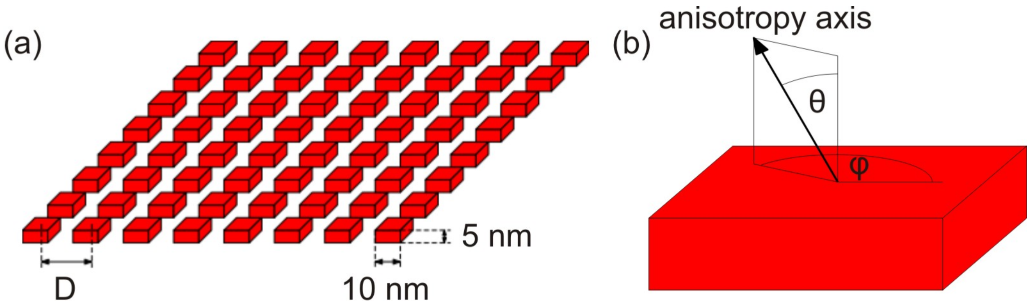

Figure 5.8: (a) Sketch of the model under study, (b) orientation of the anisotropy axis (Θ, φ) of an individual bit.

The center-to-center distance, D, is varied between 11 and 110 nm, which covers areal densities of up to 4.8 Tbit/inch^2. To achieve such high areal densities and satisfy the criteria of thermal stability, hard magnetic materials, i.e. FePt alloys, have to be used owing to their high magnetic anisotropy constant. Therefore, in the following, magnetic materials with parameters close to the one of FePt alloys, i.e., a saturation magnetization, M_S, of 14 kG, an exchange parameter, A, of 1×10^{-6} ergs/cm, and magnetic anisotropy constants K_U of up to 2×10^7 erg/cm^3, will be considered. To account for the aforementioned distribution of media properties, the magnetic

---

[2] Results have been published in [96–98]

anisotropy constant was varied with a Gaussian distribution with a mean value K_U between 0.6×10^7 and $2 \times 10^7\,\mathrm{ergs/cm^3}$ and a standard deviation σ_{K_U} (normalized on K_U) between 0 and 0.2. However, note that for each bit, the magnetic anisotropy value is fixed and the distribution is realized by assigning a different K_U value to every bit randomly. Assuming these magnetic parameters, the exchange length and the Bloch domain wall width are both larger than 2 nm. Thus, a mesh size of 2 nm was chosen for all simulations. The external magnetic field was applied under an angle of 2° to avoid numerical instabilities. However, note that there is no dispersion in the easy axis considered. To exclude the influence of the fact that the array has a limited size of 8 by 8 bits only, the simulations were cross-checked with simulations for an array of 20 by 20 bits, but no substantial differences were found ($< 7\%$).

Additionally, an angular variation of the magnetic anisotropy axis orientation was taken into account realized by assigning the angles Θ and φ to each individual bit, with Θ being fixed for the entire bit array and φ being randomly chosen between 0 and 2π for every single bit (Fig. 5.8(b)). Thus, the ensemble of magnetic anisotropy axes in the bit array is located on the surface of a cone with an opening angle Θ.

Each simulation with a given set of parameters (D, M_S, K_U, σ_{K_U}, Θ) was performed 30 times, where as for each run, a new set of 8×8 magnetic anisotropy values was chosen randomly and assigned to the individual bits. The magnetic parameters of interest (coercive field H_C and corresponding switching field distribution) were determined using statistical averaging over all 30 runs of one set, resulting in a distribution of the magnetic parameters (shown as error bars in the figures). From an application point of view, the i.e. highest value of SFD/H_A is of interest as this shows the worst case which has to be handled in a BPM system, for example the hardest bit at the corner of the array and the softest at the center.

5.2.1 Perpendicular Magnetic Anisotropy Axis: $\Theta = 0°$

To investigate the magnetization reversal behavior in the array of magnetic nanostructures, the series of simulations was performed by varying systematically the value of the mean magnetic anisotropy constant, K_U, the standard deviation, σ_{K_U}, and the center-to-center distance, D, keeping the size of the nanostructures ($10 \times 10 \times 5\,\mathrm{nm^3}$) constant. The magnetic anisotropy axis was perpendicular to the plane, $\Theta = 0°$.

An example of a simulated hysteresis half-loop of an array with $D = 20\,\mathrm{nm}$ using $K_\mathrm{U} = 1 \times 10^7\,\mathrm{ergs/cm^3}$, $M_\mathrm{S} = 14\,\mathrm{kG}$, and σ_{K_U} of 0.05 is shown in Fig. 5.9(a) indicating also the way how H_C and the SFD are determined. It is worth noticing that the SFD is defined as the difference between the field of the last and first switching event. Additionally, the evolution of the switching events in the array revealing discrete steps due to individual switching events in the hysteresis loop with increasing reverse field is presented in Fig. 5.9(b)-(k).

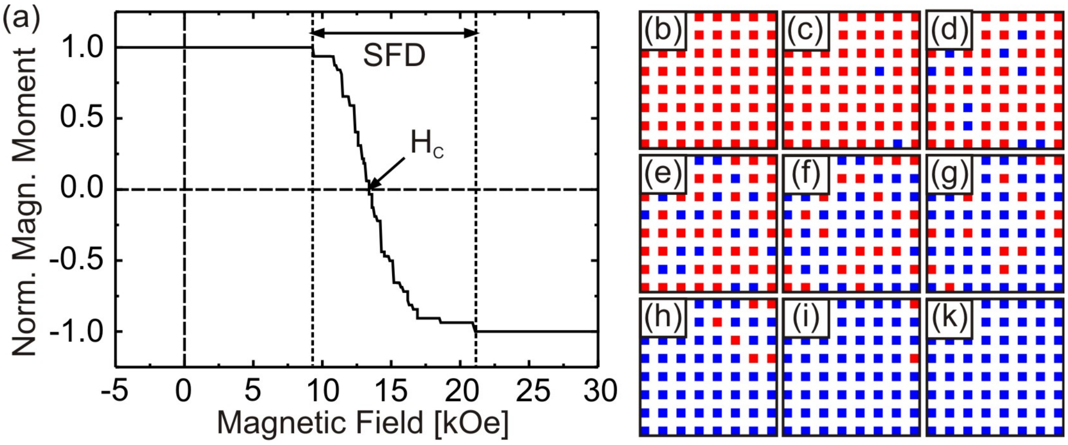

Figure 5.9: (a) Hysteresis half-loop with marked switching field distribution (SFD) and coercive field, H_C. Magnetic states of the system at (b) 0 Oe, (c) 9.4 kOe, (d) 11 kOe, (e) 12.6 kOe, (f) 14 kOe, (g) 14.9 kOe, (h) 16.2 kOe, (i) 18.6 kOe, and (k) 21.2 kOe are shown. Parameters of this simulation: $D = 20\,\mathrm{nm}$, $K_\mathrm{U} = 1 \times 10^7\,\mathrm{ergs/cm^3}$, $\sigma_{K_\mathrm{U}} = 0.05$.

5.2.1.1 Influence of the magnetic anisotropy value

The dependence of the coercive field on the mean magnetic anisotropy value for a given distribution σ_{K_U} (0.05 and 0.1) and a fixed center-to-center distance of 20 nm is presented in Fig. 5.10(a), revealing a linear increase of H_C with K_U following equation 3.31. The α parameter is related to the type of magnetization reversal process (nucleation- or pinning-dominated). Thereby, α describes the presence of defects of an inhomogeneous magnetic region on the surface and the influence of misalignment of the easy axis. In our case, α was determined from simulations by analyzing the H_C over H_A dependence to be approximately 0.9, which is typical for magnets with a nucleation-dominated reversal mechanism [99]. The difference compared to the classical model considered by Brown, where α is assumed to be 1, results from the effective angle between the total magnetic field (applied field plus magnetostatic interaction field) and the magneto-crystalline anisotropy axis. According to the STONER-WOHLFARTH theory, the switching field reduces by a factor of 0.9 to 0.86 if the field angle changes from 1° to 2°. In this respect, it is important to note that although it is an initially uniaxial system, the relaxation of the magnetization results in a tilt at the edges of the single bits. This relaxation arises from the local demagnetizing fields and contributes to the effective demagnetization factor [100].

Fig. 5.11 shows the top view of the three components of the magnetization for the center bit of a 3×3 array ($K_\mathrm{U} = 1 \times 10^7\,\mathrm{ergs/cm^3}$) in a remanent state after initial saturation. In the color scheme the red color corresponds to a maximum, the blue to a minimum, and the green to an intermediate value of the component along the x, y, or z-direction. However, note that the absolute difference between minimum and maximum value of M_S is only 3.26%, which defines the tilt of the magnetization from the easy axis [100]. The presence of this tilt was further evidenced by an increase of the uniaxial magnetic anisotropy constant, resulting in a more

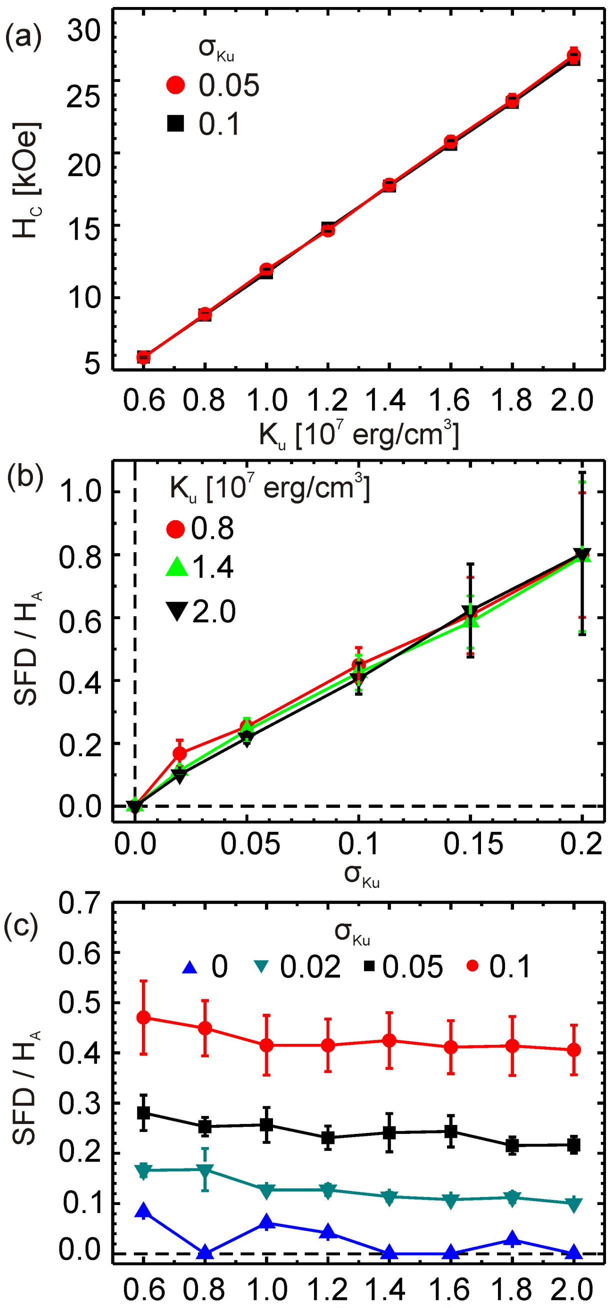

Figure 5.10: (a) Dependency of the coercive field on the magnetic anisotropy constant for different σ_{K_U} values. (b) Variation of SFD/H_A as function of the standard deviation σ_{K_U} for different values of K_U. (c) Variation of SFD/H_A as function of the magnetic anisotropy constant using various standard deviations, σ_{K_U}. Note that the lines are guides to the eye. The distance between two bits was set to 20 nm (1.5 TBit/inch^2).

parallel alignment of the moments at the edges of the nanostructures, and thus a reduction of the tilt of the magnetization. Also, the tilt increases with decreasing distance between two individual bits, resulting from the increased stray field.

Moreover, a variation of σ_{K_U} does not influence the coercive field, as the coercivity is defined by the mean value of the magnetic anisotropy constant and not by its distribution. Contrary to that, the SFD is expected to depend substantially on σ_{K_U} as with increasing σ_{K_U} the range

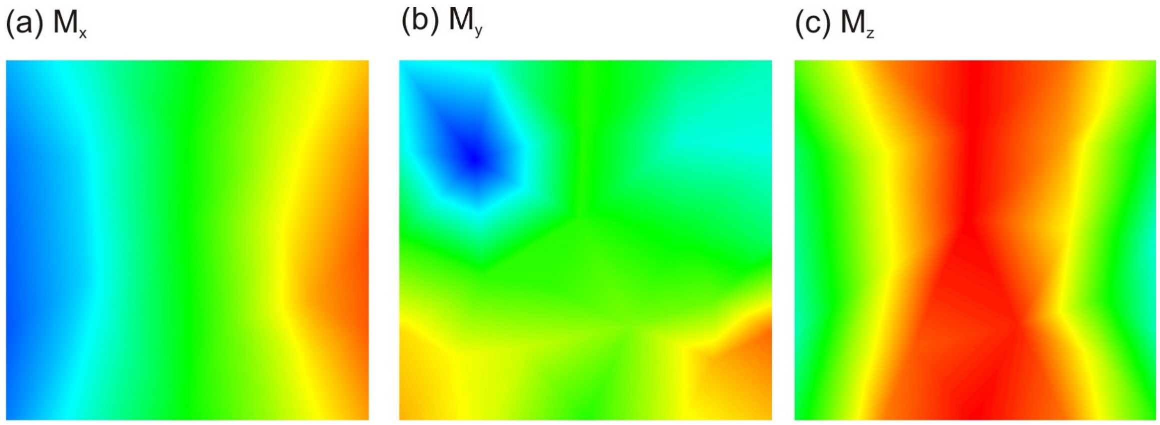

Figure 5.11: (a) M_x, (b) M_y, and (c) M_z component of the magnetization direction of the center bit of an 3×3 bit array at remanence after relaxation from an initially saturated state. The magnetic anisotropy constant, K_U, was set to 1×10^7 ergs/cm^3. In the color scheme the red color corresponds to a maximum, the blue to a minimum, and the green to an intermediate value of the component along the x, y, or z-direction. Note that the absolute difference between minimum and maximum value of M_S is 3.26%, which defines the tilt of the bit.

of the switching fields of the individual bits becomes larger, resulting in a broadening of the SFD (5.10(b)). It is important to note, that even with an assumed σ_{K_U} of zero, a non-vanishing value of the SFD was found. The reason for this is the magnetostatic coupling in the array of bits, leading to a stabilization/destabilization of the magnetic moments of the bits through magnetic dipole-dipole interaction. With increasing σ_{K_U}, the normalized SFD/H_A increases linearly as the probability to find bits with very high and very low magnetic anisotropy constants becomes larger. Note that a normalization of the SFD on H_A instead of H_C was chosen to eliminate the influence of the H_C variation and thus being able to concentrate on the changes in the SFD. Additionally, the dependency of the switching field distribution on the magnetic anisotropy constant was extracted (Fig. 5.10(c)). Analysis has shown that the SFD gradually increases with K_U. However, the SFD normalized on H_A decreases with increasing magnetic anisotropy constant for all simulated standard deviations σ_{K_U}, attributed to the fact that a harder bit does not get influenced by the dipolar interaction as much as a softer one. Thus, for achieving a SFD/H_A value smaller than for example 10% for an areal density of 1 Tbit/inch^2, the BPM must consist of bits harder than 1.6×10^7 ergs/cm^3 with a σ_{K_U} equal to 0.02 ($M_S = 14\,\mathrm{kG}, A = 1 \times 10^{-6}$ ergs/cm). However, note that the calculated SFD/H_A value corresponds to the full width of the distribution taking into account the softest and hardest bits, whereas in experimental literature, the given values are usually taken at full width at half maximum (FWHM) of the distribution.

5.2.1.2 Influence of the center-to-center distance

Dipole-dipole interaction in the array of bits was studied by varying the center-to-center distance between the bits. In Fig. 5.12, the changes of HC with the distance are presented for $\sigma_{K_\text{U}} = 0.05$. With decreasing center-to-center distance, HC at first decreases at the limit of ultra-high bit densities (grey marked area in Fig. 5.12), independent on the magnetic anisotropy constant, and remains nearly constant for larger distances.

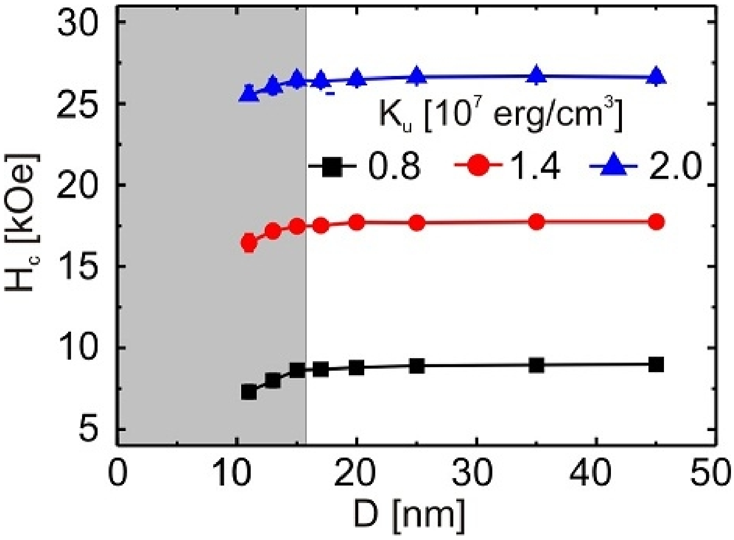

Figure 5.12: Dependency of H_C on the center-to-center distance for varying magnetic anisotropy values. The standard deviation, σ_{K_U}, was set to 0.05. The grey area defines the region with areal densities beyond 2.5 Tbit/inch^2.

This can be explained in terms of the dipolar field influence from one bit to the others. With increasing distance, the magnetostatic interaction becomes weaker and thus, a higher field is required for switching half of the squares in the array. The $H_\text{C}(D)$ curve can therefore be fitted with a function of the form:

$$H_\text{C} = (H_\text{A} - H_\text{Demag}) - \frac{m}{4\pi D^3} \tag{5.1}$$

where $m = M_\text{S} \times V_\text{square}$ is the magnetic moment of an individual bit, which is in agreement with recent results presented by BASU et al. [101]. The normalized SFD/H_A shows an opposite behavior on the separation distance: at large distances the SFD/H_A values are almost constant within the margin of error and then below $D = 20$nm the values increase substantially with smaller separation distance (Fig. 5.13(a)). A strong dependence on the anisotropy constant is found at ultra-high densities ($D < 25$ nm), where the SFD/H_A drops substantially with the increase of K_U. For larger distances the ratio SFD/H_A stays nearly independent on the magnetic anisotropy constant. This finding can be explained in terms of dipolar fields: As the energy of a system is minimized for antiparallel aligned dipoles, such a dipole-dipole interaction results in an early switching of some bits and a late switching of some others, as those are then stabilized by the surrounding, already switched, bits. Additionally, the dependence of the SFD/H_A on the center-to-center distance for different values of the saturation magnetization, M_S, was analyzed (Fig. 5.13(b)). It was found that with decreasing M_S, SFD/H_A drops due to less magnetostatic interaction between the bits, opening a way to narrow the switching field distribution, which can be realized by using "antiferromagnetically coupled media"[16].

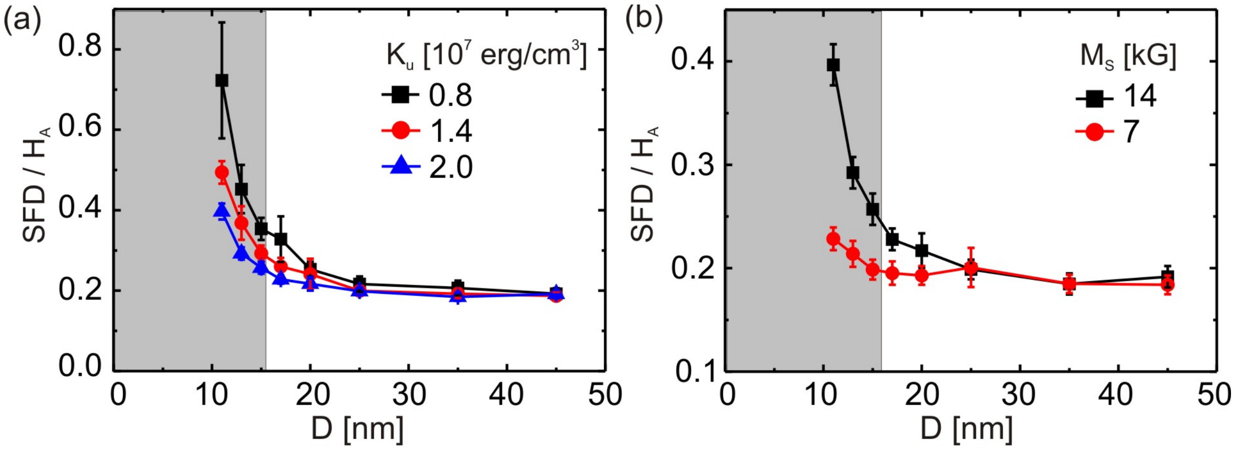

Figure 5.13: Dependency of the SFD/H_A on the center-to-center distance between two bits for (a) different values of the magnetic anisotropy constant ($M_\mathrm{S} = 14\,\mathrm{kG}$) and (b) different values of M_S ($K_\mathrm{U} = 2 \times 10^7\,\mathrm{ergs/cm^3}$). The standard deviation, σ_{K_U}, was set to 0.05. The grey area defines the region with areal densities beyond 2.5 Tbit/inch^2.

5.2.1.3 Influence of the size and thickness of the individual bits

The influence of the size and thickness of the bits was investigated in an array of 8×8 bits with a center-to-center distance of $D = 20\,\mathrm{nm}$. Moreover, the magnetic anisotropy value was chosen to be either $0.8 \times 10^7\,\mathrm{ergs/cm^3}$ or $1.4 \times 10^7\,\mathrm{ergs/cm^3}$, and the standard deviation, σ_{K_U}, to be 0 or 0.05. Figure 5.14 shows the influence of the size of the bit on the coercive field and switching field distribution for a fixed thickness of 5 nm.

With increasing size of the bits, the coercive field drops, whereas the switching field distribution increases, independent of the magnetic anisotropy value and the standard deviation. The decrease of the coercivity is reason by multiple facts:

- With increasing bit size, the effective distance between the bits decreases, leading to an increase of the magnetostatic influence of the bits to each other. Moreover, also the absolute magnetic moment, $M_\mathrm{S} \times V$, of each bit increases, significantly increasing the magnetostatic field.

- Also for a single bit, the coercivity decreases with increasing bit size, suggestion a change of the magnetization reversal mode of the bit from quasi-coherent rotation of magnetization to

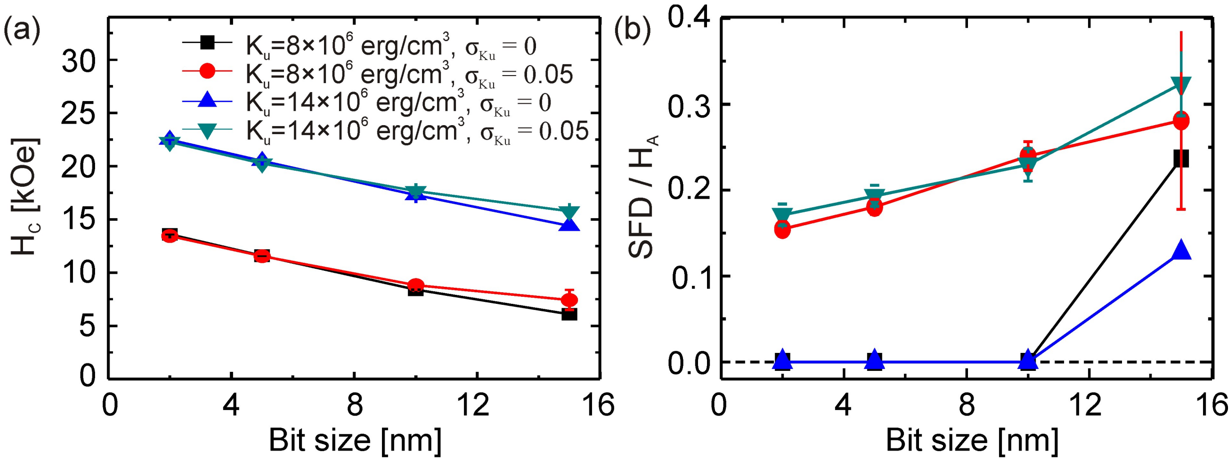

Figure 5.14: Dependency of the (a) coercive field, H_{C}, and (b) normalized switching field distribution, SFD/H_{A}, on the size of the individual bits for different values of the magnetic anisotropy constant, K_{U} and the standard deviation, $\sigma_{K_{\mathrm{U}}}$. The legend in (a) is also valid for subfigure (b).

incoherent magnetization reversal.

The increase of the switching field distribution is solely based on the increase of the dipolar interaction between the bits, similar to decreasing the distance between the bits, as discussed above.

Figure 5.15 shows the influence of the thickness of the bits on the coercive field and switching field distribution of the bit array for a fixed bit size of 10 nm. Whereas the switching field

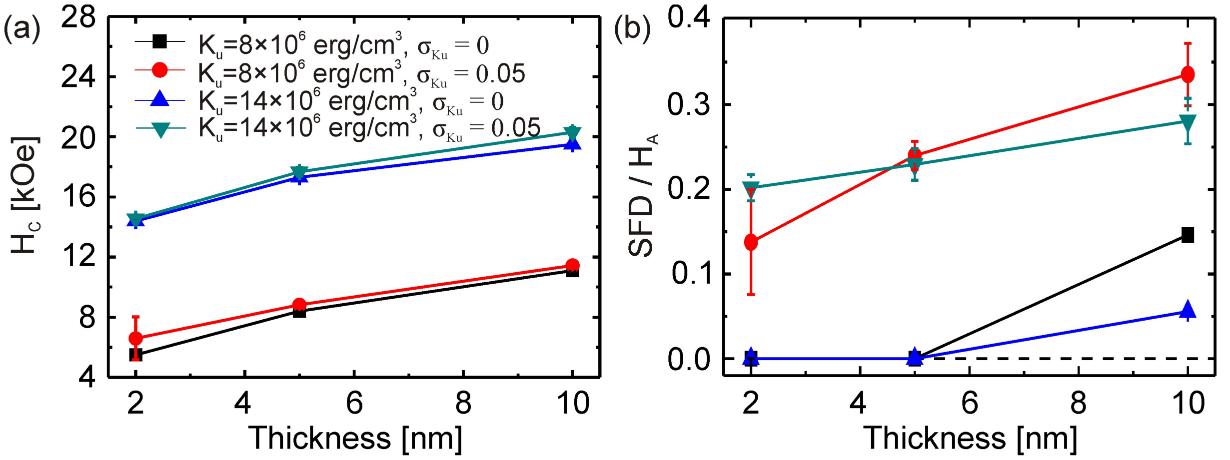

Figure 5.15: Dependency of the (a) coercive field, H_{C}, and (b) normalized switching field distribution, SFD/H_{A}, on the thickness of the individual bits for different values of the magnetic anisotropy constant, K_{U} and the standard deviation, $\sigma_{K_{\mathrm{U}}}$. The legend in (a) is also valid for subfigure (b).

distribution increases with increasing thickness of the bits, which can be explained by the magnetostatic influence of the bits, similar to the discussion about the bit size above, the coercive field also increases with increasing bit thickness. The increase of the coercivity with increasing bit thickness occurs not only in an array of bits but also for a single bit, leading to the suggestion that a change of the demagnetization factor and thus of the magnetization reversal mechanism is the reason for the increase of H_C.

5.2.1.4 Influence of the magnetic field angle

To obtain more information on the magnetization reversal behavior in the system, an analysis of the angular dependence of the switching field, H_S, was performed. This was done by computing the hysteresis loops of the system exposed to an external magnetic field applied under an angle relative to the easy axis for a fixed K_U value of 1×10^7 ergs/cm^3. Note that the switching field was not extracted at remanence but in-field and only the z-component of the magnetization was analyzed, however, it was checked that the individual bits do not switch back in their original state once the field is turned off. The angular dependence of the switching field was extracted and is presented in Fig. 5.16(a), revealing a clear minimum at 45° and then an increase towards the initial value. Both features are characteristic for a reversal process which is dominated by nucleation as described in the STONER-WOHLFARTH model for the reversal of single-domain particles with uniaxial magnetic anisotropy.

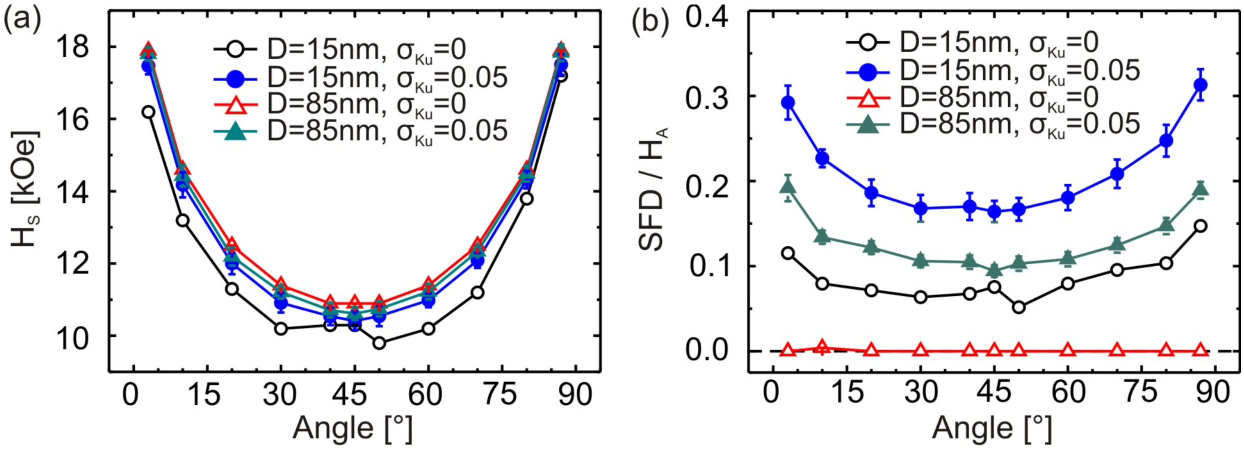

Figure 5.16: (a) Angular dependence of the (a) switching field and (b) switching field distribution SFD/H_A for different distances between two bits and different σ_{K_U}, ($K_\mathrm{U} = 1 \times 10^7$ ergs/cm^3).

The analysis shows that the magnetization reversal is rather independent within the margin of error on the center-to-center distance between two bits and on the intrinsic distribution of the magnetic anisotropy constant, following the discussion above. Moreover, the angular dependence of the normalized switching field distribution was investigated for different distances and different σ_{K_U} values (5.16(b)). For large center-to-center distances and vanishing σ_{K_U}, there is no switching field distribution, as there is neither considerable magnetostatic interaction between the individual bits nor an intrinsic distribution of the magnetic anisotropy constant. However, with both, increasing σ_{K_U} and decreasing center-to-center distance, the normalized switching field distribution decreases and shows a minimum at 45°. The reduction of SFD/H_A towards 45° is related to the decreased switching fields which favors an earlier switching. According to the STONER-WOHLFARTH theory both the switching field of the first bit and the switching field of the last bit is reduced by the same factor which also reduces the difference between these fields. In addition, magnetostatic interactions not only change the absolute value of the total magnetic field acting on a bit but also vary the angle of the total magnetic field. Near 45°, any variation of the angle only leads to a small change of the switching field, according to the STONER-WOHLFARTH theory. Thus, if the external field is applied a 45°, magnetostatic interaction contributes less to the switching field distribution. This finding of a narrowing of SFD/H_A of the array might be of particular interest for the "tilted media"concept [46, 102, 103], where reading/writing is performed in the inclined geometry of the applied magnetic field with respect to the magnetization orientation.

5.2.2 Tilted Magnetic Anisotropy Axis: $\Theta > 0°$

Contrary to the micromagnetic simulations with $\Theta = 0°$, for a tilted magnetic anisotropy axis, hysteresis loops are not as meaningful from an application point of view. Instead, remanent loops, as discussed in section 3.4.1, reveal important magnetic properties of the investigated magnets. There, for each run as described at the beginning of this section, the magnetization was at first saturated in positive z-direction and then a reverse field H_R in opposite z-direction was applied. Afterwards, the field was turned off and the system relaxed resulting in a remanent magnetization M_R. In this way, the remanent loop $M_\mathrm{R}(H_\mathrm{R})$ was build. The magnetic properties of interest (switching field H_S and SFD) were then determined out of these remanent loops the same way as described before. Moreover, in the following, the distance between the bits, D, was fixed at 20 nm.

5.2.2.1 Influence of the tilt angle Θ

For this study, the external magnetic field was applied under an angle of 0° with respect to the surface normal. From the simulation results for the bit array, H_S and SFD were extracted as a function of the fixed tilt angle θ for different magnetic anisotropy values. Note that as the angle φ was randomly chosen between 0 and 2π for every single bit. As summarized in Fig. 5.17(a), with increasing tilt angle up to $25° - 35°$, a gradual decrease of H_S normalized to the anisotropy field (H_A) is obtained depending on the chosen K_U value. A further increasing tilt angle leads to an increase of $H_\mathrm{S}/H_\mathrm{A}$. For comparison the ideal Stoner-Wohlfarth curve for a coherent reversal process was also included in Fig. 5.17(a). The deviation from this ideal behavior is more pronounced for small K_U values and can be attributed to the presence of an inhomogeneous magnetization distribution in a bit cell resulting in an incoherent magnetization reversal process, which is more prominent for softer bits [94, 104]. To support this assumption, additional simulations were performed on arrays of ellipsoids ($a = b = 10\,\mathrm{nm}, c = 5\,\mathrm{nm}$) with homogeneous magnetization revealing an almost ideal Stoner-Wohlfarth reversal behavior (not shown). The influence of the tilt angle on H_S was found to be independent of the intrinsic magnetic anisotropy distribution (Fig. 5.17(a)), as the switching field is defined by the mean value of the magnetic anisotropy distribution but not by its standard deviation. The SFD normalized to the anisotropy field H_A as a function of tilt angle Θ is presented in Fig. 5.17(b). The lowest SFD is found for Θ equal 45° showing only a weak dependence on the magnetic anisotropy value. Moreover, the SFD becomes much broader by using a larger variation of the magnetic anisotropy value ($\sigma_{K_\mathrm{U}} = 0.05$), as was expected. Whereas the normalization of the SFD to H_A helps to separate different effects in a theoretical analysis, for the design of a magnetic recording system, the value of SFD$/H_\mathrm{S}$ might be more important for experimentalists. Therefore SFD$/H_\mathrm{S}$ as function of of tilt angle Θ is also shown in Fig. 5.17(c). It turns out that the lowest values of SFD$/H_\mathrm{S}$ are achieved for tilt angles of about $60° - 75°$, depending on K_U. By neglecting a distribution of the magnetic anisotropy value ($\sigma_{K_\mathrm{U}} = 0$), the SFD can be further reduced drastically, but might be rather challenging to achieve experimentally. Another issue from the application point of view is the strongly reduced read back signal given by the z-component of the magnetization with increasing tilt angle.

5.2.2.2 Influence of the applied field angle

In this section we explore the influence of the applied field angle on the averaged switching field and its distribution. A series of simulations was performed by varying the angle of the applied magnetic field with respect to the surface normal. Still, the studied bit array has an angular variation of the magnetic anisotropy axis orientation.

Figure 5.18 shows simulation results revealing a Stoner-Wohlfarth-like behavior for the switching field with a minimum at 45° for bit arrays exhibiting a small tilt ($\Theta < 10^\mathrm{o}$) of the magnetic anisotropy axis orientation. In this case the anisotropy axes of the bits are nearly parallel and the influence of the randomness given by the angle φ is negligible. Thus this situation is close to the uniaxial case which leads to the expected Stoner-Wohlfarth-like behavior with field angle. However, by increasing the tilt angle Θ, the switching field becomes independent of the applied magnetic field angle. At a first glance, this is a rather unexpected result but can be simply understood in terms of the torque acting on a magnetic moment of the individual bits: Here, the realization of φ for each individual bit plays a crucial role, as it could lead to either magnetization reversal in smaller fields (anisotropy axis of the bit is tilted i.e. 45° with respect to the applied magnetic field direction, shown in Fig. 5.19(a)), or higher fields (anisotropy axis of the bit is anti-parallel to the applied magnetic field direction Fig. 5.19(b)). As the angle φ is uniformly distributed within the array, an averaging over 64 bits results in the absence of the applied field angle dependence of the switching field.

Contrary to the angular dependence of the switching field, the angular dependence of the

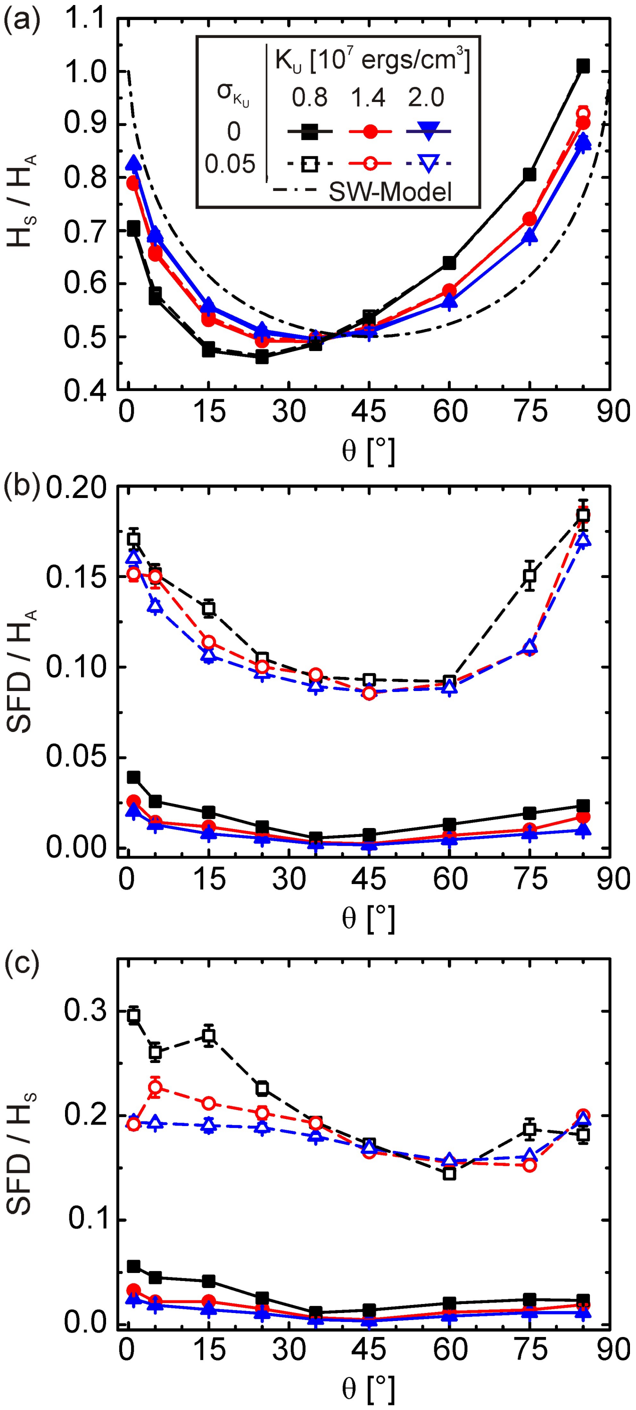

Figure 5.17: Influence of the magnetic anisotropy axis orientation on the (a) switching field and (b) switching field distribution for different magnetic anisotropy value. Both values are normalized to the anisotropy field. (c) Switching field distribution normalized to the switching field. Please note that the legend from subfigure (a) is applied to the other subfigures as well.

applied field on the SFD depends strongly on the intrinsic variation of the magnetic anisotropy constant (Fig. 5.20).

For small tilt angles $\Theta < 15°$, both SFD/H_A and SFD/H_S exhibit a minimum at 45°, as expected from the classical Stoner-Wohlfarth model (Fig. 5.20(a)). For larger tilt angles $15° < \Theta < 45°$, this minimum vanishes and the SFD becomes independent of the field angle. A further

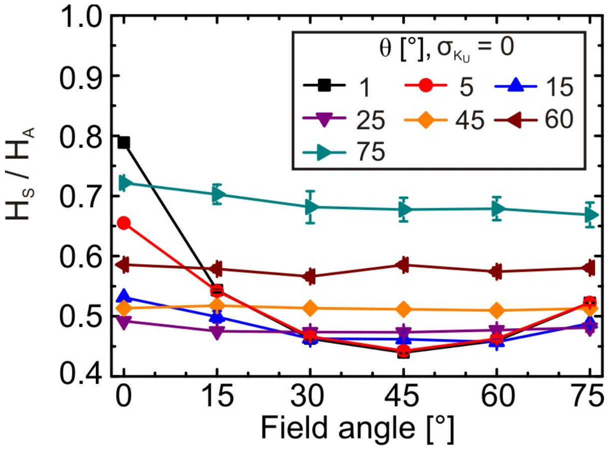

Figure 5.18: Influence of the applied field angle on the normalized switching field for bit arrays with different anisotropy axis orientations (tilt angle Θ).

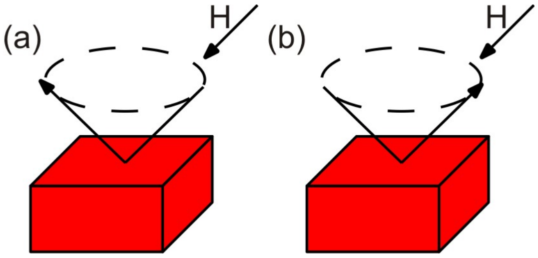

Figure 5.19: Relative orientation of the applied magnetic field and anisotropy axis direction of a bit for fixed tilt angle Θ being (a) perpendicular (large torque) and (b) parallel (small torque) to each other.

increase results in a continuous broadening of the SFD. By comparing Fig. 5.17 with Fig. 5.20, looking at $\sigma_{K_\mathrm{U}} = 0.05$, which is the more realistic case, it can be concluded that the configuration with $\Theta = 45° - 75°$ and applying the field under 0° gives the lowest SFD/H_S of about 0.15. This can be explained in terms of the torque acting on the magnetization of the individual bits. By choosing a magnetic field perpendicular to the surface, the worst case scenario, illustrated in Fig. 5.19, does not occur thus reducing the switching field distribution. By increasing the field angle, the situation shown in Fig. 5.19 becomes more and more present where the randomness of φ now worsens the SFD as discussed above.

5.2.3 Exchange coupled composite bit patterned media

5.2.3.1 Non-correlated layers

Again, an array of 8×8 bits with a center-to-center distance of 20 nm between two bits, leading to an areal density of about 1.5 Tbit/inch^2, is considered. Each bit has a lateral size of $10 \times 10\,\mathrm{nm}^2$ and possesses uniaxial magnetic anisotropy with a magnetic easy axis parallel to the surface normal ($\theta = 0$). To account for the unavoidable distribution of media properties, the

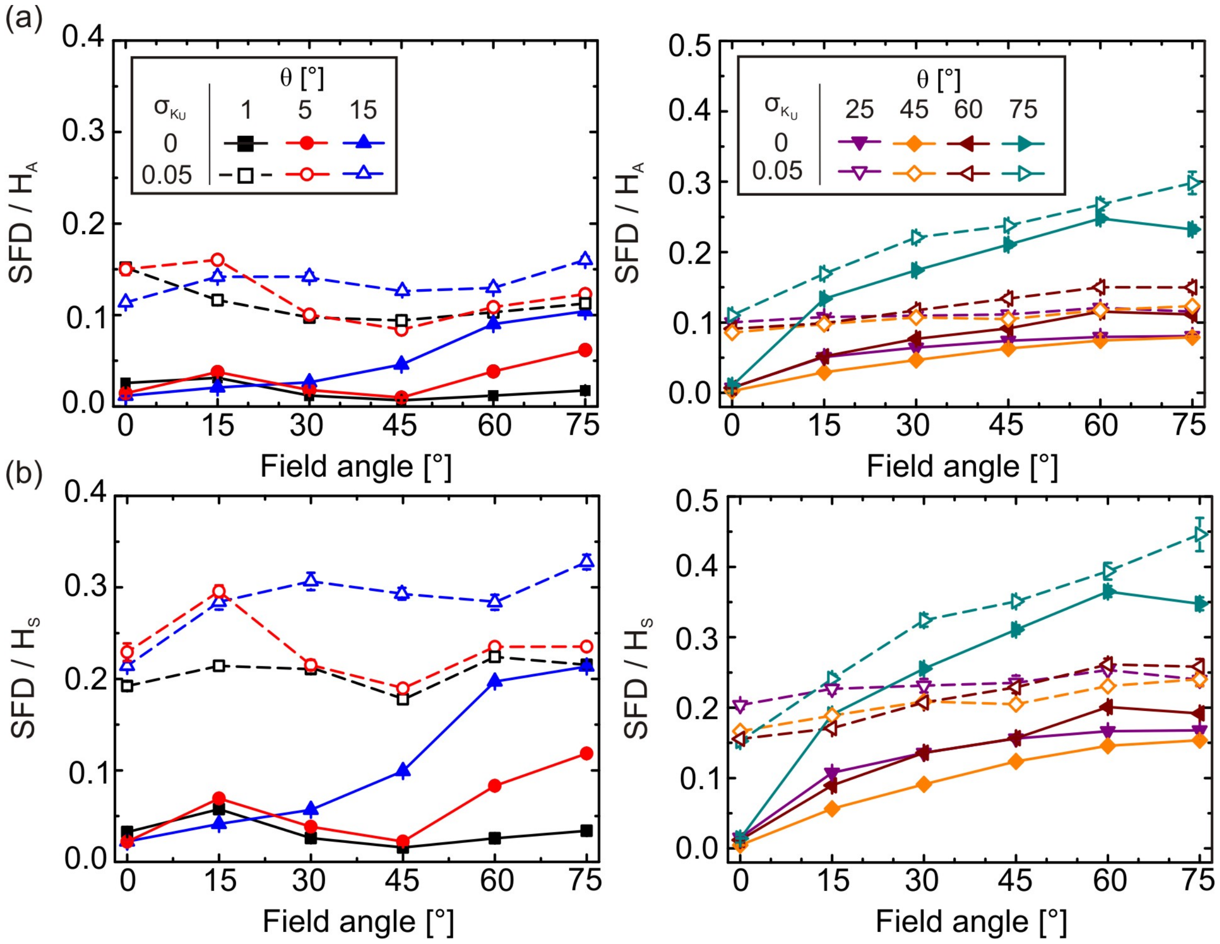

Figure 5.20: Dependence of the applied field angle on the SFD normalized to (a) H_A and (b) H_S for different values of σ_{K_U} and tilt angle Θ. K_U was set to 1.4×10^7 ergs/cm^3. Please note that the legend in (a) is also valid for (b).

magnetic anisotropy constant was varied with a Gaussian distribution (standard deviation of 0.05 K_U). In the following, we concentrate on bits composed of two and three layers with different magnetic anisotropy values assigned to each layer and compare the results with bits consisting of a hard magnetic single layer. Furthermore, a graded layer stack consisting of 10 layers with quadratically decreasing magnetic anisotropy value from the bottom to the top was investigated. Table 5.1 summarizes the geometrical and magnetic properties of the models under study. Both, the interlayer and intralayer exchange coupling constants were set to 1×10^{-6} ergs/cm to assure strong exchange coupling between the layers in the ECC stack. It was shown that, in the assumption of the uniform magnetization in the layer, weakening of the interlayer exchange coupling is beneficial with respect to lowering the switching field of the ECC bit [17]. However, detailed investigation performed accounting for the spatially inhomogeneous magnetization in the bit [105, 106] revealed that the energy barrier for magnetization reversal is maximal for a fully exchange coupled layer stack. Therefore, in the following, we focus on the fully exchange coupled case only.

#	layer stack		$K_\mathrm{U}[1 \times 10^7\,\mathrm{ergs/cm^3}]$	M_S [kG]	t [nm]
1a	single layer	hard	1.0 – 4.0	14	5
1b	single layer	hard	1.0 – 4.0	14	15
2	bilayer	hard	1.0 – 4.0	14	5
		soft	1.0	6	10
3	trilayer	hard	1.0 – 4.0	14	5
		medium	1.0	6	5
		soft	0.6	6	5
4	ten layers	graded	1.0 – 4.0	14	15

Table 5.1: Magnetic and geometrical properties of the bit arrays with various layer stacks. The thickness of the individual layers in the stack, t, and the corresponding magnetic properties are listed. K_U is the uniaxial magnetic anisotropy constant and M_S the saturation magnetization of the layer.

Figure 5.21 shows a sketch of the bit array with stack #3 (Table 5.1). In this case, a dark color represents a high magnetic anisotropy value while a brighter color corresponds to lower magnetic anisotropy values.

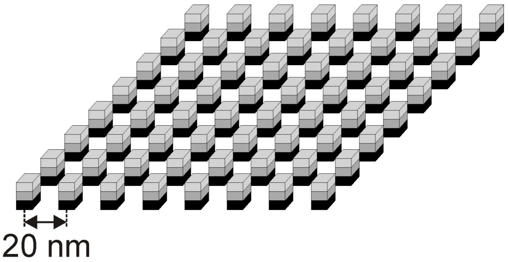

Figure 5.21: Model of 8 × 8 bits with each bit consisting of three layers with different magnetic properties (corresponds to stack #3, Table 5.1).

Figure 5.22 shows descending branches of exemplary hysteresis loops for the different layer stacks of Table I. The magnetic anisotropy value of the hard layer was set to $4 \times 10^7\,\mathrm{ergs/cm^3}$. With increasing number of layers in the stack, the switching field of the bit array decreases and the SFD becomes narrower. To further analyze the influence of the different stacks of a bit on H_S and SFD, these parameters were plotted as a function of the magnetic anisotropy value of the hard layer K_U^{hard} (Fig. 5.23).

With increasing K_U^{hard}, the switching field, H_S, increases (Fig. 5.23(a)). For single layer bits (stacks #1a, #1b), this increase is linear and a larger switching field was obtained for the thicker single layer (stack #1b). The latter is due to a modification of the shape anisotropy contribution leading to more incoherent magnetization reversal process. For the other investigated layer stacks (stacks #2-#4), there is a clear trend to saturation in the dependence $H_\mathrm{S}(K_\mathrm{U}^{hard})$. Please note that for $K_\mathrm{U}^{hard} > 5K_\mathrm{U}^{medium}$, a further increase of H_S is expected as the combined effect of the applied magnetic field and torque from the soft layer is insufficient to switch the magnetization

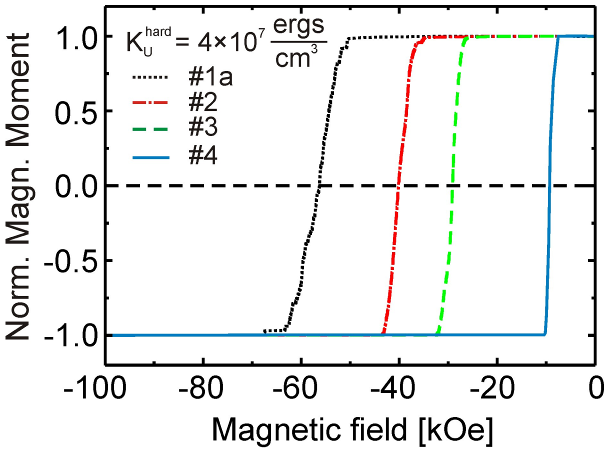

Figure 5.22: Descending branches of the hysteresis loops for various layer stacks given in Table 5.1. The uniaxial magnetic anisotropy constant of the hard layer was set to 4×10^7 ergs/cm^3.

of the hard layer [17]. However, due to computational limitations, simulations of magnetically harder layers were not performed. It is shown that with increasing number of layers in the ECC stack, the switching field successively decreases, reaching a value of about 9 kOe for graded media (stack #4; $K_\mathrm{U}^{hard} = 4 \times 10^7$ ergs/cm^3) considering a quadratic decrease of K_U over ten layers which is in agreement with previous studies [18].

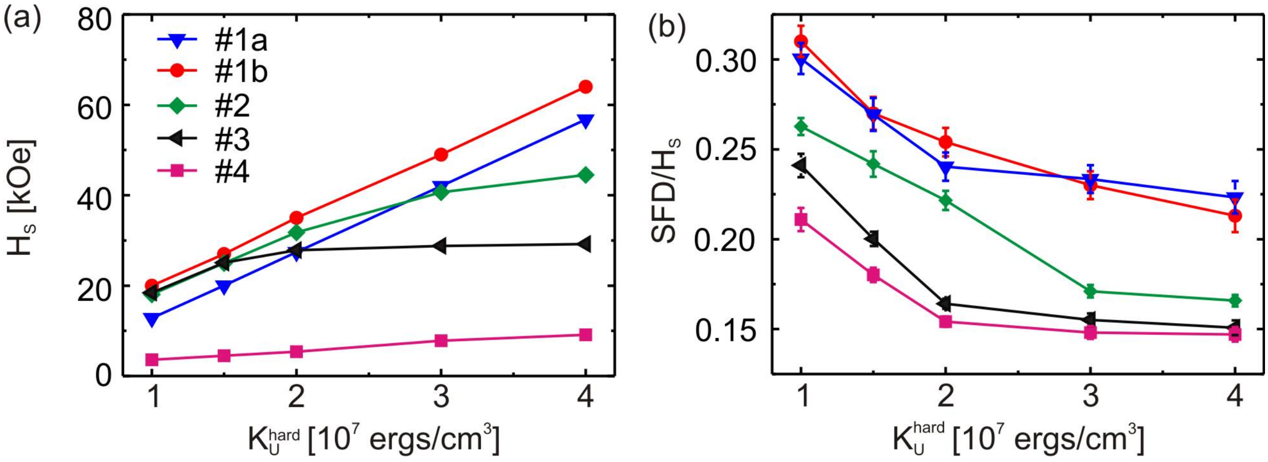

Figure 5.23: (a) Switching field and (b) normalized switching field distribution as a function of the magnetic anisotropy value of the hard layer for various layer stacks given in Table 5.1 for the case when the distributions of magnetic anisotropy values of the different layers are uncorrelated. Please note that the error bars in (a) are within the size of the symbols. Moreover, the legend of subfigure (a) applies to subfigure (b) as well.

Contrary to the behavior of $H_\mathrm{S}(K_\mathrm{U}^{hard})$, the normalized switching field distribution decreases with increasing K_U^{hard}, which is attributed to both, a change of the magnetization reversal mechanism of the media and a decrease of the influence of the dipolar fields from neighboring bits with increasing magnetic anisotropy value (Fig. 5.23(b)). With increasing number of layers in the stack, SFD/H_S decreases from about 0.23 for a bit composed of a single hard layer down to about 0.14 for graded media ($K_\mathrm{U}^{hard} = 4 \times 10^7$ ergs/cm^3). Moreover, the total thickness of the single layer for stack #1 has almost no influence on SFD/H_S.

Moreover, the energy barrier for the magnetization reversal, ΔE, at 300 K was simulated for the reversal process of one bit located in the central area of the array starting from an initially saturated state. Please note that this magnetic configuration is the most energetically unfavorable with respect to the magnetostatic interaction between the bits in the array. The magnetic anisotropy value of the hardest layer was set to 4×10^7 ergs/cm^3. The results for the different layer stacks are summarized in Table 5.2. As it follows from the data presented in Table 5.2, the stability of the ECC bits is only slightly reduced compared to the single layer bit (stack #1b). Moreover, the stability of the ECC bits is higher than the one of the single layer bits with a thickness of 5 nm (stack #1a), which can be explained in terms of an increased total thickness of the bits in stacks #2 and #3, where the added material is still magnetically relatively hard. By comparing the magnetic energy barriers and switching fields (Table 5.2), it can be seen that by tailoring the magnetic properties of the layer stacks of the bits, the switching field can be substantially reduced while keeping the magnetic energy barrier nearly constant.

	#1a	#1b	#2	#3	#4
$\Delta E[k_\mathrm{B}300\,\mathrm{K}]$	276	731	706	698	673
H_S[kOe]	56	65	44	29	9
SFD/H_S	0.22	0.21	0.17	0.15	0.14

Table 5.2: Energy barriers, ΔE, for magnetization reversal of the central bit in the array for the case when the distributions of the magnetic anisotropy values of the layers are not correlated. H_S and SFD/H_S are also given. The magnetic anisotropy value of the hard layer was set to 4×10^7 ergs/cm^3.

5.2.3.2 Correlated layers

In this section, it will be shown that by tailoring the correlation between the values of the distributions of the magnetic anisotropy values of the individual layers of ECC media, the switching field distribution of the bit array can be reduced significantly, while the switching field, H_S, remains unaffected.

The micromagnetic model

The size of the finite element mesh was set to 1 nm. We consider an array of 8×8 bits with a center-to-center distance of 20 nm between two bits, leading to an areal density of about 1.5 Tbit/inch^2. Each bit has a lateral size of 10×10 nm^2, a thickness of 15 nm, and possesses uniaxial magnetic anisotropy with a magnetic easy axis parallel to the surface normal. The saturation magnetization of all layers was set to 14 kG. The intralayer and interlayer exchange coupling constant was set to 1×10^{-6} ergs/cm. Please note that previous studies [105, 106] revealed that the energy barrier for magnetization reversal is maximal for a fully exchange coupled layer stack. Therefore, in the following, we focus on the fully exchange coupled (ECC) case only. However, the results are also valid for systems with reduced exchange coupling. Figure 5.24 shows a sketch of the bit array and the geometrical properties of a single bit. Please note that a dark color represents a high magnetic anisotropy value while a brighter color corresponds to lower magnetic anisotropy values.

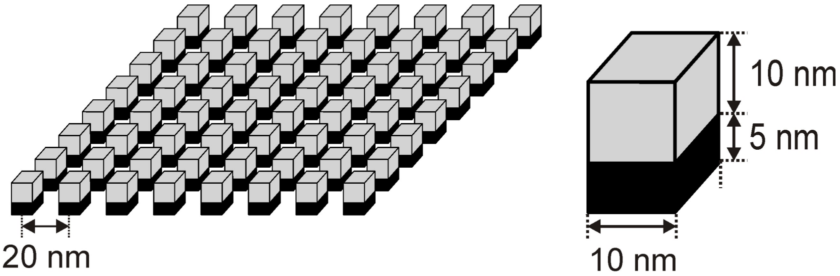

Figure 5.24: Model of 8 × 8 bits with each bit consisting of a hard (dark color) and a soft (bright color) magnetic layer.

To account for the unavoidable distribution of media properties, the magnetic anisotropy values of the bits in the array were varied with a Gaussian distribution with mean values $\overline{K_\mathrm{U}^\mathrm{soft}}$ and $\overline{K_\mathrm{U}^\mathrm{hard}}$ and corresponding standard deviations $\sigma_{K_\mathrm{U}}^\mathrm{soft}$ and $\sigma_{K_\mathrm{U}}^\mathrm{hard}$ for the soft and hard layer, respectively. Thereby, a correlation between the values of the two distributions expressed by a correlation factor C can be introduced in the following way: At first for each bit, a magnetic anisotropy value of the hard layer, $K_\mathrm{U}^\mathrm{hard}$, was randomly chosen from the Gaussian distribution (mean value $\overline{K_\mathrm{U}^\mathrm{hard}}$, standard deviation $\sigma_{K_\mathrm{U}}^\mathrm{hard}$) and assigned to the respective hard layer of the bit. From $K_\mathrm{U}^\mathrm{hard}$, the fully correlated value (C = 1) for the soft layer, $K_\mathrm{U}^\mathrm{soft,\ cor}$, was calculated as follows:

$$K_\mathrm{U}^\mathrm{soft,\ cor} = \frac{\overline{K_\mathrm{U}^\mathrm{soft}}}{\overline{K_\mathrm{U}^\mathrm{hard}}} \cdot K_\mathrm{U}^\mathrm{hard} \tag{5.2}$$

Then, for each bit, an uncorrelated (C = 0) magnetic anisotropy value of the soft layer, $K_\mathrm{U}^\mathrm{soft,\ uncor}$, was randomly chosen from the Gaussian distribution (mean value $\overline{K_\mathrm{U}^\mathrm{soft}}$, standard deviation $\sigma_{K_\mathrm{U}}^\mathrm{soft}$). Finally, the magnetic anisotropy value of the soft layer of each bit, $K_\mathrm{U}^\mathrm{soft}$ can be calculated:

$$K_\mathrm{U}^\mathrm{soft} = (1 - C) \cdot K_\mathrm{U}^\mathrm{soft,\ uncor} + C \cdot K_\mathrm{U}^\mathrm{soft,\ cor} \tag{5.3}$$

Simulations for each model were carried out 30 times, whereas for each run, a new set of magnetic anisotropy values was chosen as described above and assigned to the bits. Furthermore, only the descending branch of the hysteresis loop (from +10 kOe to −100 kOe) was simulated with a magnetic field sweep rate of 1 kOe/ns. The magnetic field was applied under an angle of 3° to avoid numerical instabilities. The magnetic parameters of interest (H_S and SFD) were determined using statistical averaging over all 30 runs for each model, resulting in a distribution shown as error bars. The SFD was determined as the field difference between 90% and −90% of the saturation magnetization of the hard layer of the ECC stack.

Results

Figure 5.25(a) shows the normalized switching field distribution of the bit array as a function of the correlation factor C for different values of $\overline{K_\mathrm{U}^\mathrm{hard}}$. The magnetic anisotropy value of the soft layer was set to $1 \times 10^7\,\mathrm{ergs/cm^3}$. Both, $\sigma_{K_\mathrm{U}}^\mathrm{soft}$ and $\sigma_{K_\mathrm{U}}^\mathrm{hard}$ were chosen to be 5% of their respective mean value. Please note that the switching field, H_S, was not influenced by a correlation of the values of the distributions of the magnetic anisotropy values (not shown). For values of the magnetic anisotropy of the hard layer close to the one of the soft layer ($\overline{K_\mathrm{U}^\mathrm{soft}} = 1 \times 10^7\,\mathrm{ergs/cm^3}$), the smallest SFD/$H_\mathrm{S}$ is achieved at $C = 0$, while an increasing correlation leads to a gradual increased SFD/H_S. In this case, the bit can nearly be treated as a single phase bit and an increased correlation leads to an increased appearance of bits with (high $K_\mathrm{U}^\mathrm{hard}$)/ (high $K_\mathrm{U}^\mathrm{soft}$) or (low $K_\mathrm{U}^\mathrm{hard}$) / (low $K_\mathrm{U}^\mathrm{soft}$) combinations which results in a broadening of the switching field distribution [97]. However, in the case of high magnetic anisotropy values of the hard layer ($2 \times 10^7\,\mathrm{ergs/cm^3}$ - $4 \times 10^7\,\mathrm{ergs/cm^3}$), the shown functions SFD/H_S exhibits a minimum at about $C = 0.5$. The reason for this minimum is an interplay of two effects:

1. an increased correlation leads to increased appearance of hard/hard and soft/soft bits, as described above
2. an intermediate correlation leads to a reduction of the possible K_U values of the soft magnetic layer (equation 5.3) and thus indirectly narrows $\sigma_{K_\mathrm{U}}^\mathrm{soft}$

Figure 5.26 shows an example of two randomly chosen (uncorrelated) values of the magnetic anisotropy of the soft layer (top part of the image, very left and very right) and the resulting values for a correlation factor $C = 0.5$.

Whereas the uncorrelated values ${K_U}_{1,2}^{\text{soft, uncor}}$ have a relatively broad distribution in the shown example (dark grey box), the resulting values have a smaller distribution due to the correlation with $K_\mathrm{U}^\text{soft, cor}$ (light grey box). This reduction of the distribution of $K_\mathrm{U}^\mathrm{soft}$ finally leads to the narrowing of the switching field distribution of the bit array.

Figure 5.25(b) shows the normalized switching field distribution as a function of the correlation factor C for different $\sigma_{K_\mathrm{U}}^\mathrm{soft}$. The distribution of the hard magnetic layer, $\sigma_{K_\mathrm{U}}^\mathrm{hard}$, was set to 5%, $\overline{K_\mathrm{U}^\mathrm{hard}}$ to $4 \times 10^7\,\mathrm{ergs/cm^3}$, and $\overline{K_\mathrm{U}^\mathrm{soft}}$ to $1 \times 10^7\,\mathrm{ergs/cm^3}$. The switching field, $H_\mathrm{S} \approx 40\,\mathrm{kOe}$, is not influenced by the correlation. Three different cases dependent on the standard deviations of the individual distributions can be distinguished:

1. $\sigma_{K_\mathrm{U}}^\mathrm{soft} < \sigma_{K_\mathrm{U}}^\mathrm{hard}$: The normalized switching field distribution is smallest for $C = 0$. Therefore, the uncorrelated case is preferential for ECC/BPM media with narrow $\sigma_{K_\mathrm{U}}^\mathrm{soft}$

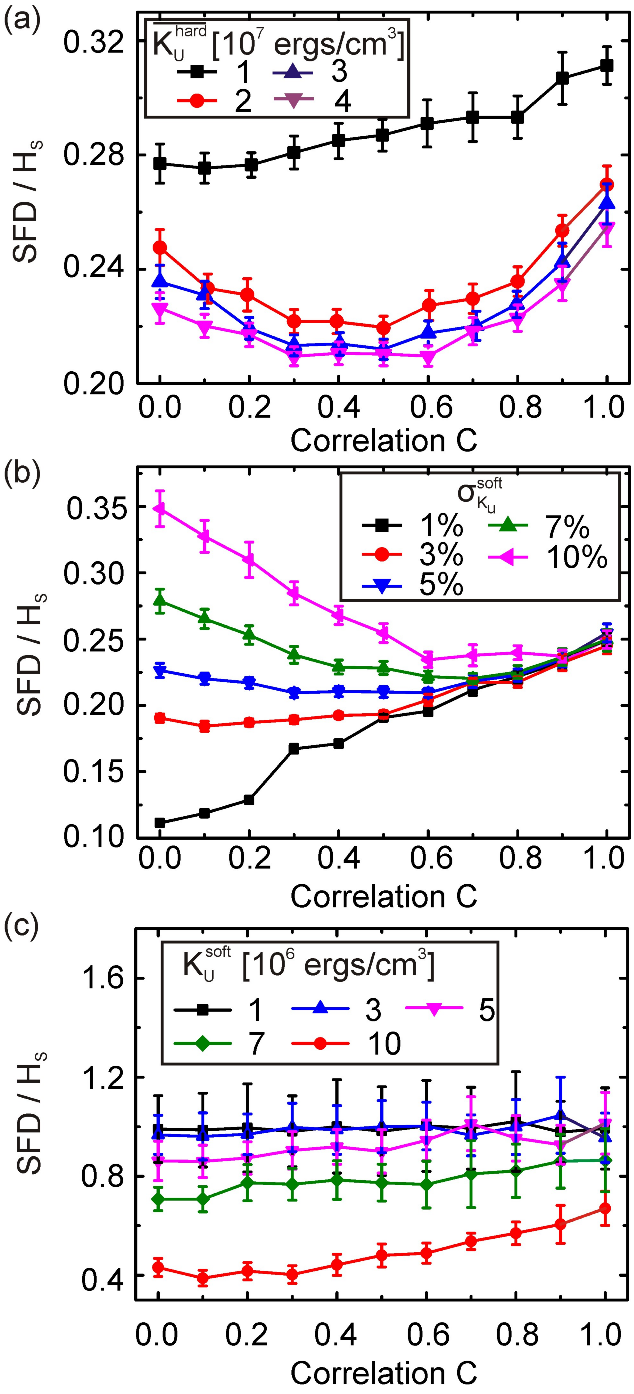

Figure 5.25: Normalized switching field distribution as a function of the correlation factor C between the magnetic anisotropy values of the individual layers for (a) different $K_{\mathrm{U}}^{\mathrm{hard}}$, (b) different $\sigma_{K_{\mathrm{U}}}^{\mathrm{soft}}$, and (c) different $K_{\mathrm{U}}^{\mathrm{soft}}$.

2. $\sigma_{K_{\mathrm{U}}}^{\mathrm{soft}} \approx \sigma_{K_{\mathrm{U}}}^{\mathrm{hard}}$: The normalized switching field distribution exhibits a minimum at about $C \approx 0.5$. Therefore, the partly correlated case is preferential if the distributions have approximately the same standard deviation.

3. $\sigma_{K_{\mathrm{U}}}^{\mathrm{soft}} > \sigma_{K_{\mathrm{U}}}^{\mathrm{hard}}$: The normalized switching field distribution is mainly given by $\sigma_{K_{\mathrm{U}}}^{\mathrm{hard}}$ and is not affected by $\sigma_{K_{\mathrm{U}}}^{\mathrm{soft}}$. Therefore, the ECC reduces the influence of the distribution of the

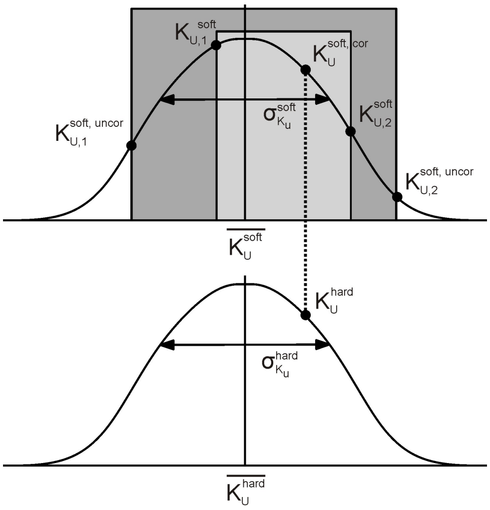

Figure 5.26: Schematic illustration of a correlation between the distributions of the magnetic anisotropy values of the individual layers. The chosen example is for two bits. For simplicity, both bits possess the exactly same magnetic anisotropy value of the hard layer but different ones for the soft layer. A correlation factor of 0.5 was assumed.

soft layer on the SFD of the system if the correlation factor is high ($C > 0.8$).

Figure 5.25(c) shows the normalized switching field distribution as a function of the correlation factor C for different magnetic anisotropy constants of the soft layer. As experiments have shown that the anisotropy distributions of the magnetic hard layer is usually in the region of about 20%, $\sigma_{K_\mathrm{U}}^{\mathrm{hard}}$ was set to 0.2 and $\sigma_{K_\mathrm{U}}^{\mathrm{soft}}$ was set to 0.05. The magnetic anisotropy constant of the hard layer was fixed at $4 \times 10^7\,\mathrm{ergs/cm^3}$. For very small values of $K_\mathrm{U}^{\mathrm{soft}}$, the normalized SFD does not depend on the correlation factor as the reversal of the magnetic hard layer is rarely influenced by the magnetic soft layer due to the large difference in magnetic anisotropy values and the medium can thus be seen as a single-layer BPM. With increasing $K_\mathrm{U}^{\mathrm{soft}}$, the difference in the magnetic anisotropy constant between the hard and the soft layer decreases. As for the small values of $K_\mathrm{U}^{\mathrm{soft}}$, there are some bits which do show an independent switching of the hard and soft layer, this decreased difference results to a narrower switching field distribution of the entire bit array. Moreover, especially for $K_\mathrm{U}^{\mathrm{soft}} = 1 \times 10^7\,\mathrm{ergs/cm^3}$, with increasing correlation factor, the normalized SFD increases due to the reasons explained above.

Next to the definition of correlated distributions used before, also other types of correlation, as for example anti-correlation can be employed. First micromagnetic simulations of anti-correlated ECC systems have shown an actual improvement of the SFD, but further detailed investigations need to be carried out to draw a distinct conclusion. However, another rather straight forward definition of correlation in bit patterned media is given in the following way:

$$K_\mathrm{U}^{\mathrm{soft}} = K_\mathrm{U}^{\mathrm{soft,\ cor}} \qquad \text{for a probability of } C \tag{5.4}$$

$$K_\mathrm{U}^{\mathrm{soft}} = K_\mathrm{U}^{\mathrm{soft,\ uncor}} \qquad \text{for a probability of } (1 - C) \tag{5.5}$$

This definition means that if for example $C = 0.8$, 80% of all bits in the simulated bit array are fully correlated (meaning that the magnetic anisotropy values of the individual layers are correlated), while 20% of the bits are uncorrelated. Identical simulations using the same parameter sets as used for the initial definition of correlation were performed. The obtained results are in general quite similar. But, there are also differences, for instance, the minimum of the normalized switching field distribution for intermediate values of the correlation factor C, as observed for different magnetic anisotropy values of the hard layer (fig. 5.25(a)), or for different distributions of the magnetic soft layer (fig. 5.25(b)), does not occur with the latter definition of correlation. However, this behavior is consistent with the explanation given above as visualized in figure 5.26. In more detail, in this case, an intermediate correlation factor does no longer lead to a reduction of the possible K_{U} values of the soft magnetic layer and thus does not induce a narrower $\sigma_{K_{\mathrm{U}}}^{\mathrm{soft}}$, as it was the case when using the initial definition of correlation.

5.3 Investigation on the magnetization reversal of a magnetic dot array of Co/Pt multilayers [3]

A systematic study on the magnetic properties of a dot array consisting of Co/Pt multilayers patterned by electron beam lithography with dot sizes between 200 nm and 40 nm, keeping the filling factor constant at about 0.16, will be presented. The evolution of the nucleation, switching and saturation fields will be discussed as a function of the dot size. Moreover, the magnetization reversal process of individual dots with different sizes was simulated by solving the Landau-Lifshitz-Gilbert equation.

5.3.1 Sample preparation and experimental techniques

Co/Pt multilayers were deposited on thermally oxidized Si(100) wafers with a 100 nm-thick SiO_2 layer in a molecular beam epitaxy (MBE - see section 4.2) chamber equipped with an electron gun loaded with Co and Pt (purity greater than 99.99%). The base pressure was 4×10^{-11} mbar and the pressure during deposition did not exceed 5×10^{-9} mbar. The multilayer stack consisting of $[\mathrm{Co}(0.3\ \mathrm{nm})/\mathrm{Pt}(0.8\ \mathrm{nm})]_8$ was deposited on a 5 nm-thick Pt buffer layer to provide the required texture for the multilayer growth. An additional 3 nm-thick Pt cover layer was deposited to protect the sample from oxidation. The magnetic characterization was performed using a superconductive quantum interference device (SQUID - see section 4.4) magnetometer, revealing a saturation magnetization of about $M_\mathrm{S} = 480\,\mathrm{emu/cm^3}$ and a uniaxial magnetic anisotropy constant of about $K_\mathrm{U} = 3 \times 10^6\,\mathrm{ergs/cm^3}$. Subsequently, the multilayer film was patterned using electron beam lithography (EBL). EBL was carried out using a LEICA 5000+ Electron Beam nanowriter working at 100 kV. A conventional process using the resist PMMA (Poly(methyl methacrylate)) and lift off technique was applied. The pattern transfer in the magnetic layer after the lithographic process was performed by an ion beam etching process. Scanning electron microscopy images of the samples after patterning are presented in figure 5.27.

Hexagonal arrays with different dot sizes and different pitches were created, while holding the filling factor constant at 0.16. A hexagonal arrangement was chosen as this arrangement is the preferred one from an application point of view as it provides the highest areal density. The dimensions of the patterns are given in table 5.3.

The integral magnetic properties of the patterned samples were characterized by polar magneto-optical Kerr effect (MOKE - see section 4.5) magnetometry using a focused beam operating at a wavelength of 670 nm. The external magnetic field was applied perpendicular to the substrate plane. In addition to hysteresis loops, revealing the presence of an out-of-plane easy axis of magnetization, remanence curves were taken. The shape of the hysteresis loops and remanence curves was found to be identical, suggesting irreversible magnetization reversal processes. Therefore, in the following we concentrate on the discussion of the remanence curves. Additionally,

---

[3] Results have been published in [73]

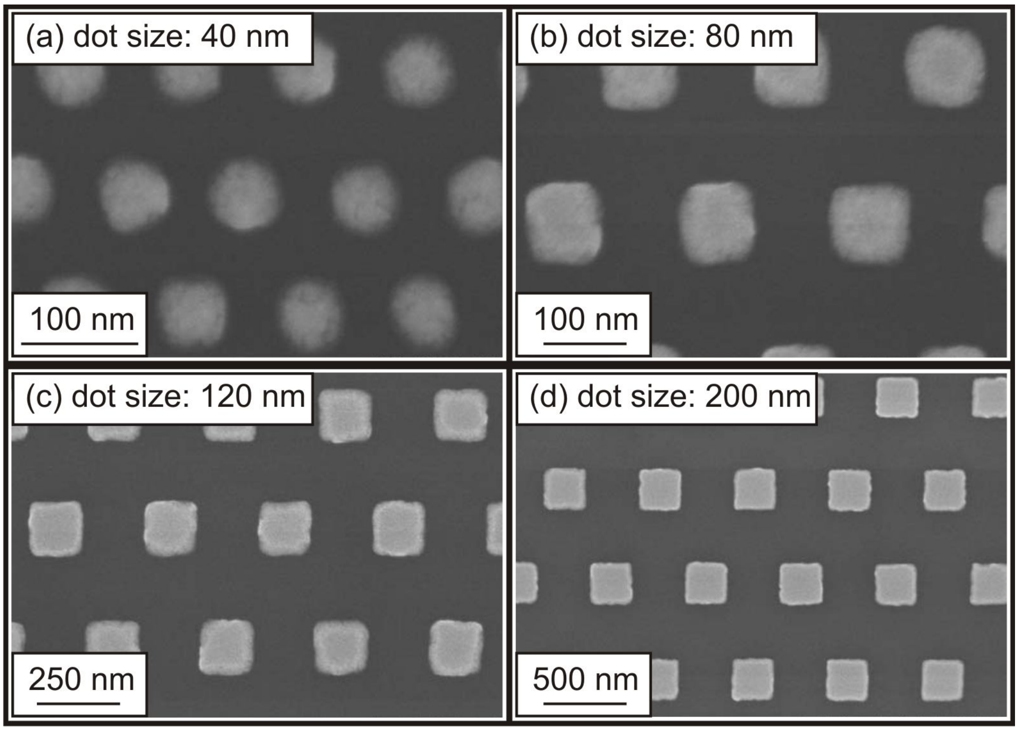

Figure 5.27: SEM images taken after the patterning process.

magnetic force microscopy (MFM) imaging was performed to investigate the magnetic properties of individual dots both in remanence and in an applied magnetic field.

Sample	dot size [nm]	period [nm]
1	40	100
2	80	200
3	120	300
4	200	500

Table 5.3: Dot size and pattern period of the samples under study.

5.3.2 Magnetic Characterization

5.3.2.1 Magnetic Force Microscopy study

MFM images of the patterned samples were taken in the ac-demagnetized state and after setting a reverse field H_R of $-2.75\,\mathrm{kOe}$ to the initially saturated samples (figure 5.28). The study performed on the dot array with the smallest dot size of 40 nm reveals that individual dots are in a magnetic single-domain state independent of the magnetic history (figures 5.28(a,b)). Please note that for this dot array, the applied field of $-2.75\,\mathrm{kOe}$ is already larger than the coercive field and thus, more than 50% of all dots are already switched. In contrast, MFM data taken on the array with 200 nm dot sizes reveal that the nanostructures are in a clear multi-domain state (figures 5.28(g, h)). The patterns with dot sizes of 80 nm and 120 nm are at the border between single- and multi-domain state as indicated by the presence of dots which are showing either a single-domain or multi-domain state (figures 5.28(c-f)).

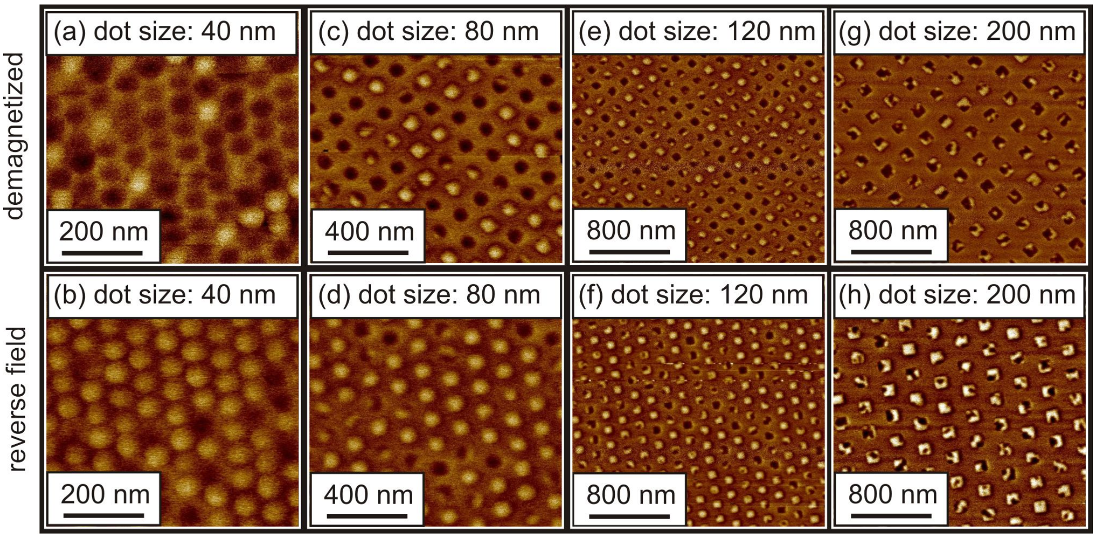

Figure 5.28: MFM images taken in the ac-demagnetized state (a, c, e, g) and after setting a reverse field $H_\mathrm{R} = -2.75\,\mathrm{kOe}$ to an initially saturated dot array (b, d, f, h).

To study the magnetization reversal process of individual dots in the multi-domain state, in-field MFM measurements were carried out on the dot array with a dot size of 200 nm. Figure 5.29 shows the evolution of the magnetization reversal in different applied magnetic fields perpendicular to the sample plane.

It can be seen that the reversal of the dots starts with the nucleation of a magnetic domain at the edges of the dots, most likely due to defects resulting from the patterning process (see white circle in figure 5.29(a)). However, there are also dots where the magnetization reversal occurs around the center of the dots due to the larger demagnetizing field in the dot center (see white circle in figure 5.29(b)). With increasing magnetic field, the nucleated domains spread over a certain distance and eventually gets pinned on structural inhomogeneities, i.e. at the boundaries between neighboring Co/Pt grains. This process is accompanied either by depinning of the magnetic domains or by further nucleation of domains in the same dot and its spread leading to the complete magnetization reversal. Similar domain patterns were already observed in patterned CoCrPt perpendicular media [107]. Our study shows that the magnetization reversal process in the array of dots with a size of 200 nm is nucleation dominated, whereas the coercive field is determined by pinning of magnetic domain walls on structural inhomogeneities. Moreover, it is worth mentioning that the nucleation process is deterministic, always starting at the same location of the dots when the same reverse field is applied.

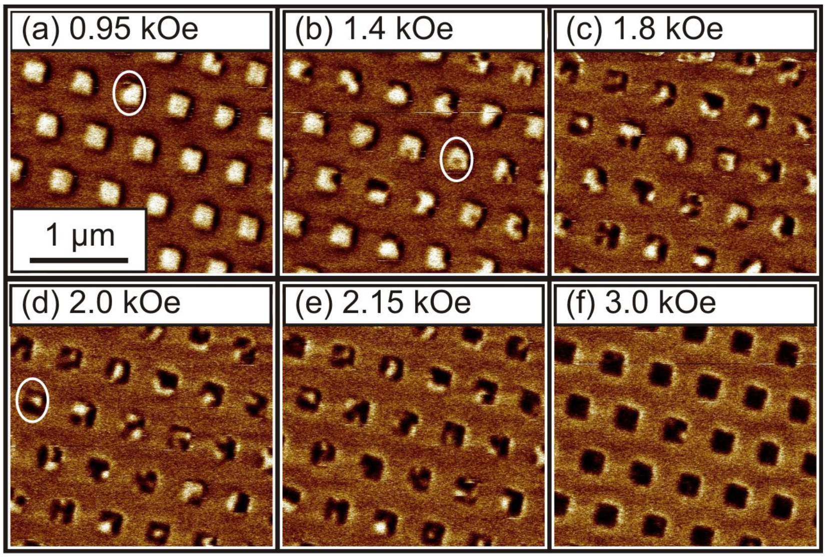

Figure 5.29: In-field-MFM images of an array with a dot size of 200 nm taken at (a) 0.95 kOe, (b) 1.4 kOe, (c) 1.8 kOe, (d) 2.0 kOe, (e) 21.5 kOe and (f) 3.0 kOe. Note that the images were taken at the same location to follow the evolution of the magnetization reversal.

5.3.2.2 Integral magnetic properties

A series of remanence curves as measured by p-MOKE is shown in figure 5.30(a). From these curves, the first derivative of the normalized magnetization with respect to the magnetic field was extracted (figure 5.30(b)). In this case, the field corresponding to the maximum of the first derivative corresponds to the averaged switching field, H_S, while the full width at half maximum corresponds to the switching field distribution (SFD). Moreover, the nucleation field H_nuc is defined as the field where the magnetization of the array reaches 90% of the saturation magnetization (figure 5.30(a)). Accordingly, the saturation field, H_sat, is defined as the field where the magnetization of the array reaches -90% of the saturation magnetization. Figure 5.30(c) shows the dependence of the switching field, nucleation field, saturation field, and switching field distribution on the dot size. The analysis shows that H_S as well as H_nuc increases with increasing dot size, whereas H_sat does not vary much with the dot size (Figure 5.30(c)). The saturation field is determined by the magnetization reversal of the magnetic hardest parts of the dots. The patterning divides the initially exchange coupled film into exchange-decoupled regions. The magnetic hard parts are then distributed over the individual dots. Assuming that the magnetic hard parts of the Co/Pt multilayers are smaller than the dot sizes, this will lead to the observed independency of the saturation field on the dot size.

The reduction of the dot size below 200 nm results in a modification of the magnetization reversal mechanism from domain wall nucleation and propagation to coherent/incoherent rotation of the magnetization (see micromagnetic simulations below). It is important to note that a coherent reversal process is accompanied by a substantial increase in H_C, compared to the

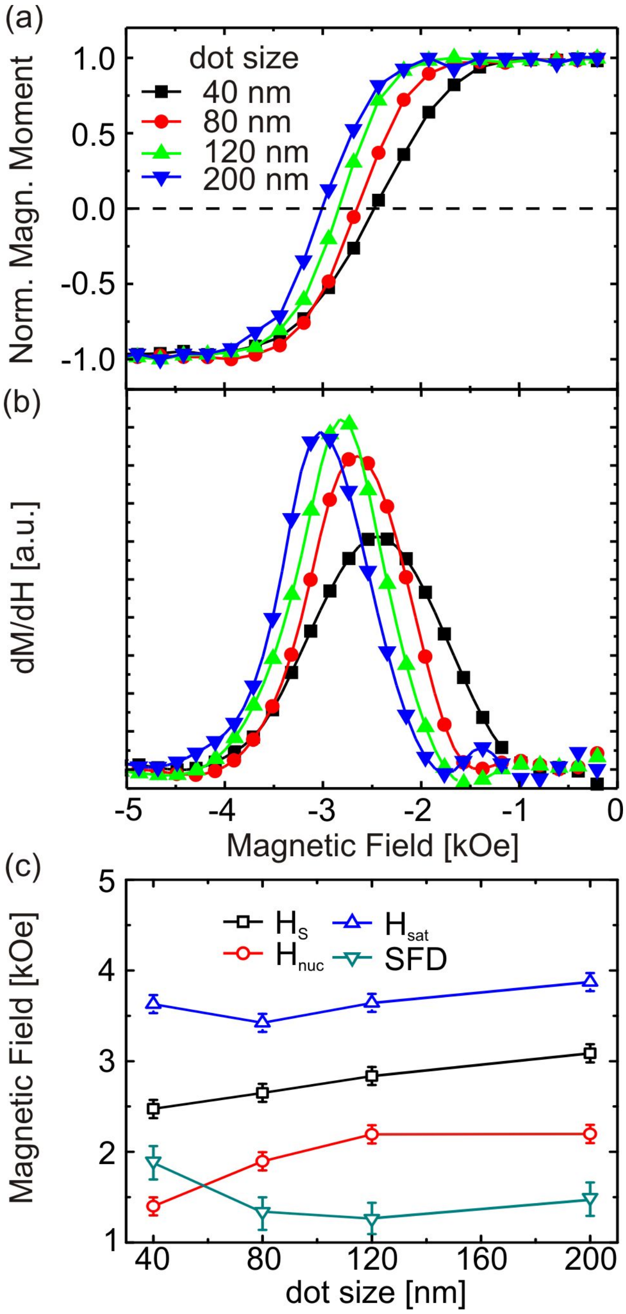

Figure 5.30: (a) MOKE remanence curves measured of the four investigated dot arrays, (b) derivative of the remanence curve with respect to the magnetic field, and (c) extracted nucleation field H_{nuc}, switching field H_{S}, saturation field H_{sat}, and switching field distribution (SFD).

incoherent reversal mechanisms [108–110]. Therefore, the further lowering of the switching and nucleation field with reduction of the dot size can be explained by an incoherent magnetization reversal process. In addition, a degradation of the magnetic properties induced by the patterning process is expected. With decreasing dot size, the relative area, that gets affected by the patterning process increases, resulting in a lowering of the magnetic anisotropy value of the magnetic material, finally leading to a reduction of the switching field [111]. Indeed, the SEM images show an increased roughness at the edges of the individual bits at smaller dot sizes, revealing even a change of the shape of the dots from rectangular to a more round shape. Moreover, the reduction of the switching field is accompanied with a substantial broadening of the switching field distribution in particular for the array with 40 nm dots.

5.3.3 Micromagnetic simulations

To investigate the change of the reversal mechanism and thus the change of the switching field, micromagnetic simulations of individual dots with different sizes from 200 nm down to 10 nm were performed (figure 5.31). The mesh size of the micromagnetic model was about 2 nm. Please note that the simulations were performed at zero temperature.

The saturation magnetization was assumed to be 480 emu/cm^3, based on SQUID results of the film sample. The magnetic anisotropy value was varied between 2×10^6 ergs/cm^3 and 5×10^6 ergs/cm^3. The magnetic easy axis was set perpendicular to the base plane of the dot and the field was applied under an angle of 3° relative to the surface normal to avoid numerical instabilities of the simulation related to the vanishing torque acting on the magnetic moment by the external magnetic field. Figure 5.31(a) shows the switching field as function of the dot size for different values of the magnetic anisotropy constant. The switching field decreases with increasing dot size due to different magnetization reversal mechanisms, and increases with increasing magnetic anisotropy constant, as expected. Thus, the switching field of a smaller dot can be larger than the switching field of a larger dot due to different magnetic anisotropies, which can explain the observed experimental data. The temporal evolution of the magnetization for $K_\mathrm{U} = 3 \times 10^6$ ergs/cm^3 is depicted in subfigures 5.31(b)-(d). Please note that the shown magnetization states are snapshots of the magnetization reversal process and are not stable.

The nearly cubic dot with a side length of 10 nm and a thickness of 9 nm changes its magnetization by quasi-coherent rotation as predicted by Rave et al. [94], a process that is rather similar to the classical Stoner-Wohlfarth reversal [112]. The magnetization rotates around the applied field, changing its direction from positive to negative (figure 5.31(b)). By increasing the side length of a dot from 10 nm to 40 nm, the magnetization reversal mode changes from quasi-coherent rotation to incoherent rotation via non-equilibrium two-domain state formation with twisted vortices (figure 5.31(c)) [Rave1998]. While figure 5.31(c)-I shows the saturated state of the dot at 0 kOe, figure 5.31(c)-II shows the beginning of the magnetization reversal process. Figure 5.31(c)-III clearly reveals the formation of domains, finally ending in a fully reversed state as presented in figure 5.31(c)-IX. By further increasing the side length to 200 nm, the magnetization reversal mechanism changes again. Noticeably, the nucleation of the domain does not happen at a corner but at the center of the dot (figure 5.31(d)-II). After the nucleation, two other reverse domains closer to two opposite corners of the dot nucleate (figure 5.31(d)-

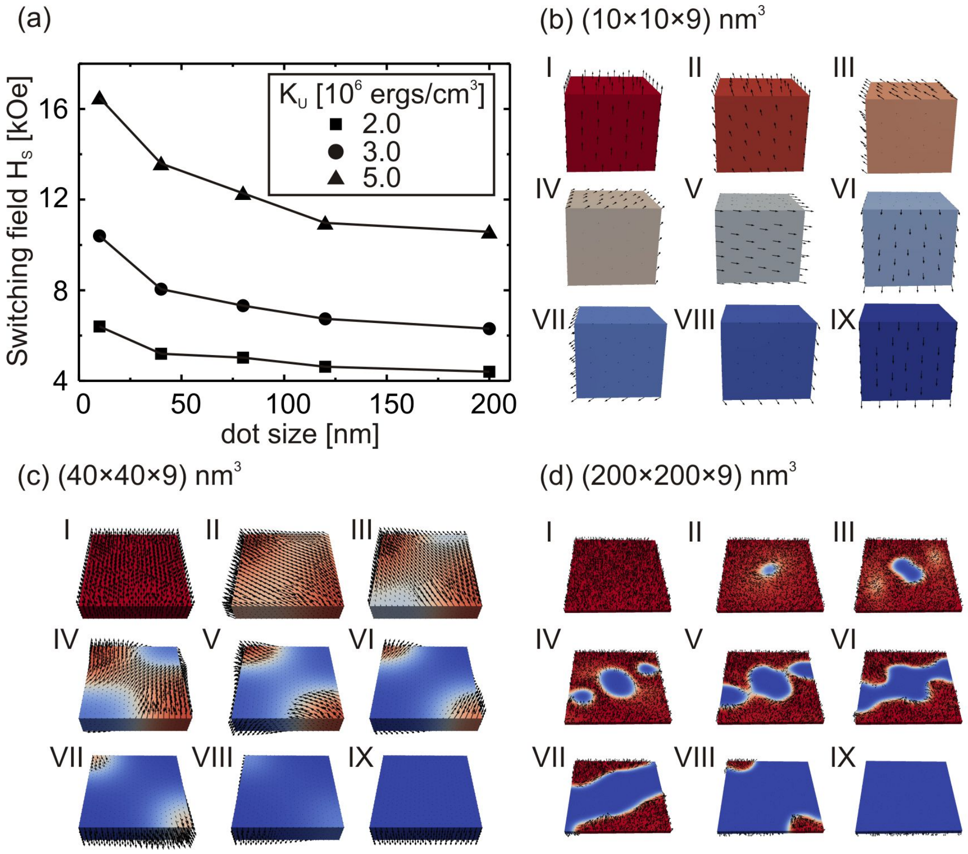

Figure 5.31: (a) Switching field dependence on the magnetic anisotropy constant and the dot size, and (b)-(d) different steps of the reversal of a single dot with various sizes of (b) $(10 \times 10 \times 9)$ nm^3, (c) $(40 \times 40 \times 9)$ nm^3, and (d) $(200 \times 200 \times 9)$ nm^3 using $K_\mathrm{U} = 3 \times 10^6$ ergs/cm^3. Please note that the images (I) are taken at zero field and (IX) at -20 kOe. The other steps of the reversal are taken as snapshots during the magnetization reversal process.

IV), finally merging with the first domain (Fig. 5(d)-V). Subsequently, the domain propagates through the entire dot, ending in a fully reversed magnetization of the dot (figure 5.31(d)-IX). This behavior is relatively similar to the experimental finding where the domain nucleation of some dots indeed starts in the center of the dots due to the larger demagnetizing field in the dot center.

5.4 Nanocap arrays of granular CoCrPt:SiO$_2$ films on silica particles: Tailoring of the magnetic properties by Co$^+$ irradiation[4]

5.4.1 Introduction

Various lithography approaches are widely used to fabricate ordered arrays of magnetic nanostructures [9, 107, 114]. However, since these approaches are time-consuming and expensive, methods based on self-assembly of magnetic nanostructures are rather attractive [39]. In this respect, self-assembly of non-magnetic spherical particles with defined magnetic properties provided by a magnetic film deposited onto the particles [115] is used. This enables an elegant way to create magnetic nanostructure arrays with strong perpendicular magnetic anisotropy as required for high thermal stability [116–120]. In addition, Kappenberger et al. [121] recently used a template-directed self-assembly process to arrange spherical particles as small as 20 nm demonstrating the feasibility to create particle arrays with long-range order. Besides the template fabrication, a lot of work was performed on the modification of the magnetic properties of CoCrPt:oxide media to achieve the best recording performance. Conventionally, tailoring the magnetic properties of such a granular system is achieved by varying a number of deposition parameters, as for example the buffer layer stack, the deposition pressure, or the content of the nonmagnetic component [122–124]. However, influencing the magnetic properties using ion irradiation with either non-magnetic, i.e. Ga, He, and Ar [114, 125–129] or magnetic ion specimens, i.e. Co [130], was recently introduced. In this work, the possibility to tune the magnetic properties of CoCrPt:SiO$_2$ films grown on self-assembled arrays of SiO$_2$ spherical particles using irradiation with magnetic Co$^+$ ions is demonstrated. By using magnetic ions, a direct influence on the intergranular exchange by introducing Co atoms into the grain boundaries can be exerted, which allows to tailor the magnetic exchange coupling between CoCrPt grains in a controlled manner [130], thus influencing the integral magnetic properties, i.e. remanence magnetization, coercive field, and magnetic domain configuration. Structural properties of the particle samples were investigated by scanning electron microscopy (SEM) and transmission electron microscopy (TEM) in conventional and high resolution (HR) mode. The local magnetic properties at room temperature were probed using magnetic force microscopy (MFM), whereas the integral magnetic properties of the samples were characterized using superconducting quantum interference device (SQUID) magnetometry.

5.4.2 Sample preparation and ion irradiation

Monolayers of self-assembled SiO$_2$ particles of various sizes from 10 to 330 nm were prepared using a method proposed by Micheletto et al. [131]. A droplet of a particle/solvent mixture was put onto a thermally oxidized silicon wafer and evaporated under ambient conditions. On

---

[4] Results have been published in [113]

these SiO_2 particle monolayers, granular CoCrPt:SiO_2 films were magnetron sputtered on top of a Ta adhesion layer and a two-step Ru seed layer stack at room temperature using Ar^+ with a sputter pressure of 7×10^{-2} mbar. The magnetic layer was then covered with a diamond-like carbon (DLC) overcoat to prevent oxidation and to protect the surface. The entire layer stack is as follows:

$DLC(4nm)/[(Co_{90}Cr_{10})_{80}Pt_{20}]_{88}\text{-}(SiO_2)_{12}(15nm)/Ru(12nm)/$
$Ru(8nm)/Ta(5nm)/substrate.$

In addition to the particle samples, a series of reference samples was also prepared on planar thermally oxidized Si(100) wafers with a 100 nm-thick SiO_2 layer. The deposition parameters were adjusted in order to achieve pronounced perpendicular magnetic anisotropy, high remanent magnetization, and strong decoupling between CoCrPt grains. The corresponding SQUID magnetic hysteresis loops of the reference sample are shown in Fig. 5.32.

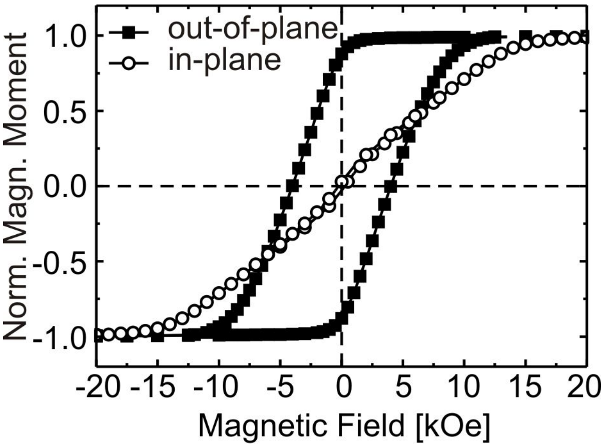

Figure 5.32: SQUID hysteresis loops of the reference sample measured in out-of-plane and in-plane geometry.

The shape of the out-of-plane and in-plane loops shows that the easy axis of magnetization is perpendicular to the sample surface. From the hysteresis loops, a saturation magnetization of $M_S = 560\,\text{emu/cm}^3$ and a coercive field of $H_C = 3.9\,\text{kOe}$ were extracted. An effective magnetic anisotropy constant of $K_{\text{eff}} = 5 \times 10^6\,\text{erg/cm}^3$ was estimated from the anisotropy field (18 kOe) assuming a coherent magnetization reversal mechanism of individual CoCrPt grains. The remanent magnetization M_R/M_S was found to be about 0.9, which might be related to the presence of a small angular distribution of the easy magnetization axis of the CoCrPt grains.

After the pre-characterization of the as-grown samples, the samples were irradiated with Co^+ ions with an energy of 40 keV at room temperature. The ion fluence was systematically increased from $0.5 \times 10^{14}\,\text{cm}^{-2}$ up to $4.5 \times 10^{14}\,\text{cm}^{-2}$. Details on the ion irradiation procedure are given elsewhere [130]. The irradiation energy of 40 keV was chosen to obtain the maximum of the damage distribution well within the magnetic layer grown on a planar substrate. However, as it will be discussed below, deposition of metal films onto particle assemblies has an important peculiarity compared to the layer stacks grown on planar substrates: due to the curvature of the particle surface, the c-axis of the columnar CoCrPt grains gets tilted following the curved surface of the spherical particles. Due to the tilt of the c-axis of the CoCrPt grains, irradiation of the layer stack grown onto particle assemblies results in an inhomogeneous modification of the magnetic properties within an individual magnetic cap.

5.4.3 Results and Discussion

5.4.3.1 Structural characterization

To get an overview of the structural properties of the samples, both SEM and TEM images were taken. Please note that this study was done on an identical layer stack but applying a different sputter pressure during the Ru layer deposition. However, the main conclusions are not expected to be affected by this modification. Figure 5.33(a) shows an SEM image of an array of particles with a size of 160 nm after film deposition. Figures 5.33(b) shows a cross-sectional TEM image of a magnetic cap on a particle with a size of 160 nm, revealing both the granular structure of the CoCrPt:SiO$_2$ layer and that columnar grains grow perpendicular to the particle surface, leading to a wide distribution of the magnetic easy axes directions over the particle surface. These columnar grains are expected to be strongly exchange decoupled (intra-cap decoupling). Moreover, since each magnetic cap only has six contact points with neighboring caps due to the hexagonal arrangement of the self-assembled particles, a strong exchange decoupling between the individual caps is expected (inter-cap decoupling). These peculiar structural properties in turn determine the distinct dependence of the magnetic properties on the size of the particles.

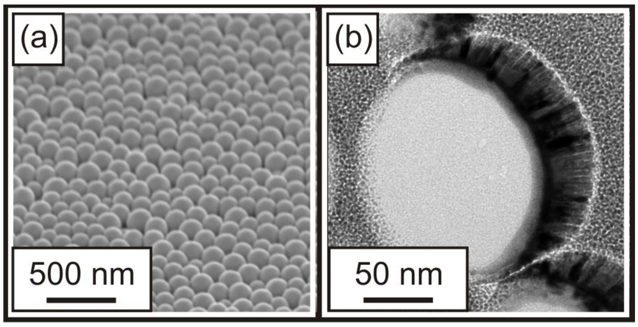

Figure 5.33: (a) SEM image of a dense array of 160 nm SiO$_2$ particles after film deposition. (b) Cross-sectional TEM image of a magnetic cap grown on a 160 nm SiO$_2$ particle. Please note that the sputter pressure of the Ru underlayer was different for this sample compared to the samples under investigation.

5.4.3.2 Magnetic characterization

Non-irradiated samples In the following, the results of the magnetic characterization of the non-irradiated CoCrPt:SiO$_2$ films grown onto assemblies of SiO$_2$ particles shall be discussed.

SQUID investigations in out-of-plane geometry (Fig. 5.34) reveal a rather broad switching field distribution (SFD). Furthermore, there is a clear size-dependence of the coercive field and remanent magnetization showing a decrease with decreasing particle size. The reduced remanent magnetization originates from the tilt of the easy axis of magnetization induced by the tilted exchange decoupled CoCrPt grains formed on the curved particle surface (Fig. 5.33(b)). The decreasing coercivity with particle size is in contrast to observations on exchange-coupled films (i.e. Co/Pd, Co/Pt multilayers) grown onto arrays of polystyrene particles [115, 116], where an increase of H$_C$ with decreasing particle size was observed. The difference is related to the different inter-cap exchange coupling compared to the CoCrPt:SiO$_2$ film caps. Whereas the entire cap of Co/Pt(Pd) multilayers reverse incoherently [119] , the switching of individual columnar grains of the CoCrPt:SiO$_2$ film caps reverse via coherent rotation of the magnetization. In this respect, the reduction of the coercive field with decreasing particle size might be attributed to a reduction of the grain size leading to a lowering of the thermal stability of the film and thus reduced coercivity. However, the curvature can also lead to a modified growth of the layer-stack with a degradation of the required texture. Both explanations are supported by the hysteresis loops measured along the hard axis direction (in-plane geometry, Fig. 5.34(b)), where a decrease of the particle size down to 10 nm results in a lowering of the saturation field from about 18 kOe to about 5 kOe.

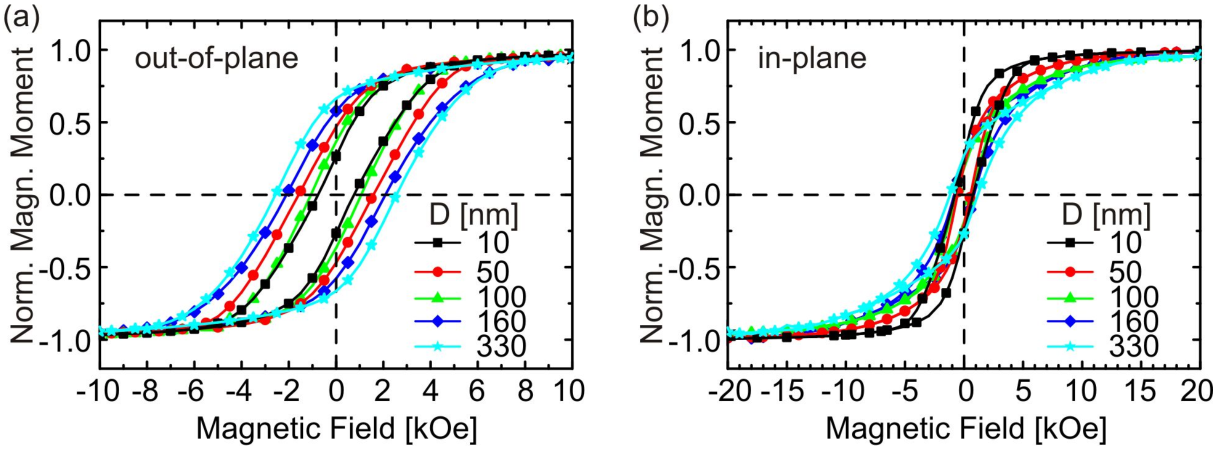

Figure 5.34: Hysteresis loops of the non-irradiated samples measured with SQUID in (a) out-of-plane and (b) in-plane geometry. Please note the different x-axis scaling.

An MFM study has been performed on the samples which were ac-demagnetized to probe the local magnetic properties (Fig. 5.35). It was observed that independent of the particle size, magnetic caps are in a magnetic multi-domain state. This is expected for an assembly of strongly exchange decoupled magnetic grains, which typically reveals a rather small equilibrium size of the magnetic domains determined by the competition between the intergranular exchange energy and magnetostatic energy.

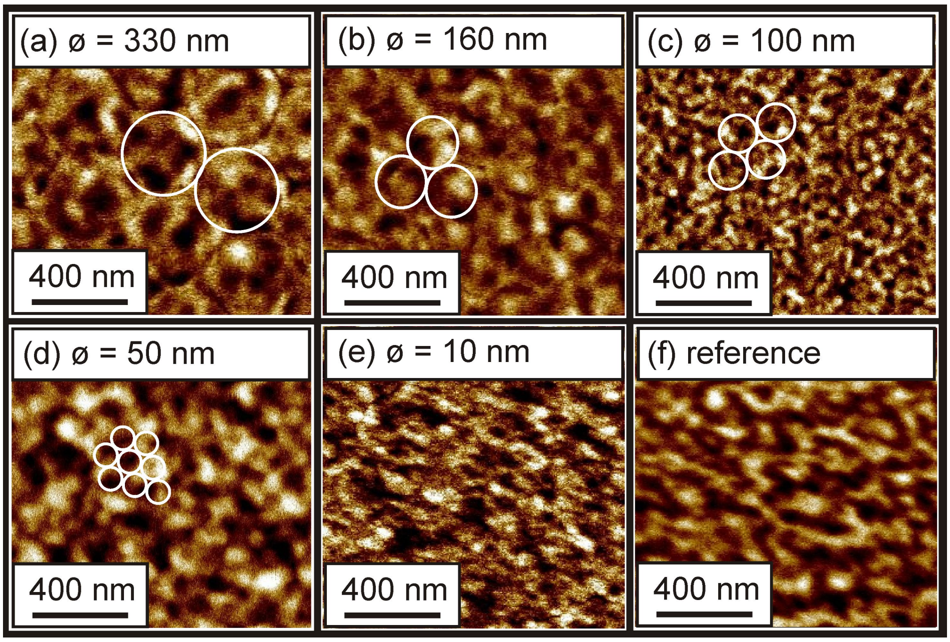

Figure 5.35: MFM images of the non-irradiated films grown on (a-e) the SiO$_2$ particles and (f) on a planar substrate. The positions of individual particles are marked exemplarily with white circles.

Co$^+$ irradiated samples After pre-characterizing the samples, Co$^+$ ion irradiation with various fluences of up to $4.5 \times 10^{14}\,\mathrm{cm}^{-2}$ was carried out. Please note that the samples were irradiated only once. Figure 5.36 shows a summary of the SQUID hysteresis loops after irradiation.

The shape of the in-plane hysteresis loops changes significantly after irradiation with Co$^+$ ions with the lowest irradiation fluence. However, a further increase of the irradiation fluence does not influence the in-plane hysteresis loops any further (compare Fig. 5.34(b) with Fig. 5.36(b, d, f)). Please note that the saturation field in hard axis direction is found to be about 18 kOe (similar to the reference sample) for all irradiation fluences. This can be explained by the exchange coupling induced by the Co$^+$ ion irradiation, leading to a vanishing influence of the curvature of the particle with different diameters confirming the assumption that the magnetic anisotropy constant was initially not altered by the grain growth on the particles with various sizes.

To further analyze the out-of-plane hysteresis loops, the coercive field and the remanent magnetization was extracted and summarized in Fig. 5.37, including also the values of the non-irradiated cap structures for comparison.

Whereas for the non-irradiated cap array, the remanent magnetization and the coercive field

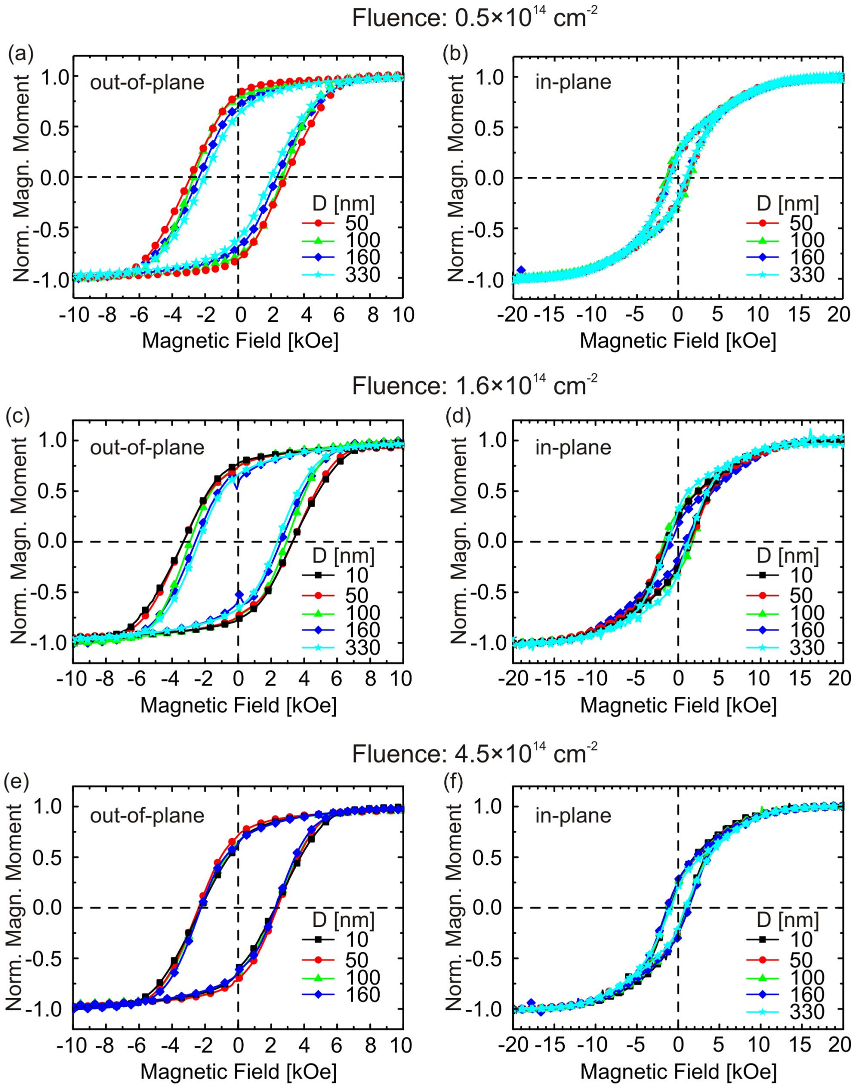

Figure 5.36: Out-of-plane and in-plane hysteresis loops of the irradiated films measured with SQUID. Please note that due to damage of the sample surface, the measurement of the sample grown onto 10 nm SiO_2 particles is missing for an irradiation fluence of $0.5 \times 10^{14}\,\mathrm{cm}^{-2}$. The same applies for the out-of-plane measurement of the 330 nm particle array after irradiation at a fluence of $4.5 \times 10^{14}\,\mathrm{cm}^{-2}$.

increase with increasing particle diameter, the opposite behavior is observed after irradiation except for the smallest particles in particular for the highest fluence (Fig. 5.37). Additionally, both H_C and M_R for the irradiated samples are found to be significantly higher than the respective values of the non-irradiated caps for the smaller particle diameters. These observations clearly indicate an increase of the intergranular exchange coupling induced by the implantation of Co into the grain boundaries [130], since the enhancement of the exchange is resulting in an enhanced thermal stability of the magnetic media which can explain the increase of the remanence magnetization and improved coercive field with the expected size dependence for an exchange coupled cap structure. Please note that even with an increasing amount of Co in the film, the

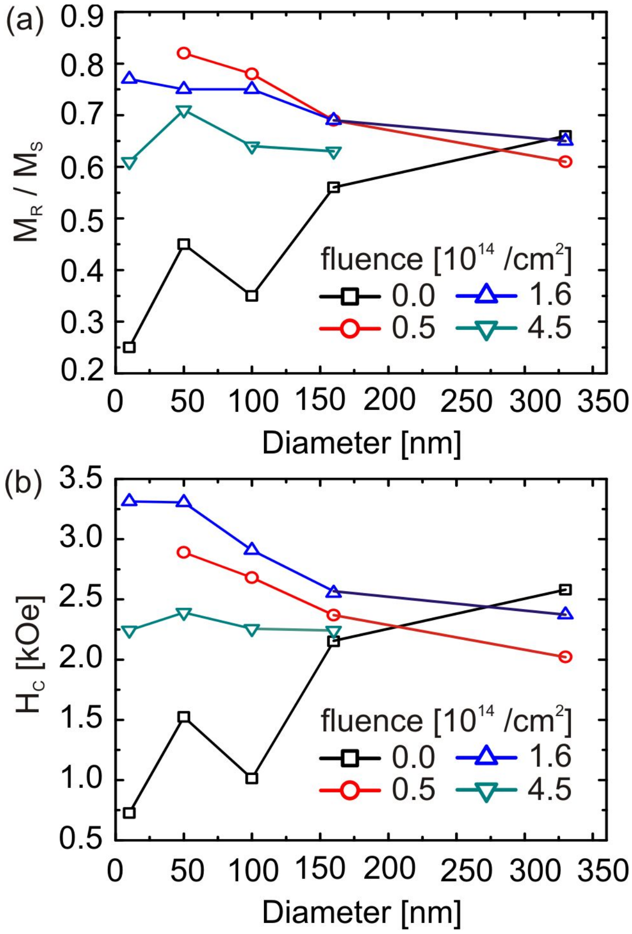

Figure 5.37: (a) Remanent magnetization and (b) coercive field of the non-irradiated and irradiated films as function of the particle diameter.

saturation magnetization changes only slightly, as the total amount of implanted Co atoms is less than 0.1%. However, by further increasing the irradiation fluence to $4.5 \times 10^{14}\,\mathrm{cm}^{-2}$, the degradation of the magnetic layer becomes dominant and both, the remanent magnetization and the coercive field in the easy-axis direction decrease but the properties remain nearly the same for all particle sizes. The underlying microstructure after irradiation was not investigated thus the mechanism which lead to the observed magnetic behavior at high fluence is not clear. One can speculate that the implantation of carbon from the top layer will lead to the observed degradation [107], however processes such as vacancy formation, disordering, or cluster formation have to be taken into account as well [127, 132].

Figure 5.38 shows MFM images of the irradiated cap arrays. As no noticeable difference in the MFM images for small irradiation fluences was observed, only the images for the highest fluence of $4.5 \times 10^{14}\,\mathrm{cm}^{-2}$ are shown. Additionally, an MFM image of the reference sample irradiated with the same fluence is presented (Fig. 5.38(f)). The images were taken after exposing the initially saturated samples to a reverse magnetic field equal to the coercive field. By comparing

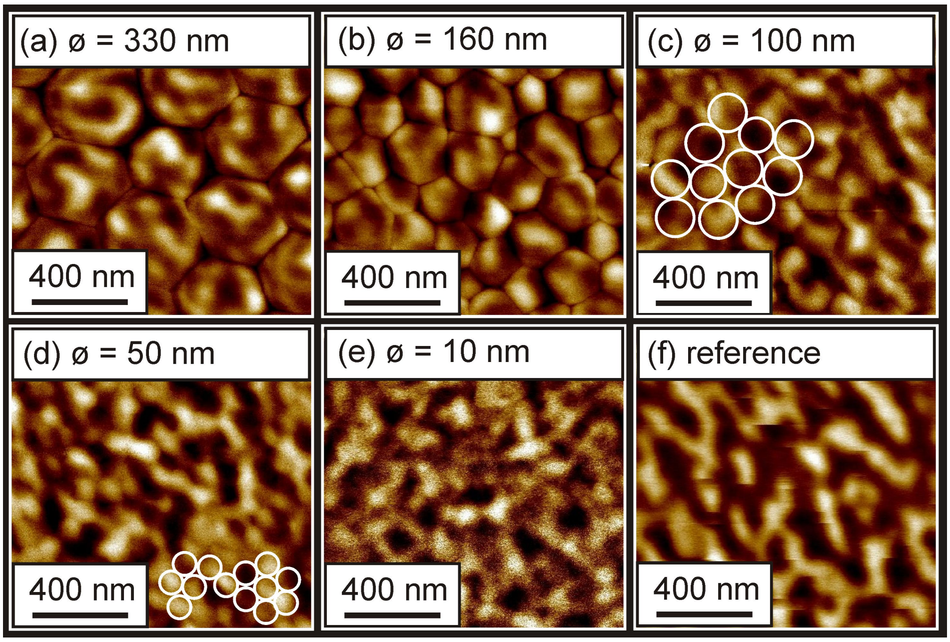

Figure 5.38: MFM images of the irradiated cap arrays after applying a negative field close to the coercivity to the initially saturated samples. The irradiation fluence was $4.5 \times 10^{14}\,\mathrm{cm}^{-2}$. The white circles represent individual particles.

Fig. 5.35 with Fig. 5.38 it appears that the characteristic magnetic domain width has somewhat increased after irradiation in particular for the 100 nm particle array, the same trend is observed for the irradiated planar CoCrPt:SiO_2 film [130]. However, all caps remain in a magnetic multi-domain state independent of the particle size.

It is worth noticing that for the 10 nm particle array the deposited film thickness is already much larger than the particle size which should result in a more continuous layer with large roughness given by the particle template. Thus, it is not surprising that the magnetic domain size for the planar film is somewhat larger and better defined than the one of the film deposited onto the 10 nm particles for the same irradiation fluence. In this case as the increase of the exchange coupling is less pronounced for the films on the particles due to the different microstructure, as discussed above, and secondly, its larger roughness leads to an increase of pinning and nucleation sites and thus to smaller domain sizes with larger coercivity.

Chapter 6

Summary

Due to the ever increasing need of data storage capacity, the amount of data that can be saved on hard disk drives has been increased nearly exponentially over the last decades. However, due to fundamental issues in the current recording technology and therefor its inability to increase the areal density of hard disc drives any further, new recording technologies and recording media designs have to be developed and evaluated concerning its possible applicability. In this thesis, both experimental and theoretical studies on current recording media and possible future recording media, namely bit patterned media, have been carried out and will be summarized shortly in the following:

The magnetization reversal process of single nanomagnets and their energy barrier of magnetization was simulated using micromagnetic simulations. A systematic study about the dependence of the energy barrier for magnetization reversal process on the geometry of one individual bit was performed. It was found out that for quasi-coherent reversal mode, the results of the energy barrier simulations agree with calculations using analytical formulas for homogenously magnetized ellipsoids. In the region where incoherent reversal behavior takes place, the volume of the bit in an analytical approach has to be replaced with an activation volume which is smaller than the physical volume of the bit. The ratio between activation volume and real volume of the bit was studied as a function of the size of the bit and a critical ratio of 0.5 was found. If the magnetization reversal process is incoherent, the ratio between activation volume and real volume of the bit drops below 0.5. Furthermore, the field-driven magnetization reversal mechanism of a single bit was investigated. It was shown that the transition from quasi-coherent to incoherent magnetization reversal process is dependent on the magnetic anisotropy constant and geometrical properties of the bit. Moreover, this transition goes ahead with a change of the energy barrier dependency on the geometrical and magnetic parameters.

Also using micromagnetic simulations, the influence of various magnetic and geometrical properties on the switching field and switching field distribution of bit patterned media. Thereby, both single-phase and exchange coupled composite bits were investigated. It was found out that for uniaxial single-phase bits, the switching field distribution increases with increasing distribution of the magnetic anisotropy constant of the bits and decreasing distance between the individual bits due to magnetostatic interaction. In the case of an easy axis perpendicular to the film plane, the optimal field angle is about 45°, going ahead with the theory developed by Stoner and Wohlfarth. In the case of an tilted easy axis, when the external magnetic field is applied perpendicular to the substrate, the influence of the tilt angle on the switching field follows a more Stoner-Wohlfarth-like angular dependence. This tendency changes totally when the external magnetic field is applied under an angle with respect to the surface normal for tilt angles larger than about 15°. The effect of the angular variation of the magnetic anisotropy orientation on the SFD becomes negligible for small tilt angles if the magnetic field is applied under an angle close to 45°. Larger tilts result in an increase of both averaged switching field and switching field distribution. In the case of exchange coupled composite bits, a decrease of the switching field and switching field distribution was observed if a large number of layers were used. Moreover, it was found out that the energy barrier of magnetization reversal depends mostly on the highest anisotropy constant of the layer stack and is mainly not influenced by softer layers. Moreover, exchange-coupled composite bit patterned media arrays were invastigated using micromagnetic simulations. A narrowing of SFD/H_S and a reduction of H_S was obtained using a graded BPM media consisting of ten magnetic layers with a quadratically decreasing magnetic anisotropy value. However, the energy barrier for magnetization reversal of an individual bit at a fixed layer thickness is not altered and guarantees its thermal stability. In this context, a possible influence of the correlation of the distributions of the magnetic anisotropy constant was investigated in a system consisting of two exchange-coupled layers. It was shown that a correlation between the magnetic anisotropy distributions of the different layers of an ECC bit patterned array has a severe influence on the switching field distribution. In the case of nearly equal distributions of the soft and hard layer, the normalized switching field distribution can be decreased significantly by choosing an intermediate correlation between the individual distributions, depending on the specific way of defining the correlation. However, in general, for different distributions of the magnetic anisotropy value of the different layers, a correlation is only favorable if the soft layer has a larger relative distribution than the hard layer and not vice versa.

The magnetization reversal behavior of a dot array consisting of Co/Pt multilayers with perpendicular magnetic anisotropy, patterned by electron beam lithography, was investigated. The size of the dots was varied from 200 nm down to 40 nm while keeping the filling factor constant at about 0.16. It was found that the shape of the individual dots changes with dot size. Whereas dots larger than 120 nm are rectangular, smaller dots have a more round shape. The MFM study revealed that dots with a size of 200 nm are in a multi-domain state and reverse their magnetization via domain wall nucleation and propagation, while the smallest dots with a size of 40 nm were only found in a single-domain state. The MOKE investigations have shown a severe impact of the patterning process, resulting in a degradation of the magnetic layer, leading to a decrease of the switching field and increase of the switching field distribution of the dot array with decreasing dot size. Finally, micromagnetic simulations were performed to understand the magnetization reversal process in more detail, revealing the transition from single-domain coherent magnetization rotation over incoherent magnetization reversal to domain wall nucleation and propagation with increasing dot size from 10 nm to 200 nm.

In the last part of the thesis, a study of the magnetic and structural properties of strongly exchange decoupled CoCrPt:SiO_2 films grown onto assemblies of SiO_2 spherical particles was presented. The magnetic properties of the samples were found to be substantially different compared to the films grown on planar SiO_2 substrates. The observed difference was discussed in terms of the angular distribution of the easy axis following the curved surface of the spherical particles. The samples reveal an intriguing scaling dependence of the coercive field and remanent magnetization: both parameters are found to decrease with decreasing diameter of the particles. Furthermore, the possibility to tune the magnetic properties using ion irradiation with magnetic Co+ ions at fluences up to $4.5 \times 10^{14}\text{cm}^{-2}$ was discussed. The irradiation process at $0.5 \times 10^{14}\text{cm}^{-2}$ already results in an opposite scaling behavior: H_C increases with decreasing particle size down to 10nm. Moreover, the increase of the exchange coupling results in a substantial increase of the remanent magnetization. It was assumed that the different scaling behavior is due to the enhancement of the intergranular exchange coupling between CoCrPt grains initiated by Co^+ irradiation resulting in an enhanced thermal stability of the magnetic media. However, after irradiation with larger fluences of $4.5 \times 10^{14}\text{cm}^{-2}$, the degradation of the magnetic layer becomes dominant and both, the remanent magnetization and the coercive field in the easy-axis direction decrease but do not show a pronounced dependence on the particle size. Moreover, a detailed MFM study of both, the non-irradiated and irradiated caps showed multi-domain states for all particles sizes with a somewhat larger magnetic domain size.

Chapter 7

Outlook

In the following, a short overview over some still unanswered questions and how they might be investigated shall be given.

Concerning the magnetization reversal processes of single nanomagnets, experimental proof of the obtained results is of high importance. Therefore, time-resolved magneto-optical Kerr effect experiments are currently performed in cooperation with H. Schmidt from the University of California, Santa Cruz. In these experiments, the spin dynamics, i.e. the precession of the spins around their effective field is measured. By analysing these data, it is possible to distinguish between coherent and incoherent rotation of magnetization, giving insight into the magnetic behaviour of single nanostructures. Moreover, the same experiments might get applied to nanostructure arrays, revealing information about the magnetostatic interaction between the individual bits and their influence on the magnetization dynamics.

Regarding the micromagnetic simulations of bit patterned media, the main goalhas to be to find a way to simulate bits closer to the experimental reality. This can include several aspects:

- surface roughness and roughness of the individual layers of one bit
- bits consisting out of several grains reflecting the way the magnetic material grows in the experiment
- including distributions not only of the magnetic anisotropy constant but also of the saturation magnetization and the easy axis within one bit
- including a possible size and thickness distribution of the individual bits
- changing the shape of the bits corresponding to their size, i.e. more round bits if they are very small and more rectangular like if they are larger

Combining several or all of these points might lead to results being in better agreement with experiments.

Bibliography

[1] IBM Research and Development Laboratory, “Proposal - Random Access File,” 1953.

[2] IBM, “US Patent 3,503,060,” 1970.

[3] Magnetic disc heritage center, “Ramac history,” 2005.

[4] IBM, “Areal density roadmap.”

[5] Veeco, “Areal density roadmap.”

[6] S. Greaves, Y. Kanai, and H. Muraoka, “Shingled magnetic recording on bit patterned media,” *IEEE Trans. Magn.*, vol. 46, no. 6, p. 1460, 2010.

[7] A. Moser, K. takano, D. T. Margulies, M. Albrecht, Y. Sonobe, Y. Ikeda, S. Sun, and E. E. Fullerton, “Magnetic recording: advancing into the future,” *J. Phys. D: Appl. Phys.*, vol. 35, pp. R157–R167, 2002.

[8] C. Ross, “Patterned Magnetic Recording Media,” *Annu. Rec. Mater. Res.*, vol. 31, pp. 203–235, 2001.

[9] B. D. Terris, “Fabrication challenges for patterned recording media,” *J. Magn. Magn. Mat.*, vol. 321, no. 6, pp. 512–517, 2009.

[10] S. Batra, J. D. Hannay, Z. Hong, and J. S. Goldberg, “Investigations of perpendicular write head design for 1 TB/in^2,” *IEEE Trans. Magn.*, vol. 40, p. 319, 2004.

[11] J. Zhu and Y. Tang, “Micromagnetics of Percolated Perpendicular Media,” *IEEE Trans. Magn.*, vol. 43, pp. 687–692, 2007.

[12] K. Matsumoto, A. Inomata, and S. ya Hasegawa, “Thermally Assisted Magnetic Recording,” *FUJITSU Sci. Tech. J.*, vol. 42, no. 1, pp. 158–167, 2006.

[13] H. J. Richter, A. Y. Dobin, R. T. Lynch, D. Weller, R. M. Brockie, O. Heinonen, K. Z. Gao, J. Xue, R. J. M. d. Veerdonk, P. Asselin, and M. F. Erden, “Recording potential of bit-patterned media,” *Appl. Phys. Lett.*, vol. 88, p. 222512, 2006.

[14] J.-G. Zhu and Y. Tan, “A medium microstructure for high area density perpendicular recording,” *J. Appl. Phys*, vol. 99, p. 08Q903, 2006.

[15] D. E. Laughlin, Y. Peng, Y.-L. Qin, M. Lin, and J.-G. Zhu, “Fabrication, Microstructure, Magnetic, and Recording Properties of Percolated Perpendicular Media,” *IEEE Trans. Magn.*, vol. 43, pp. 693 – 697, 2007.

[16] O. Hellwig, A. Berger, J. B. Kortright, and E. E. Fullerton, “Domain structure and magnetization reversal of antiferromagnetically coupled perpendicular anisotropy films,” *J. Magn. Magn. Mater.*, vol. 319, p. 13, 2007.

[17] D. Suess, “Multilayer exchange spring media for magnetic recording,” *Appl. Phys. Lett.*, vol. 89, p. 113105, 2006.

[18] D. Suess, J. Lee, J. Fidler, and T. Schrefl, “Exchange-coupled perpendicular media,” *J. Magn. Magn. Mater.*, vol. 321, pp. 545–554, 2009.

[19] R. H. Victora and S. Xiao, “Composite media for perpendicular magnetic recording,” *IEEE Trans. Magn.*, vol. 41, pp. 537–542, 2005.

[20] D. Suess, T. Schrefl, S. Fähler, M. Kirschner, G. Hrkac, F. Dorfbauer, and J. Fidler, “Exchange spring media for perpendicular recording,” *Appl. Phys. Lett.*, vol. 87, p. 012504, 2005.

[21] D. Suess, J. F. andK. Porath, T. Schrefl, and D. Weller, “Micromagnetic study of pinning behavior in percolated media,” *J. Appl. Phys.*, vol. 99, p. 08G905, 2006.

[22] M. T. Rahman, L. Chih-Huang, D. Vokoun, and N. N. Shams, “A Simple Route to Fabricate Percolated Perpendicular Magnetic Recording Media,” *IEEE Trans. Magn.*, vol. 43, pp. 2133 – 2135, 2007.

[23] D. Makarov, E. B. Urena, O. G. Schmidt, F. Liscio, M. Maret, C. Brombacher, S. Schulze, M. Hietschold, and M. Albrecht, “Nanopatterned copt alloys with perpendicular magnetic anisotropy,” *Appl. Phys. Lett.*, vol. 93, no. 15, p. 153112, 2008.

[24] D. Makarov, P. Krone, D. Lantiat, C. Schulze, A. Liebig, C. Brombacher, M. Hietschold, S. Hermann, C. Laberty, D. Grosso, and M. Albrecht, “Magnetization Reversal in Arrays of Magnetic Nanoperforations,” *IEEE Trans. Magn.*, vol. 45, p. 3515, 2009.

[25] C. Brombacher, M. Saitner, C. Pfahler, A. Plettl, P. Ziemann, D. Makarov, D. Assmann, M. H. Siekman, L. Abelmann, and M. Albrecht, “Tailoring particle arrays by isotropic plasma etching: an approach towards percolated perpendicular media,” *Nanotechnology*, vol. 20, no. 10, p. 105304, 2009.

[26] C. Schulze, M. Faustini, J. Lee, H. Schletter, M. U. Lutz, P. Krone, M. Gass, K. Sader, A. L. Bleloch, M. Hietschold, M. Fuger, D. Suess, J. Fidler, U. Wolff, V. Neu, D. Grosso,

D. Makarov, and M. Albrecht, “Magnetic films on nanoperforated templates: A route towards percolated perpendicular media,” *Nanotechnology*, vol. 21, p. 495701, 2010.

[27] D. Punz, J. Lee, M. Fuger, J. Fidler, T. Schrefl, , and D. Suess, “Theory and micromagnetics of pinning mechanism at cylindrical defects in perpendicular magnetic films,” *J. Appl. Phys.*, vol. 107, p. 113926, 2010.

[28] B. D. Terris and T. Thomson, “Nanofabricated and self-assembled magnetic structures as data storage media,” *J. Phys. D: Appl. Phys.*, vol. 38, no. 12, p. R199, 2005.

[29] D. Weller, H. Braendle, G. Gorman, C. Lin, and H. Notarys, “Magnetic and magneto-optical properties of cobalt-platinum alloys with perpendicular magnetic anisotropy,” *Appl. Phys. Lett.*, vol. 61, p. 2726, 1992.

[30] T. Thomas, G. Hu, and B. D. Terris, “Intrinsic Distribution of Magnetic Anisotropy in Thin Films Probed by Patterned Nanostructures,” *Phys. Rev. Lett.*, vol. 96, p. 257204, 2006.

[31] M. Albrecht, C. T. Rettner, A. Moser, M. E. Best, and B. D. Terris, “Recording performance of high-density patterned perpendicular magnetic media,” *Appl. Phys. Lett.*, vol. 81, p. 2875, 2002.

[32] J. Lohau, A. Moser, C. T. Rettner, M. E. Best, and B. D. Terris, “Writing and reading perpendicular magnetic recording media patterned by a focused ion beam,” *Appl. Phys. Lett.*, vol. 78, p. 990, 2001.

[33] S. Y. Chou, “Patterned magnetic nanostructures and quantized magnetic disks,” *Proc. IEEE*, vol. 85, p. 652, 1997.

[34] R. P. Cowburn, “Property variation with shape in magnetic nanoelements,” *J. Phys. D: Appl. Phys.*, vol. 33, p. R1, 2000.

[35] S. Evoy, D. W. Carr, L. Sekaric, Y. Sozuki, J. M. Parpia, and H. C. Craighead, “Thickness dependent binary behavior of elongated single-domain cobalt nanostructures,” *J. Appl. Phys.*, vol. 87, p. 404, 2000.

[36] T. A. Savas, M. Farhoud, H. I. Smith, M. Hwang, and C. A. Ross, “Properties of large-area nanomagnet arrays with 100 nm period made by interferometric lithography,” *J. Appl. Phys.*, vol. 85, p. 6160, 1999.

[37] W. Wu, B. Cui, X. Sun, W. Zhang, L. Zhuang, L. Kong, and S. Chou, “Large area high density quantized magnetic disks fabricated using nanoimprint lithography,” *J. Vac. Sci. Technol. B*, vol. 16, p. 3825, 1998.

[38] S. Sun and C. B. Murray, "Synthesis of monodisperse cobalt nanocrystals and their assembly into magnetic superlattices," *J. Appl. Phys.*, vol. 85, p. 4325, 1999.

[39] O. Hellwig, J. K. Bosworth, E. Dobisz, D. Kercher, T. hauet, G. Zeltzer, J. D. Risner-Jamtgaard, D. Yaney, and R. Ruiz, "Bit patterned media based on block copolymer directed assembly with narrow magnetic switching field distribution," *Appl. Phys. Lett.*, vol. 96, p. 052511, 2010.

[40] R. H. Victora and X. Shen, "Exchange coupled composite media," *Proc. IEEE*, vol. 96, p. 1799, 2008.

[41] F. Garcia-Sanchez, O. Chubykalo-Fesenko, O. Mryasov, R. W. Chantrell, and K. Y. Guslienko, "Exchange spring structures and coercivity reduction in fept/ferh bilayers: A comparison of multiscale and micromagnetic calculations," *Appl. Phys. Lett.*, vol. 87, p. 122501, 2005.

[42] S. Hernandez, M. Kapoor, and R. H. Victora, "Synthetic antiferromagnet for hard layer of exchange coupled composite media," *Appl. Phys. Lett.*, vol. 90, p. 132505, 2007.

[43] N. F. Supper, D. T. Margulies, A. Moser, A. Berger, H. Do, and E. E. Fullerton, "Writability enhancement using exchange spring media," *IEEE Trans. Magn.*, vol. 41, p. 3238, 2005.

[44] N. F. Supper, D. T. Margulies, A. Moser, A. Berger, H. Do, and E. E. Fullerton, "Experimental study of longitudinal exchange spring media," *J. Appl. Phys.*, vol. 99, p. 08S310, 2006.

[45] W. K. Shen, J. M. Bai, R. H. Victora, J. H. Judy, and J. P. Wang, "Composite perpendicular magnetic recording media using $[\mathrm{Co/PdSi}]_n$ as a hard layer and FeSiO as a soft layer," *J. Appl. Phys.*, vol. 97, p. 10N513, 2005.

[46] J. P. Wang, W. K. Shen, and J. Bai, "Exchange coupled composite media for perpendicular magnetic recording," *IEEE Trans. Magn.*, vol. 41, p. 3181, 2005.

[47] O. Hellwig, J. B. Kortright, K. Takano, and E. E. Fullerton, "Switching behavior of fept/ni-fe exchange-spring films studied by resonant soft-x-ray magneto-optical kerr effect," *Phys. Rev. B*, vol. 62, p. 11694, 2000.

[48] B. C. Stipe, T. C. Strang, C. C. Poon, H. Balamane, T. D. Boone, J. A. Katine, J. Li, V. Rawat, H. Nemoto, A. Hirotsune, O. Hellwig, R. Ruiz, E. Dobisz, D. S. Kercher, N. Robertson, T. R. Albrecht, and B. C. Terris, "Magnetic recording at 1.5 pb/m^2 using an integrated plasmonic antenna," *Nature Photonics*, May 2010.

[49] J. W. F. Brown, "Theory of Approach to magnetic saturation," *Phys. Rev.*, vol. 58, pp. 736–743, 1940.

[50] H. Kronmüller and M. Fähnle, *Micromagnetism and the Microstructure of Ferromagnetic Solids*. Cambridge University Press, 2009.

[51] A. Aharoni, “Magnetostatic energy calculation,” *IEEE Trans. Magn.*, vol. 27, no. 4, pp. 3539–3547, 1991.

[52] Q. Chen and A. Konrad, “A review of finite element boundary techniqes for static and quasi-static electromagnetic field problems,” *IEEE Trans. Magn.*, vol. 33, pp. 664–676, 1996.

[53] W. Scholz, “Micromagnetic simulation of thermally activated switching in fine particles,” Master’s thesis, Technical University of Vienna, 1999.

[54] R. M. White, *Quantum Theory of Magnetism: Magnetic Properties of Materials*. Springer, 2007.

[55] T. R. Koehler and D. R. Fredkin, “Finite element methods for micromagnetics,” *IEEE Trans. Magn.*, vol. 28, pp. 1239–1244, 1992.

[56] D. R. Fredkin and T. R. Koehler, “Hybrid method for computing demagnetizing fields,” *IEEE Trans. Magn.*, vol. 26, no. 2, pp. 415–417, 1990.

[57] T. R. Koehler, “Hybrid FEM-BEM method for fast micromagnetic calculations,” *Physica B: Condensed Matter*, vol. 223, no. 4, pp. 302–307, 1997.

[58] W. Scholz, *Scalable Parallel Micromagnetic Solvers for Magnetic Nanostructures*. PhD thesis, University of Vienna, 2003.

[59] T. Schrefl, G. Hrkac, S. Bance, D. Suess, O. Ertl, and J. Fidler, *Handbook of Magnetism*, vol. 2. Wiley, 2007.

[60] W. Gawehn, *Finite Elemente Methode: FEM-Grundlagen zur Statik und Dynamik*, vol. 2. Books on Demand, 2009.

[61] I. C. for Numerical Methods in Engineering. URL, 2009. [Online; accessed 12.04.2010].

[62] Y. Kawada, Y. Ueno, and K. Shibata, “Co-Pt Multilayers Perpendicular Magnetic Recording Media With Thin Pt Layer and High Perpendicular Anisotropy,” *IEEE Trans. Magn.*, vol. 38, no. 5, p. 2045, 2002.

[63] D. Weller, A. Moser, L. Folks, M. E. Best, M. W. L. Toney, M. Schwickert, J.-U. Thiele, and M. F. Doerner, “High K_U materials approach to 100 Gbits/inch^2,” *IEEE Trans. Magn.*, vol. 36, pp. 10–15, 2000.

[64] W. Tang, A. M. Gabay, Y. Zhang, G. C. Hadjipanayis, and H. Kronmüller, "Temperature dependence of coercivity and magnetization reversal mechanism in Sm(Co/Fe/Cu/Zr) magnets," *IEEE Trans. Magn.*, vol. 47, pp. 2515–2517, 2001.

[65] B. Lu, D. Weller, A. Sunder, G. Ju, X. Wu, R. Brockie, T. Nolan, C. Brucker, and R. Ranjan, "High anisotropy cocrpt(b) media for perpendicular magnetic recording," *Journal of Applied Physics*, vol. 93, no. 10, pp. 6751–6753, 2003.

[66] T. Schrefl and D. Suess, *Femme: Finite Element Micromagnetics.* University of Vienna, St. Pölten University of Applied Science, 2009.

[67] S. Benson and J. J. More, "A limited memory variable metric method for bound constrained minimization," anl-95/11 - revision 2.1.3, Argonne National Laboratory, 2002.

[68] L. Berger, "Emission of spin waves by a magnetic multilayer traversed by a current," *Phys. Rev. B*, vol. 54, no. 13, pp. 9353–9358, 1996.

[69] K. Capelle and B. L. Gyorffy, "Exploring dynamical magnetism with time-dependent density-functional theory: From spin fluctuations to gilbert damping," *Europhys. Lett.*, vol. 61, no. 3, pp. 354–360, 2003.

[70] L. Landau and E. M. Lifshitz, "Collected Papers of L. D. Landau," *Phys. Z. Sowjet.*, vol. 8, p. 135, 1935.

[71] T. L. Gilbert. PhD thesis, Illinois Institute of Technology, 1956. unpublished.

[72] R. C. O'Handley, *Modern Magnetic Materials: Principles and Applications.* Wiley-Interscience, 2000.

[73] P. Krone, D. Makarov, A. Cattoni, G. Faini, A.-M. Haghiri-Gosnet, I. Knittel, U. Hartmann, T. Schrefl, and M. Albrecht, "Investigation on the magnetization reversal of a magnetic dot array of co/pt multilayers," *J. Nanoparticle Research*, 2010. accepted. doi: 10.1007/s11051-010-0123-z.

[74] H. Braun and H. N. Bertram, "Nonuniform switching of single domain particles at finite temperatures," *J. Appl. Phys.*, vol. 75, no. 9, p. 4609, 1994.

[75] E. Kondorski, "On the nature of coercive force and irreversible changes in magnetisation," *Phys. Z. Sowjet.*, vol. 11, p. 597, 1937.

[76] D. Weller and A. Moser, "Thermal effect limits in ultrahigh-density magnetic recording," *IEEE Trans. Magn.*, vol. 35, no. 6, pp. 4423–4439, 1999.

[77] G. Henkelmann and H. Jonsson, “Improved tangent estimate in the nudged elastic band method for finding minimum energy paths and saddle points,” *J. Chem. Phys.*, vol. 113, pp. 9978–9985, 2000.

[78] J. Kästner. URL, 2010. [Online; accessed 12.04.2010].

[79] C. Brombacher, “Herstellung und Untersuchung von magnetischen Schichtsystemen auf sphärischen Nanopartikeln,” Master’s thesis, University of Konstanz, 2007.

[80] F. Burmeister, W. Badowsky, T. Braun, S. Wieprich, J. Boneberg, and P. Leiderer, “Colloid monolayer lithography - a flexible approach for nanostructuring of surfaces,” *Applied Surface Science*, vol. 144, p. 461, 1999.

[81] C. Enss and S. Hunklinger, *Tieftemperaturphysik.* Springer Verlag Berlin Heidelberg, 2000.

[82] Quantum Design, *MPMS ®SQUID VSM Brochure*, 2010.

[83] T. Huhne, *Magneto-optical Kerr Effect of Multilayer and Surface Layer Systems.* Shaker Verlag GMBH, 2001.

[84] T. Ulbrich, *Co/Pd- und Co/Pt- Schichtsysteme auf Partikelmonolagen.* PhD thesis, Universoty of Konstanz, 2007.

[85] T. Ulbrich, “Aufbau eines moke-systems zur untersuchung magnetischer nanostrukturen,” Master’s thesis, University of Konstanz, 2003.

[86] J. F. Ziegler, *Handbook and Implantation Technology.* North Holland, 1 ed., 1992.

[87] J. F. Ziegler, J. P. Biersack, and U. Littmark, *The stopping and range of ions in solids.* Pergamon, 1985.

[88] K. Lenz, “private communications.”

[89] J. S. Williams, *Ion Implantation and Beam Processing.* Academic Press, 1984.

[90] P. Krone, D. Makarov, M. Albrecht, T. Schrefl, and D. Suess, “Magnetization reversal processes of single nanomagnets and their energy barrier,” *J. Magn. Magn. Mat.*, vol. 322, pp. 3771–3776, 2010.

[91] R. Dittrich, T. Schrefl, D. Suess, W. Scholz, H. Forster, and J. Fiedler, “A path method for finding energy barriers and minimum energy paths in complex micromagnetic systems,” *J. Magn. Magn. Mater.*, vol. 250, p. 12, 2002.

[92] T. Schrefl, M. E. Schabes, D. Suess, O. Ertl, M. Kirschner, F. Dorfbauer, G. Hrkac, and J. Fidler, “Partitioning of the perpendicular write field into head and sul contributions,” *IEEE Trans. Magn.*, vol. 41, p. 3064, 2005.

[93] R. F. C. Farrow, D. Weller, R. F. Marks, M. F. Toney, A. Cebollada, and G. R. Harp, “Control of the axis of chemical ordering and magnetic anisotropy in epitaxial fept films,” *J. Appl. Phys.*, vol. 79, p. 5967, 1996.

[94] W. Rave, K. Fabian, and A. Hubert, “Magnetic states of small cubic particles with uniaxial anisotropy,” *J. Magn. Magn. Mater.*, vol. 190, pp. 332–348, 1998.

[95] H. Kronmueller and M. Faehnle, *Micromagnetism and the Microstructure of Ferromagnetic Solics.* Cambridge Press, 2003.

[96] P. Krone, D. Makarov, T. Schrefl, and M. Albrecht, “Effect of the Anisotropy Distribution on the Coercive Field and Switching Field Distribution of Bit Patterned Media,” *J. Appl. Phys.*, vol. 106, p. 103913, 2009.

[97] P. Krone, D. Makarov, M. Albrecht, and T. Schrefl, “Magnetization reversal of bit patterned media: Role of the angular orientation of the magnetic anisotropy axes,” *J. Appl. Phys.*, vol. 108, p. 013906, 2010.

[98] P. Krone, D. Makarov, T. Schrefl, and M. Albrecht, “Exchange coupled composite bit patterned media,” *Appl. Phys. Lett.*, vol. 97, p. 082501, 2010.

[99] H. Kronmüller, K. D. Durst, and G. Martinek, “Angular dependence of the coercive field in sintered $Fe_{77}Nd_{15}B_8$ magnets,” *J. Magn. Magn. Mater.*, vol. 69, p. 149, 1987.

[100] M. E. Schabes, “Micromagnetic theory of non-uniform magnetization processes in magnetic recording particles,” *J. Magn. Magn. Mater.*, vol. 95, p. 249, 1991.

[101] S. Basu, P. W. Fry, M. R. J. Gibbs, T. Schrefl, and D. A. Allwood, “Control of the switching behavior of ferromagnetic nanowires using magnetostatic interactions,” *J. Appl. Phys.*, vol. 105, p. 083901, 2009.

[102] J. P. wang, Y. Y. Zou, C. H. Hee, T. C. Chong, and Y. F. Zheng, “Approaches to tilted magnetic recording for extremely high areal density,” *IEEE Trans. Magn.*, vol. 39, p. 1930, 2003.

[103] K. Z. Gao and H. N. Bertram, “Magnetic recording configuration for densities beyond 1 Tb/in^2 and data rates beyond 1 Gb/s,” *IEEE Trans. Magn.*, vol. 38, p. 3675, 2002.

[104] M. E. Schabes and H. N. Bertram, “Magnetization processes in ferromagnetic cubes,” *J. Appl. Phys.*, vol. 64, p. 1347, 1988.

[105] D. Suess, “TU-Physiker verdreifacht Kapazität von Festplattenspeicher .” URL, 2007.

[106] D. Makarov, J. Lee, C. Brombacher, C. Schubert, M. Fuger, D. Suess, J. Fidler, and M. Albrecht, “Perpendicular fept-based exchange-coupled composite media,” *Appl. Phys. Lett.*, vol. 96, p. 062501, 2010.

[107] C. T. Rettner, S. Anders, R. Thomson, M. Albrecht, Y. Ikeda, M. W. Best, and B. D. Terris, “Magnetic characterization and recording properties of patterned $\text{co}_70\text{cr}_18\text{pt}_12$ perpendicular media,” *IEEE Trans. Magn.*, vol. 38, no. 4, p. 1725, 2002.

[108] A. Aharoni, “Angular dependence of nucleation by curling in a prolate spheroid,” *J. Appl. Phys.*, vol. 82, p. 1281, 1997.

[109] E. H. Frei, S. Shtrikman, and D. Treves, “Critical size and nucleation field of ideal ferromagnetic particles,” *Phys. Rev.*, vol. 106, p. 446, 1957.

[110] Y. Ishii, “Magnetization curling in an infinite cylinder with a uniaxial magnetocrystalline anisotropy,” *J. Appl. Phys.*, vol. 70, p. 3765, 1991.

[111] D. Makarov, S. Tibus, C. T. Rettner, T. Thomson, B. D. Terris, T. Schrefl, and M. Albrecht, “Magnetic strip patterns induced by focused ion beam irradiation,” *J. Appl. Phys.*, vol. 103, p. 063915, 2008.

[112] E. C. Stoner, “A mechanism of magnetic hysteresis in heterogeneous alloys,” *Trans. R. Soc.*, vol. A240, p. 599, 1948.

[113] P. Krone, C. Brombacher, D. Makarov, K. Lenz, D. Ball, F. Springer, H. Rohrmann, J. Fassbender, and M. Albrecht, “Nanocap arrays of granular cocrpt:sio_2 films on silica particles: Tailoring of the magnetic properties by co^+ irradiation,” *Nanotechnology*, vol. 21, p. 385703, 2010.

[114] C. T. Retter, S. Anders, J. E. E. Baglin, T. Thomson, and B. D. Terris, “Characterization of the magnetic modification of co/pt multilayer films by he^+, ar^+, and ga^+ ion irradiation,” *Appl. Phys. Lett.*, vol. 80, no. 2, p. 279, 2002.

[115] M. Albrecht, G. Hu, I. L. Guhr, T. C. Ulbrich, J. Boneberg, P. Leiderer, and G. Schatz, “Magnetic multilayers on nanospheres,” *Nat. Mater.*, vol. 4, no. 3, p. 203, 2005.

[116] T. C. Ulbrich, D. makarov, G. Hu, I. L. Guhr, D. Suess, T. Schrefl, and M. Albrecht, “Magnetization reversal in a novel gradient nanomaterial,” *Phys. Rev. Lett.*, vol. 96, no. 7, p. 077202, 2006.

[117] D. Makarov, E. Bermúdez-Ureña, O. G. Schmidt, F. Liscio, M. Maret, C. Brombacher, S. Schulze, M. H. M, and M. Albrecht, “Nanopatterned copt alloys with perpendicular magnetic anisotropy,” *Appl. Phys. Lett.*, vol. 93, no. 15, p. 153112, 2008.

[118] T. C. Ulbrich, D. Assmann, and M. Albrecht, "Magnetic properties of co/pt multilayers on self-assembled particle arrays," *J. Appl. Phys.*, vol. 104, no. 8, p. 084311, 2008.

[119] T. C. Ulbrich, C. Bran, D. Makarov, O. Hellwig, J. D. Risner-Jamtgaard, D. Yaney, H. Rohrmann, V. Neu, and M. Albrecht, "Effect of magnetic coupling on the magnetization reversal in arrays of magnetic nanocaps," *Phys. Rev. B*, vol. 81, no. 5, p. 054421, 2010.

[120] C. M. Günther, O. Hellwig, A. Menzel, B. Pfau, F. Radu, D. Makarov, M. Albrecht, A. Goncharov, T. Schrefl, W. F. Schlotter, R. Rick, J. Lüning, and S. Eisebitt, "Microscopic reversal behavior of magnetically capped nanospheres," *Phys. Rev. B*, vol. 81, no. 6, p. 064411, 2010.

[121] P. Kappenberger, F. Luo, L. J. Heyderman, H. H. Solak, C. Padeste, C. Brombacher, D. Makarov, T. V. Ashworth, L. Philippe, H. J. Hug, and M. Albrecht, "Template-directed self-assembled magnetic nanostructures for probe recording," *Appl. Phys. Lett.*, vol. 95, no. 2, p. 023116, 2009.

[122] Y. Xu, J. P. Wang, Z. S. Shan, H. Jiang, Y. Su, C. T. Chong, and L. Lu, "Structural and magnetic properties of hcp-cocrpt-sio$_2$ granular media," *J. Magn. Magn. Mater.*, vol. 225, no. 3, p. 359, 2001.

[123] D. Vokoun, C. H. Lai, M. S. Lin, and R. Jiang, "Effect of deposition pressure on switching field distribution of coptcr:sio perpendicular magnetic recording thin film media," *IEEE Trans. Magn.*, vol. 42, no. 10, p. 2396, 2006.

[124] Y. Hirayama, I. Tamai, I. Takekuma, and R. Nakatani, "Role of underlayer for segregated structure formation of cocrpt-sio$_2$ granular thin film," *J. Phys.: Conf. Ser.*, vol. 165, p. 012033, 2009.

[125] C. Chappert, H. Bernas, J. Ferré, V. Kottler, J.-P. Jamet, Y. Chen, E. Cambril, T. Devolder, F. Rousseaux, V. Mathet, and H. Launois, "Planar patterned magnetic media obtained by ion irradiation," *Science*, vol. 280, no. 5371, p. 1919, 1998.

[126] H. Bernas, J. P. Attane, K. H. Heinig, D. Halley, D. Ravelosona, A. Marty, P. Auric, C. Chappert, and Y. Samson, "Ordering intermetallic alloys by ion irradiation: A way to tailor magnetic media," *Phys. Rev. Lett.*, vol. 91, no. 7, p. 077203, 2003.

[127] J. Fassbender, D. Ravelosona, and Y. Samson, "Tailoring magnetism by light-ion irradiation," *J. Phys. D: Appl. Phys.*, vol. 37, no. 16, p. R179, 2004.

[128] B. D. Terris, M. Albrecht, G. Hu, T. Thomson, and C. T. Rettner, "Recording and reversal properties of nanofabricated magnetic islands," *IEEE Trans. Magn.*, vol. 41, no. 10, p. 2822, 2005.

[129] D. Makarov, S. Tibus, C. T. Rettner, T. Thomson, B. D. Terris, T. Schrefl, and M. Albrecht, “Magnetic strip patterns induced by focused ion beam irradiation,” *J. Appl. Phys.*, vol. 103, no. 6, p. 063915, 2008.

[130] S. Tibus, T. Strache, F. Springer, D. Makarov, H. Rohrmann, T. Schrefl, J. Fassbender, and M. Albrecht, “Magnetic properties of granular cocrpt:sio$_2$ films as tailored by co$^+$ irradiation,” *J. Appl. Phys.*, vol. 107, no. 9, p. 093915, 2010.

[131] R. Micheletto, H. Fukuda, and M. Ohtsu, “A simple method for the production of a two-dimensional, ordered array of small latex particles,” *Langmuir*, vol. 11, no. 9, p. 3333, 1995.

[132] J. Fassbender, T. Strache, M. O. Liedke, D. Marko, S. Wintz, K. Lenz, A. Keller, S. Facsko, I. Moench, and J. McCord, “Introducing artificial length scales to tailor magnetic properties,” *New J. Phys.*, vol. 11, no. 12, p. 125002, 2009.

Acknowledgement

I would have never been able to write this thesis without the help of a lot of people. It has been a very inspiring but also funny and relaxed atmosphere in the group which motivated me working on this thesis very much. The obligatory breakfast in the morning was always the best start in the day one can imagine and I am really gonna miss working with all the people I had the pleasure to work with.

However, there are some people I want to thank separately:

- Prof. Manfred Albrecht for his supervision and great support over the entire time. Without our nearly daily discussions and his constant help, these past two years would not have been what they were.
- Prof. Thomas Schrefl for his scientific support and the very nice visits in St. Pölten, something I will never forget. Without him, I could not even have started my Ph.D. - literally - as I would have had no idea of what to do. Working together with him, learning how to use his software, visiting him and discussing about new recording ideas while sitting in a sea-restaurant and drinking Austrian beer was probably the nicest experience while being Ph.D. student.
- Dr. Denys Makarov for the endless discussions, his valuable tips and for sharing his sometimes unbelievable knowledge about so many things. From time to time I thought it might be boring and bugging for him to read my papers again and again, but he always did it with so much thoroughness that it really helped me improving my scientific working style. Thanks a lot for that!
- Dr. Christoph Brombacher for all the discussions and a lot of scientific input.
- Olav Hellwig, Rebekah Brandt and Holger Schmidt for making my stay in the US as pleasant as possible.
- Ute Vales for being able to ask her everything about administration, even if it was written on some website and I was just unable to find it.
- My family and my fiancee Julia for all their support and understanding over the last two years.

Curriculum vitae

Personal data

Name:	Philipp Krone
Date of birth:	13.03.1987
Place of birth:	Ratingen
Nationality:	German
Marital status:	Single

Education

from 01/09	Ph.D. Student in Physics Chemnitz University of Technology, Chemnitz Advisor: Prof. Dr. M. Albrecht *Magnetization Reversal Processes of Nanostructure Arrays*
10/6/27 - 10/7/2	Participation at the 60th Meeting of Nobel Laureates in Lindau
10/08 - 12/09	Diploma thesis in Physics Chemnitz University of Technology, Chemnitz Advisor: Prof. Dr. F. Richter *Charakterisierung und Modellierung einer gepulsten Magnetronentladung*
10/04 - 10/08	Studying Physics Chemnitz University of Technology, Chemnitz
08/96 - 06/04	Secondary School Johannes Kepler Gymnasium Chemnitz, Germany
08/93 - 07/96	Elementary School Grundschule Sonnenberg, Germany

List of publications

2011

- P. Krone, D. Makarov, A. Cattoni, G. Faini, A.-M. Haghiri-Gosnet, I. Knittel, U. Hartmann, T. Schrefl, and M. Albrecht
  Investigation on the magnetization reversal of a magnetic dot array of Co/Pt multilayers
  Journal of Nanoparticle Research, DOI: 10.1007/s11051-010-0123-z.

- P. Krone, M. Albrecht, and T. Schrefl:
  Micromagnetic simulation of ferromagnetic resonance of perpendicular granular media: Influence of the intergranular exchange on the Landau-Lifshitz-Gilbert damping constant
  J. Magn. Magn. Mater. **323**, (2011) 432-434.

2010

- P. Krone, D. Makarov, M. Albrecht, and T. Schrefl:
  Magnetization reversal of bit patterned media: Role of the angular orientation of the magnetic anisotropy axes
  J. Appl. Phys. **108**, (2010) 013906.

- P. Krone, D. Makarov, T. Schrefl, and M. Albrecht:
  Exchange coupled composite bit patterned media
  Appl. Phys. Lett. **97**, (2010) 082501.

- P. Krone, C. Brombacher, D. Makarov, K. Lenz, D. Ball, F. Springer, H. Rohrmann, J. Fassbender, and M. Albrecht:
  Nanocap arrays of granular CoCrPt:SiO2 films on silica particles: tailoring of the magnetic properties by Co+ irradiation
  Nanotechnology **21**, (2010) 385703.

- P. Krone, D. Makarov, M. Albrecht, T. Schrefl, and D. Suess:
  Magnetization reversal processes of single nanomagnets and their energy barrier
  J. Magn. Magn. Mater. **322**, (2010) 3771-3776.

- C. Schulze, M. Faustini, J. Lee, H. Schletter, M. U. Lutz, P. Krone, M. Gass, K. Sader, A. L. Bleloch, M. Hietschold, M. Fuger, D. Suess, J. Fidler, U. Wolff, V. Neu, D. Grosso, D. Makarov, and M. Albrecht:
  Magnetic films on nanoperforated templates: A route towards percolated perpendicular media
  Nanotechnology **21**, (2010) 495701.

2009

- Y. Demidemko, D. Makarov, P. Krone, and V. Lozovski:
  Effect of a magnetic field on the optical properties of nonmagnetic nanorods in a dielectric matrix
  J. Optics A: Pure and Applied Optics **11**, (2009) 125001.

- D. Makarov, P. Krone, D. Lantiat, C. Schulze, A. Liebig, C. Brombacher, M. Hietschold, S. Hermann, C. Laberty, D. Grosso, and M. Albrecht:
  Magnetization Reversal in Arrays of Magnetic Nanoperforations
  IEEE Trans. Magn. **45**, (2009) 3515.

- P. Krone, D. Makarov, T. Schrefl, and M. Albrecht:
  Effect of the anisotropy distribution on the coercive field and switching field distribution of bit patterned media
  J. Appl. Phys. **106**, (2009) 103913.

Selbstständigkeitserklärung

Ich erkläre hiermit, dass ich die vorliegende Arbeit selbstständig und nur unter Verwendung der angegebenen Quellen und Hilfsmittel angefertigt habe. Es ist nicht bereits früher oder gleichzeitig an anderen Hochschulen oder an dieser Universität ein Promotionsverfahren beantragt worden.

Philipp Krone

Chemnitz, den 29.03.2011